Ozone Removal at Microsecond Contact Time using Microfibrous Entrapped Catalysts

by

Qiang Gu

A dissertation submitted to the Graduate Faculty of
Auburn University
in partial fulfillment of the
requirements for the Degree of
Doctor of Philosophy

Auburn, Alabama
May 10, 2015

Keywords: Microfibrous Entrapped Catalyst, Pressure Drop Modeling, Ozone Decomposition Catalysts, High Volumetric Flow, Convective Heat Transfer

Approved by

Bruce J. Tatarchuk, Chair, Professor of Chemical Engineering
W. Robert Ashurst, Associate Professor of Chemical Engineering
Yoon Y. Lee, Professor of Chemical Engineering
Ruel A. Overfelt, Professor of Materials Engineering

Abstract

Microfibrous Entrapped Catalysts (MFEC) manufactured from 8μm diameter nickel fibers were engineered into pleated heterogeneous catalytic reactors to improve catalytic performance from conventional packed bed and monolith reactors at high volumetric flows, since microfibrous materials can entrap small particles (150-200μm) which significantly improves inter-phase mass transfer. Conventional reactors usually operate with contact time less than 1s. MFEC reactors were able to reduce the contact time to micro seconds while maintaining similar catalytic performance. This gives MFEC a huge advantage in terms of weight and volume saving, since the conventional meter-long reactors were shortened to millimeter-thick material sheets. These unique reactors were targeted at ozone, which was widely recognized as the No.1 aircraft cabin air pollutant.

In this research, MFEC reactors were investigated under turbine bleed air conditions of high temperature (100-200 ºC) and high face velocity (10-40 m/s) resulting in an interlayer contact time of 67-200μsec. Precious metal (Pd, Ag) and transition metal (Mn) catalysts were impregnated on entrapped particles (e.g. γ-Al_2O_3) using incipient wetness method. Ozone test concentration was set at a high-demanding 1.5 ppmv. Results showed that a high level of ozone decomposition was achieved with a significant reduction of catalyst consumption. Compared with conventional aircraft filters, this reduction can be a huge advantage in terms of material cost and labor. Reaction kinetics analyses were compared for different catalysts. Results showed that

precious metal catalyst performs better at a higher temperature while transition metal catalyst maintains similar conversion when changing temperature. Tests such as XPS, TPR and TGA have been used to evaluate performance of catalysts and modify catalysts to improve conversion rate. Also catalyst aging tests were conducted according to the frequency of commercial aircraft ozone reactor replacement, which evaluated long-term performance for actual MFEC reactor usage. In various applications, high volumetric flow application of MFEC encounters a high pressure environment; catalytic performances of MFEC at these conditions are expected to be different from their low pressure counterpart, since key physical characteristics, including density, effective diffusivity and reaction rate changed at these conditions. A small scale experiment setup is constructed to further evaluate the performance of MFEC at higher pressures. Various heat and mass transfer parameters have been compared by a model constructed by Kalluri *et al*.

In addition, a comprehensive CFD pressure drop has been established based on the physical characteristics of the fiber material and entrapped particles acquired by SEM imaging. A numerical solution of the Navier-Stokes equation within the fiber material has been done to prove that pressure drop of the whole material sheet can be modeled using a small disassembled part of the whole area. A large number of random areas have been sketched and tested for position dependence of the pressure drop. Simulation results showed good estimation of the total pressure drop of flat MFEC sheets. The accuracy of model has been improved by considering the compression effect caused by the large pressure drop across the material sheet. Pleated structure pressure drop has also been conducted using the micro scale data, which showed very accurate estimation of pressure drop across MFEC.

Heat transfer phenomenon of MFEC at high volumetric flows has also been studied in this research. Ensemble average method is used to evaluate radial and axial heat transfer coefficient at forced convection conditions. Temperature distribution within the MFEC is acquired by numerical solution of heat transfer equation at high volumetric conditions with different boundary conditions. Temperature distribution is also acquired experimentally by using an Omega® multi-point thermocouple. Two temperature profiles are compared for model accuracy. Nusselt number has been used to evaluate the degree of convection at different velocities. Moreover, heat transfer at higher pressure condition is also conducted as an evaluation of applying MFEC at high volumetric flow and high pressure environment.

Acknowledgments

I would like to acknowledge the encouragement and guidance from my research advisor Dr. Bruce J Tatarchuk. I would also like to show my sincere appreciation to all my committee members: Dr. Robert Ashurst, Dr. Yoon Lee and Dr. Ruel Overfelt. I also want to acknowledge Dr. Bart Prorok for his time serving as my university reader. This dissertation would not have been possible without the unwavering support and suggestions of research advisor in CM3 group Dr. Donald R. Cahela and mechanical support of Troy Barron from Intramicron Inc. Also without the cooperation and support of my colleagues from center for microfibrous material manufacturing, especially Kimberly Dennis, Dwight Cahela, Megan Schumacher, Benjamin Doty, Min Sheng, Amogh Karwa, Abhijeet Phalle, Robert Henderson, Hongyun Yang, Yanli Chen, Ying Zhu, Carlos F. Gonzalez, William R. Yantz Jr., Priyanka P. Dhage, Wenhua Zhu and many others, this work would not have been possible. I would like to thank Ms. Yvonne Williams for her careful proof reading of this written work. I am also very grateful to the help from department staff Sue Abner and Karen Cochran through my tenure at Auburn.

Most importantly, I would like to thank my family, especially my parents and wife Jingshan Wang for their unconditional love, support and trust in me. My sincere thanks goes to my friends especially Jiawei Zhang, Wei Yuan, Jingyuan Xiong, Zhiyang Ding, Xiaojun Ruan, Rui Xu, Sihe Zhang, Ying Zhu, Yixian Yang, Jiong Xie, Shu Yin, Fan Yang, Suihan Wu, Teng Xu, Aaron Seeto, Jingran Duan, Min Sheng, Huirong Li, Yiqun Wang Pengfei Zhao, Peng

Cheng, Xueni Sun, Xinquan Cheng Zequn Liu and many others who made my stay at Auburn an unforgettable memory.

Table of Contents

List of Tables

List of Figures

List of Abbreviations

CFD	Computational Fluid Dynamics
CM3	Center for Microfibrous Material Manufacturing
MFEC	Microfibrous Entrapped Catalysts
PLC	Programmable Logic Controller
PV	Pressure Volume
SEM	Scanning Electron Microscope
TEM	Transmission Electron Microscopy
VOC	Volatile Organic Compounds

Nomenclature

A	crossing area, m^2
C_p	heat capacity, J/kg-K
D	diameter, m
E_a	apparent activation energy, J/mol
h	inside heat transfer coefficient, W/m^2-K
ΔH	reation heat, J/mol
k	thermal conductivity, W/m-K
L	length, m
Pr	Prandtl number
r	radial position, m
Re	Reynolds number
R	gas constant, 8.314 J/mol-K
t	time, s
T	temperature, K
U	overall heat transfer coefficient, W/m^2-K
v	superficial velocity, m/s
V	volume, m^3
x	mass fraction
z	axial position, m

Greek symbols

ϵ	voidage
μ	gas viscosity, kg/m-s
ρ	density, kg/m^3
φ	shape factor

Superscripts

n	n^{th} step

Subscripts

Al	alumina
e	effective
f	fluid
F	fiber
i	i^{th} particle or i^{th} division
id	inside diameter
j	j^{th} division
m	metal
od	outside diameter
p	particle
r	radial
w	wall

z	axia

Chapter I. Introduction to ozone removal and high volumetric testing & Literature Review

I.1. Introduction

The field of air filtration is composed of two major parts, mechanical filtration and molecular filtration. Over the past decades, the demand for improved indoor air quality has increased. In early days, mechanical filtration received more attention, since airborne particles have caused many respiratory problems in the working environment. Particulate filters have been utilized for most mechanical filtrations. Air-filtration and cleaning systems can remove a variety of contaminants from airborne environment. Their effectiveness will depend on the nature of those contaminants. Today, as more chemicals are introduced into everyday life, removing only airborne particles cannot satisfy the demand for clean air, since certain molecular contaminants, including O_3, CO and VOC etc. can also bring respiratory problems such as lung cancer, allergy, and dryness of skin. These problems are especially significant in a compact system like a commercial jet aircraft where cleaning agents are frequently used and outside contaminants are brought in by the AC system (O_3 abundant at high altitude). However, since these compact systems usually serve more concentrated populations, the amount of clean air demand is large, while ducting and air handling systems on board must be small. To meet these demands and compensate for the limitation of the compact system, molecular filtration

has to be tested at higher face velocity and high temperatures to supply enough air and increase catalyst activity for contaminant removal.

In this research, microfibrous entrapped catalyst reactors are tested for molecular filtration at high face velocity and high temperature for advantages over conventional packed bed and monolith reactors. The operating conditions required on a compact system should be low pressure drop and high contaminant conversion rate. By introducing microfibrous entrapped catalyst reactor, it is expected that high pressure drop of packed bed reactor can be avoided and more turbulence enhancement can be brought in to improve mass transfer rate compared with monolith reactors.

In the first part of this dissertation, the pressure drop over pleated microfibrous entrapped catalyst reactors is tested and compared with packed bed and monolith reactors. The pressure drop of microfibrous entrapped catalyst reactor is modeled with the aid of SEM imaging. In the second part, catalyst performance of the microfibrous media is tested. The reaction kinetics are analyzed. Catalysts used for ozone decomposition are characterized using SEM, TEM, TGA and other techniques. The effects of humidity, catalyst loading, and particle sizes are also examined. The third part evaluates the performance of MFEC in high pressure environment, since this condition is frequently encountered in high volumetric flow applications. The final part investigates the heat transfer characteristics of MFEC at high volumetric flow condition and in both low and

high pressure environment. The conclusion and suggested future work are summarized in the final part.

I.2. History of ozone removal

Photochemical conversion of oxygen creates ozone in the atmosphere. Ozone, a potent greenhouse gas, is usually found in the earth's upper atmosphere (10~30 miles above the earth's surface). The concentration usually increases with latitude and changes with seasons and weather. Research has also found that emission of NO_x from aircraft has increased the photochemical conversion of ozone. Penner *et al.* have reported modeling result of 2-5 ppb of increase in middle troposphere at northern mid-latitude, where most aircraft fly. The ozone increase level is linear with amount of NO_x generated.

In the late 1970s, airline customers and flight personnel began to report symptoms including irritations in nose, eyes, and throat with headaches. At the same period, the commercial aircraft began to fly at higher altitudes. At these altitudes, ozone level has become more and more significant compared with levels on the ground. To evaluate this issue, the Global Atmosphere Sampling Program conducted ozone concentration measurements in and out of the cabin of a B-747-100 in 1977 (Figure I-1). Figure I-1 shows that the outside ozone concentration can be well over the limit set by FAA in 1985. According to FAA, cabin air ozone level should not be over 0.25 ppm at

any time over 32,000 ft flight. The level of 0.10 ppm should not be passed for any 3-hour flight over 27,000 ft. If the aircraft cabin air has been left untreated, it will cause a series of health problems, including coughing, throat irritation and uncomfortable chest feelings. Since the regulations have been set, research and publications on aircraft cabin air have transferred much attention to ozone level monitoring and ozone filters.

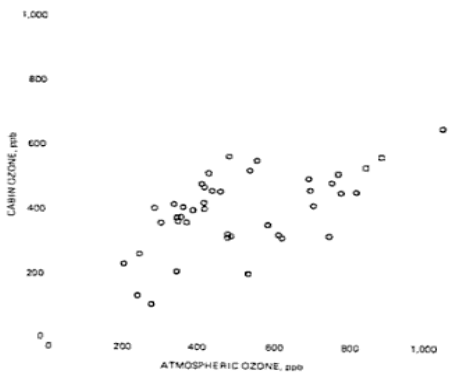

Figure I-1. GASP measurement of ozone level in and out of aircraft cabin

Airlines have solicited from companies solutions for the onboard ozone level problem for quite a few years. Different approaches including thermal, adsorption and catalytic have been attempted. It was found that the amount of adsorbent required is overwhelming because of the large demand for clean air. The thermal decomposition method requires a higher temperature and higher pressure environment. This requirement will consume extra energy besides the power for aircraft, which will reduce the overall efficiency. Compared with thermal decomposition and adsorption, catalytic decomposition will operate at much lower temperature without a large consumption of

adsorbent. Figure I-2 compares the efficiency of catalytic and thermal decomposition of 1.0 ppmv ozone at 1 atm and low temperatures. Nowadays, almost all aircraft equipped with ozone filters use catalytic decomposition for ozone.

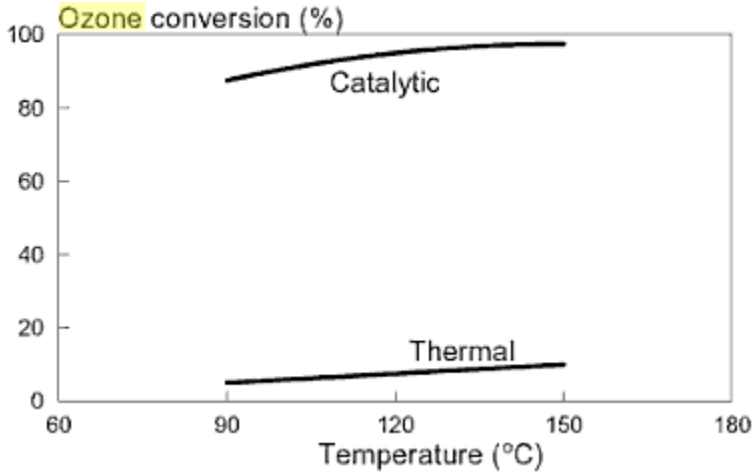

Figure I-2. Ozone conversion comparison between catalytic and thermal methods; pressure @ 1 atm, ozone @ 1.0 ppmv

Noble metal and base metal catalyst performance have been studied previously by Carr and Chen 1982, 1983; Kent and Fein 1979; and Chang 1980 for ozone decomposition at aircraft situations. Figure I-3 shows three metal-based catalyst performances. Compared with noble metal catalyst, base metal catalyst is much lower in cost. With some modification, these catalysts show good conversion rate at high temperatures. However, further investigation of these metal catalysts shows that most base metal catalyst is much weaker in catalyst deactivation. If 20,000 flight hours is set as

design life time for an ozone filter, palladium-based catalyst, though expensive, is much more economical if considering the labor required to change these filters.

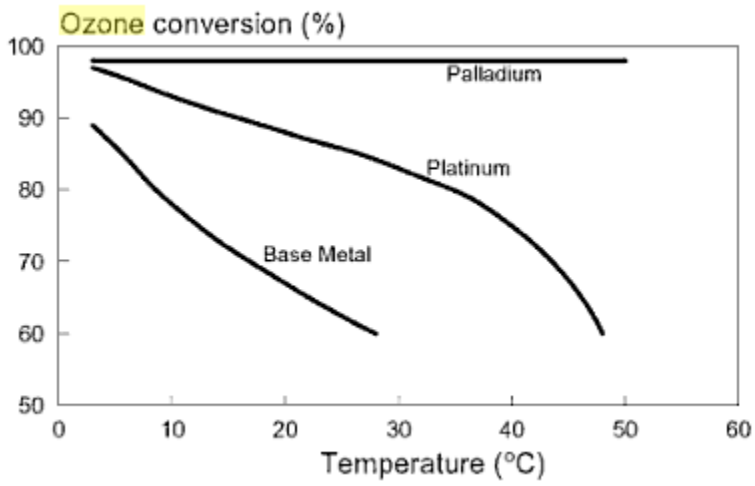

Figure I-3. Ozone catalyst performance comparison; pressure @ 1 atm, concentration at 1.5 ppmv, temperature @ 422K

For now, the major suppliers of aircraft ozone filters are BASF and Honeywell. They have designed different sizes and layouts out aircraft ozone filters, which primarily use monolith structures. Figure I-4 shows the installation of an ozone abater. Figure I-5 shows the position of ozone filters on a Boeing 767 aircraft.

Figure I-4. Installation of ozone converter on a commercial jet aircraft

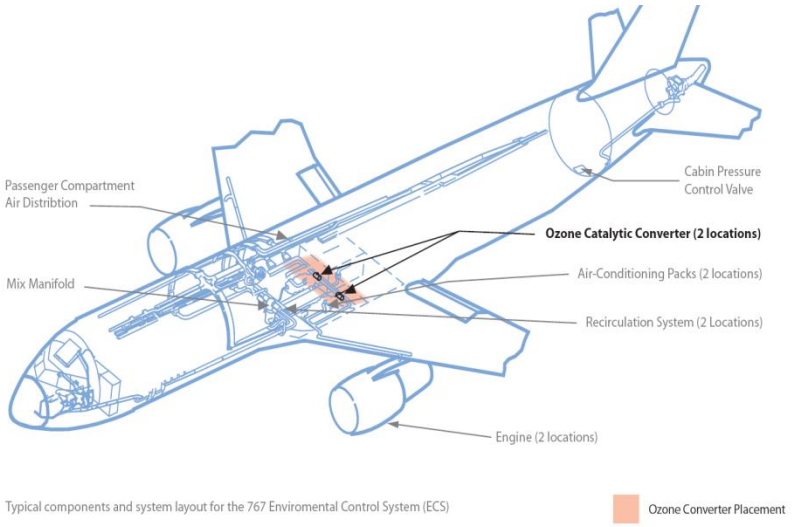

Figure I-5. Ozone converter position on a Boeing 767 jet aircraft

These converters are designed using high cell density ceramic or metal monolith reactors. However these designs have certain problems. Typical operating conditions of a wide-body jet are listed in Table I.1.

Table I.1. Operating condition for a commercial jet aircraft

Air flow condition, kg/sec	0.68-1.4
Temperature, ℃	120-200
Pressure, atm	1.6-4.0
Allowable pressure drop, atm	0.034-0.102
Vessel proof pressure, atm	5-30
Housing diameter, cm	20-28
Max weight, kg	4.5-16
Shock and vibration	Individual aircraft manufacture specification

Because of the requirement of conversion at such high face velocities, most of these reactors are designed to operate at bulk mass transfer regime, which means that enhanced turbulence and large surface area for the catalysts are preferred. Comparing the available reactor design for this application, the packed bed needs larger particle sizes to reduce pressure drop, where the available surface area is reduced due to the larger sizes. As for monolith reactors, the channel design of the reactor reduces the pressure drop, while no physical structure exists to enhance the turbulence. Both of these advantages can be solved by introducing microfibrous media into this application. With the sinter-lock network of metal fibers, smaller particles can be entrapped than with the packed bed,

leading to a large increase in the available surface. Also the sinter-lock networks of fibers act as turbulence enhancer by dividing the flow and enhancing mass transfer.

Ozone is also created by common equipment including copiers, pool cleaners, and water purification processes. Catalytic ozone decomposition has been widely applied to these situations to protect human health. Today, most ozone releasing equipment has installed ozone filters. But some have been adapted in non-optimized way. For instance, packed bed converters have been popular in most situations. But in situations like aircraft filtration, pressure drop has been a great issue as to packed bed converters. Microfibrous materials filters have been developed as a high contact-efficiency and low pressure drop alternative to these situations.

I.3. Literature review on ozone decomposition catalyst

I.3.1. Catalysts used and activity

Ozone decomposition reaction is thermodynamically favored with a heat of reaction of $\Delta H_{298}^{0} = -138\, kJmol^{-1}$ and free energy of reaction of $\Delta G_{298}^{0} = -163\, kJmol^{-1}$. However, ozone is reported by Cotton *et al.* to be stable up to 523K and catalysts are required to decompose it. Over the years, various kinds of ozone decomposition catalysts were developed; however, most of them share similar

components. These include noble metal and transition catalysts. Common noble catalysts applied are Pt, Pd, Rh and common transition catalysts are Ni, Co, Cu, Mn, Fe. These catalysts are usually applied with catalyst support materials like Al_2O_3, SiO_2, TiO_2 and activated carbon to maximize the surface area so that mass transfer limitation of the reaction can be minimized.

Since the catalysts are mostly present in metal or oxide forms, the catalysts are commonly prepared using incipient wetness method. This method is accomplished by first impregnating soluble catalysts onto the support and then drying and finally calcinations. If the catalyst is a combination of metal and oxide, the process can be done either by impregnation and calcinations at the same time or repeating a separate process. However, ozone decomposition results prefer the second method. A possible reason for this may be differing calcination temperatures, which are impossible to satisfy if mixture is needed for the reaction.

As to catalyst activity, Schwab *et al.* have reported the following sequence for the activity between metal and its oxide.

$$Cu<Cu_2O<CuO; \quad \text{(I.1)}$$

$$Ag<Ag2O<AgO; \quad \text{(I.2)}$$

$$Ni<Ni2O3; \quad \text{(I.3)}$$

$$Fe<Fe2O3; \quad \text{(I.4)}$$

$$Au<AuO3; \quad \text{(I.5)}$$

Imamura has reported the activity between different oxides for unsupported catalyst

Ag2O>NiO>Fe2O3>Co3O4>CeO2>Mn2O3>CuO>Pb2O3>Bi2O3>SnO2>MoO3>V2O5>SiO2 (I.6)

However, these catalysts are not compared controlling the surface area of these materials. The actual exposed active sites are not determined.

Dhandapani *et al.* have reported the performance of metal oxide catalyst supported on Al_2O_3 catalyst supports. These tests were carried out at 313K with face of 0.7 m/s. Inlet ozone concentration is 2ppm. Humidity at tests is 40%. They carried out the experiment until the decomposition rate reached a steady state, which removed the effect of initial conversion rate. Their results are listed in Figure I-6: MnO_2 (42%) > Co_3O_4 (39%) > NiO (35%) > Fe_2O_3 (24%) > Ag_2O (21%) > Cr_2O_3 (18%) > CeO_2 (11%) > MgO (8%) > V_2O_5 (8%) > CuO (5%).

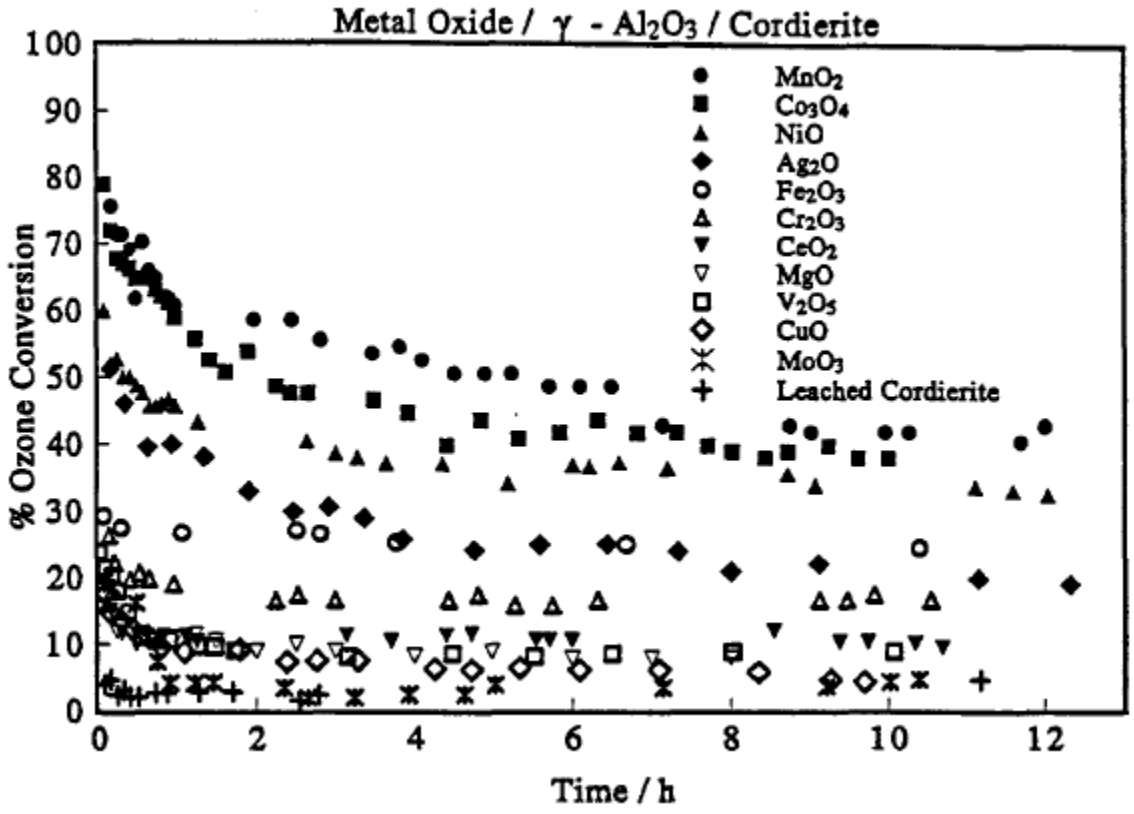

Figure I-6. Comparison of the performance of different metal oxide on Al_2O_3 foam

These results have also been compared based on normalization of the weights and moles of active component, which showed MnO_2 has the highest rate among these metal oxide catalysts. The detailed comparison is shown in Table I.2.

Table I.2 Metal oxide catalyst rate comparison

Metal oxide	Ozone conversion (%)	Rate (mol s^{-1} g of $oxide^{-1}$)	Rate (mol s^{-1} mol of $metal^{-1}$)
MnO_2	42	$1.28 \cdot 10^{-6}$	$0.11 \cdot 10^{-3}$
Co_3O_4	39	$1.03 \cdot 10^{-6}$	$0.08 \cdot 10^{-3}$
NiO	35	$1.08 \cdot 10^{-6}$	$0.08 \cdot 10^{-3}$
Fe_2O_3	24	$0.52 \cdot 10^{-6}$	$0.04 \cdot 10^{-3}$
Ag_2O	21	$0.52 \cdot 10^{-6}$	$0.06 \cdot 10^{-3}$
Cr_2O_3	18	$0.35 \cdot 10^{-6}$	$0.02 \cdot 10^{-3}$
CeO_2	11	$0.39 \cdot 10^{-6}$	$0.07 \cdot 10^{-3}$
MgO	8	$0.17 \cdot 10^{-6}$	$0.007 \cdot 10^{-3}$
V_2O_5	8	$0.20 \cdot 10^{-6}$	$0.018 \cdot 10^{-3}$
CuO	5	$0.08 \cdot 10^{-6}$	$0.006 \cdot 10^{-3}$
MoO_3	4	$0.10 \cdot 10^{-6}$	$0.013 \cdot 10^{-3}$

I.3.2. Catalyst support

To maximize the surface area of active catalyst, metal and metal oxide catalysts are usually dispersed on high surface area support. These supports are usually high surface area inorganic material containing complex pore structures.

Al_2O_3

Alumina is the most commonly used catalyst support in any application. There are various types of alumina which varies in surface area, pore size distribution, crystal structure and surface acidic properties. As the requirement of this application, the surface area of the catalyst support should be maximized. Among different kinds of alumina, γ-Al_2O_3 which typically has 100-200 m^2/g is largest in surface area. However, when

temperature goes to 1,150℃, the γ-Al_2O_3 converts to α-Al_2O_3 which 1-5 m^2/g. This temperature has determined the metal fibers to be used, since the sintering process for certain kinds of metal fibers may surpass the transition temperature. Nickel fiber sinters well under 1000 ℃ and shows good mechanical strength for pressure drop.

SiO_2

High surface area SiO_2, which has 300-400 m^2/g surface area, is also commonly used as catalyst support. In this application, both SiO_2 and Al_2O_3 should just act as inert support if bleed air is considered air only. However, the bleed air contains some level of sulfur-compound, which is reported to react with Al_2O_3. If this effect is considered, the available surface area will decrease by using Al_2O_3. Thus, SiO_2 is preferred.

TiO_2

TiO_2, which has 50-80 m^2/g surface area, is also a preferred catalyst support for aircraft bleed air ozone converters, since it is inert to sulfate formation. TiO_2 also has a transition temperature from high surface area anatase form (50-80 m^2/g) to low surface area rutile form (<10 m^2/g). This temperature is 500℃. Considering the sintering temperature of most metal fibers, this temperature is easily surpassed for any fiber.

Therefore, fluffy fiber sheets have to be considered for this support. Catalysts have to be prepared as to packed bed particles and then randomly dispersed to high-voidage fiber sheets. These sheets are compressed to required thickness.

I.3.3. Catalyst preparation

Impregnation

The active catalysts were coated on the porous catalyst supports using incipient wetness process. First, the maximum water uptake by the catalyst support is determined by slowly adding water to the catalyst support until it is saturated. In this way, water uptake by a certain amount of catalyst support is known for later use. Then, water soluble precursors are prepared based the desired weight percentage for the catalyst support. Usually, catalyst nitrites are used in this research, because either solubility of nitrite is larger or thermo decomposition of these salts to acquire active catalyst is easy. The pre-manufactured microfibrous sheets are soaked into precursor solutions for 30 minutes so those pores are filled with the solution. Extra liquid from the sheets is drained using paper towel.

Drying

Excess liquid within the fiber sheets is removed by drying at 120℃.

Calcination

The dried sheets are calcinated at 400-500℃ to thermally decompose the nitrite from metal catalysts to metal oxide form, which act as active catalyst for ozone decomposition. This process is done by blowing air through the oven while heating for 4-5 hours.

I.4. Brief on microfibrous material

Microfibrous materials are developed in the Center of Microfibrous Material Manufacturing (CM3) at Auburn University. This medium has a sinter-lock matrix structure using different material fibers ranging from four to twenty microns. The manufacturing materials include nickel, stainless steel, ceramic and polymer. The manufacturing process includes fiber dispersion, wet-lay performer, drying, sintering. As the process progresses, catalyst support particles are added during wet-lay process. These added particles enlarge the scope where microfibrous material can be applied, which

covers both mechanical and molecular filtration. Sheng *et al.* have also developed a process which can load pre-manufactured catalysts. This process has reduced the possibility of catalyst poisoning in manufacturing process and offers more versatility in catalyst selection. Meanwhile, microfibrous sheets manufactured with sintered metal fibers have shown great mechanical strength. Since normal fiber materials are mostly weak in mechanical strength, these materials can be used in more demanding situations like higher face velocity and higher pressure drop.

Microfibrous entrapped sorbents and catalyst materials have been manufactured from many types of metal fibers entrapping various sorbents and catalyst supports. Micro scale pictures of four different materials taken by SEM are shown in Figure I-7. Figure I-7A shows a material made from activated carbon fiber and two micron stainless steel fibers. The size reference on Figure I-7A, B and C is thirty microns in length. Figure I-7B shows 55-88 micron BPL carbon entrapped by a mixture of 2, 4 and 8 micron nickel fibers. Figure I-7C shows spray-dried titanium particles entrapped by two micron stainless steel fibers. Figure I-7D shows γ-alumina particles entrapped in a mesh of four and eight micron nickel fibers. Several catalyst supports have been entrapped in copper fibers as well. These materials are especially useful for applications in reducing environments at high temperatures.

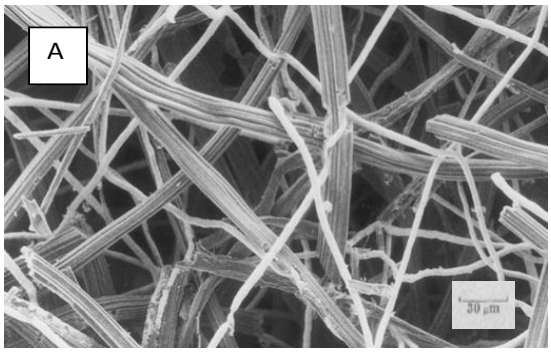

Activated Carbon Fibers and

2 μm Stainless Steel Fibers

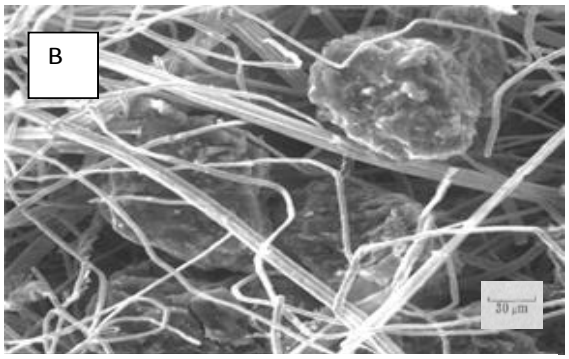

55-88 μm BPL Activated Carbon Particles
Entrapped by 2, 4 and 8 μm Nickel Fibers

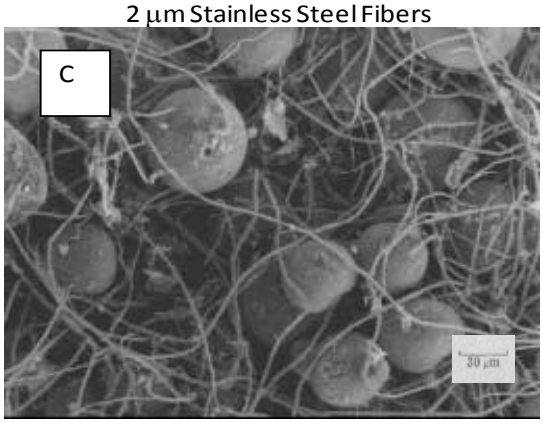

Spray Dried TiO_2 Particles

Entrapped by 2 μm 316L SS Fibers

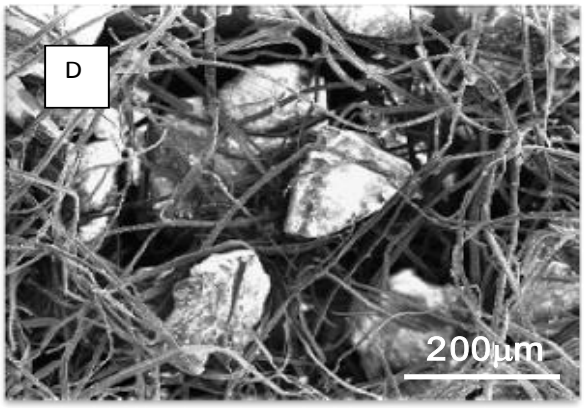

150-250 μm γ-Al_2O_3 Particles

Entrapped in 4 & 8 μm Nickel fibers

Figure I-7. Microfibrous material and with different entrapped particles;

A carbon and metal fiber mixed; B carbon fiber entrapped with nickel fiber; C TiO_2 particles entrapped by stainless steel fibers; D AlO_3 particles entrapped by nickel fibers

Microfibrous material has been carefully investigated in several aspects. Cahela *et al.* have developed the PMP equation to predict pressure drop for high voidage fiber media. Kalluri *et al.* have modeled and compared the pressure drop, mass transfer rate and overall efficiency between packed bed, monolith and microfibrous material using PMP equation and theoretical model. Yang *et al.* have studied the effect of external mass

transfers in de-sulfurization. Zhu *et al.* have contributed to the electrical conductivity of fiber media for fuel cell applications. Harris *et al.* have shown that, because of the smaller entrapped particle size, the diffusion rate into the structure has been improved. Sothen *et al.* have developed a semi-empirical pressure drop model for pleated filter and filter banks at low face velocities.

This novel kind of material provides advantages over traditional packed bed and monolith reactors in several aspects, including higher contact efficiency, higher heat and mass transfer rate. With careful reactor design, microfibrous material reactors also show reduced pressure drop which helps with energy consumption and reduced weight and volume of air handling system for the reactors. These advantages provide microfibrous materials with more versatility in application, especially in compact systems like aircraft, vessels and tanks.

Though many aspects in mass transfer and contact efficiency have been improved by using microfibrous material, this material has certain drawbacks. These mainly include lower loading capacity and higher pressure drop by single flat sheet. These problems are usually minimized by pleating the media sheets to increase media area which can improve the loading capacity and to reduce the face velocity within each pleat which can help with the total pressure drop across the filters.

Existing pressure drop models for pleated MFEC filters

Pressure drop of pleated microfibrous material has been studied by Sothen *et al.* using a semi-empirical model. This model considered several aspects of the filter geometry, including pleat number, pleat depth, pleat tip, media constant, and media support. The pressure drop for each design aspect is sketched and quantified in Figure I-8. In this model, the total pressure drop is broken down into seven terms. Six of them are geometry related, which means they are determined by the physical property of the filter. Pressure drop across the media is experimentally determined because it is much more complicated due to too many degrees of freedom including fiber dimension, fiber volume loading, fiber shape factor, fiber material, particle dimension, particle volume loading, particle shape factor, particles material, media thickness, media compressibility. By experimental determination, accuracy can be guaranteed while ignoring the details of the media.

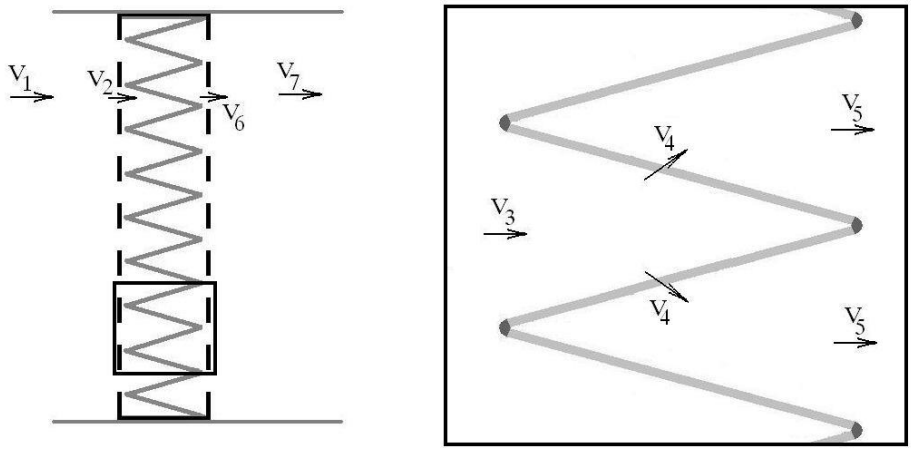

Figure I-8. Scheme of a pleated filter structure

Across Front Grating: $\Delta P_1 = \frac{1}{2}\rho[(V_2^2 - V_1^2) + K_G V_1^2]$ (I.7)

Contraction into Pleat Tips: $\Delta P_2 = \frac{1}{2}\rho[(V_3^2 - V_2^2) + K_C V_3^2]$ (I.8)

Flow in Pleat: $\Delta P_3 = \frac{1}{2}\rho[(V_4^2 - V_3^2) + K_{P1} V_3^2]$ (I.9)

Flow through Media: $\Delta P_4 = AV_4 + BV_4^2$ (I.10)

Flow in Pleat: $\Delta P_5 = \frac{1}{2}\rho[(V_5^2 - V_4^2) + K_{P2} V_5^2]$ (I.11)

Expansion from Pleat Tips: $\Delta P_6 = \frac{1}{2}\rho[(V_6^2 - V_5^2) + K_E V_5^2]$ (I.12)

Across Back Grating: $\Delta P_7 = \frac{1}{2}\rho[(V_7^2 - V_6^2) + K_G V_7^2]$ (I.13)

$$\Delta P_T = \Sigma \Delta Pi = \Delta P_1 + \Delta P_2 + \Delta P_3 + \Delta P_4 + \Delta P_5 + \Delta P_6 + \Delta P_7 \quad \text{(I.14)}$$

$$\Delta P_T = \tfrac{1}{2}\rho[(2Kg)V_3^2 + (Kc + Kp + Ke)V_4^2] + AV_5 + BV_5^2 \quad \text{(I.15)}$$

Most parameters in this model are theoretical except the media constant, which is determined experimentally. For media constant measurement, two pieces of straight pipe are used to sandwich a flat media sample for pressure drop test. Face velocities are controlled by inlet rotameters. Differential pressure drop is monitored at upstream and downstream. This test is fairly true and accurate at low speed, because the flow air does not change the property of the test media very much. However, if tests are carried out in higher face velocities, the pressure difference at two sides of the media compresses the

media momentarily, which changes the volume loading of the inside component. Sothen *et al.* have not examined the accuracy of the model. And no model containing the details of the media has been created to predict pressure drops.

I.5. Why test at high volumetric flow?

Large dimension ducts are used to supply air to households or work places, while they usually run at relatively low speeds. However, when it comes to compact systems like aircraft, ducting system volume will be much smaller, since the space for each on board equipment is limited. To solve this problem, the air filtration is proposed to run at higher face velocity by taking advantage of the power coming from the engine. Turbine bleed air has the property of high temperature and high face velocity. Treating the bleed air requires no additional equipment to push the air through the filters at high face velocity. By running at high face velocity, the contaminant filter can be running at higher efficiency and supply enough clean air to the customers and crew. This design primarily has advantages in two aspects. First, the onboard air handling system volume can be minimized, which is critical in space saving, since more equipment is required nowadays to improve customer comfort. Second, this design improves operational efficiency. By treating the turbine bleed air, less fuel is consumed by the air handling system, leading to a higher total efficiency for the whole system.

However, treating the bleed air does lead to some problems which require additional effort to solve. First, turbine bleed air is not as clean as environment air. Air from the turbine usually includes chemicals like cracked oil, sulfur compound CO and NO_x. Some of these compounds can poison the ozone decomposition catalyst and some of them have to be removed for onboard customer health. Second, the turbine bleed air is high in temperature. From previous introduction, it is noticed that cheap base metal catalysts have a short lifespan when running at high temperatures. This means noble metal catalyst, primarily Pd, is required as the catalyst component. From cost effectiveness concern, it is not as economic as running at lower speeds and lower temperatures.

I.6. High volumetric test setup

Figure I-9 shows a novel design system for testing microfibrous material at millisecond time. A variable frequency drive is used to control the system speed, which can reach over 40 meters per second in face velocity. Heaters as well as purging air are used to control temperature, which can change continuously from 100-200ºC. Contaminants including ozone and VOCs are mixed at the outlet of the blower to meet the required concentration level required for tests. System speed is acquired by

differential pressure across a bare section of the test rig. Pollutant concentration level and temperature are both monitored upstream and downstream of the reactor section.

The unique attribute of the system is the short contact time of reactant with catalyst surface. For a millimeter thickness of MFEC, system speed of over 40 meters per second shortened the contact time to less than 0.1 micro second. Due to entrapment of small particles, mass transfer rate to the catalyst is increased enough to meet the test requirement for ozone reduction.

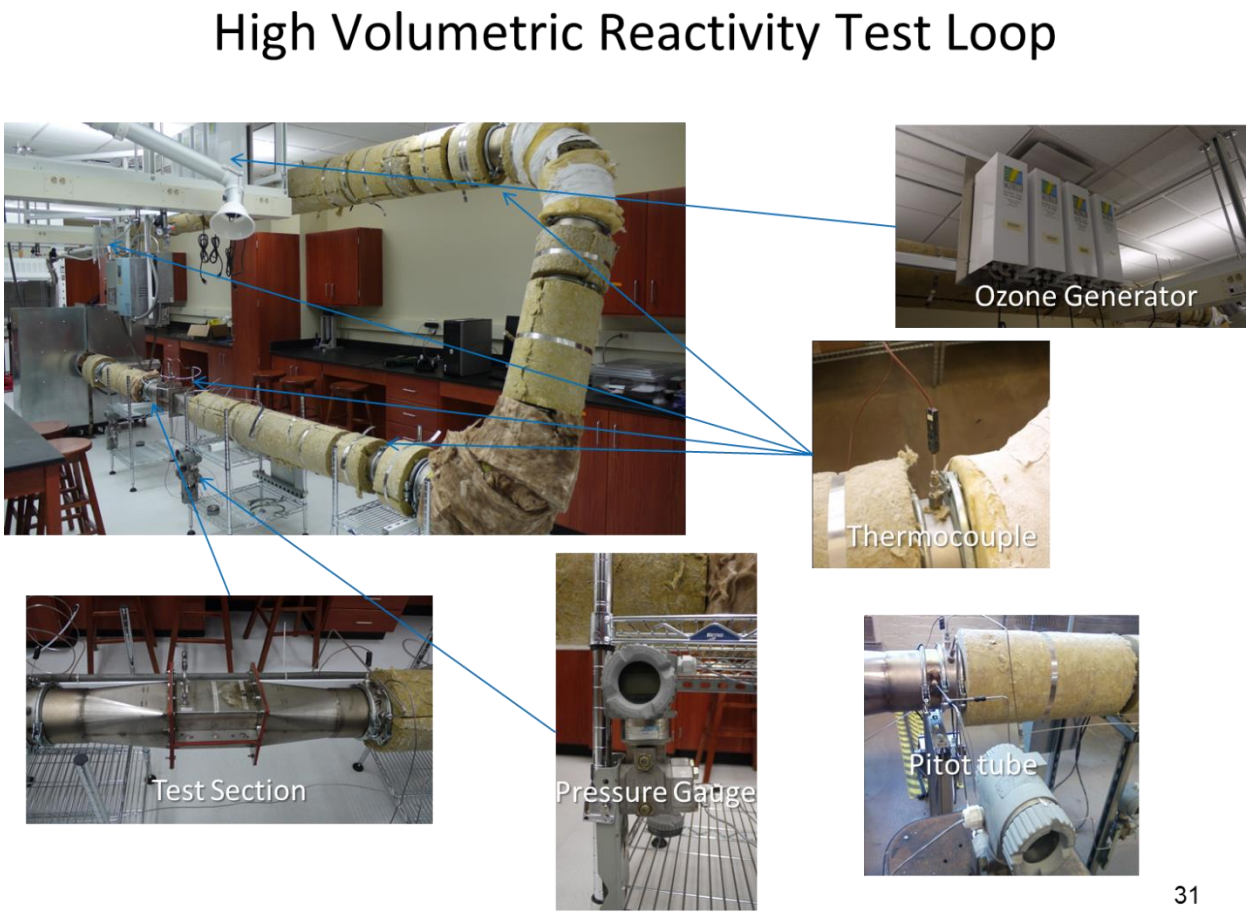

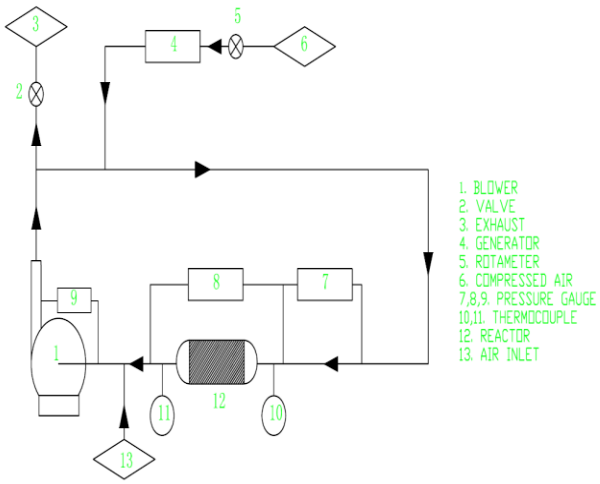

Figure I-9. High volumetric catalytic testing system of microfibrous material

I.6.1. Velocity verification

Velocity of the system is acquired by measuring the differential pressure drop across a bare section of the test rig and calculated using the following equation:

$$\Delta p = \lambda \frac{L}{D} \frac{\rho}{2} u^2 \tag{I.16}$$

Since several other factors can influence the pressure drop at the bare rig, including the velocity profile at different speeds, temperatures and pressure dependence of density and accuracy of pipe friction factor, the system speed is verified in several ways to guarantee an accurate system velocity before any data are collected. First, the system speed is verified by a commercial pitot tube (Dwyer® 167-6) located upstream of the reactor (Figure I-10). The pitot tube speed measurement is basically the same

principle as measuring the pressure drop across a bare section of the test rig (Figure I-11). The only difference is the pitot tube is less sensitive to flow pattern changes in the duct. The commercial pitot tube reading is based on temperature and air density. Temperature is obtained by an Omega® type J thermocouple located at the same position as the pitot tube. Density is calculated based on the temperature and pressure. System is reading absolute gauge pressure at the downstream of the reactor. The absolute pressure at the pitot tube is the sum of atmospheric pressure and the differential pressure across the reactor. The velocity is verified both with the pleated microfibrous media on the system and without. The velocity is also verified at temperature from 373-473K with velocities ranging from 10-40 m/s.

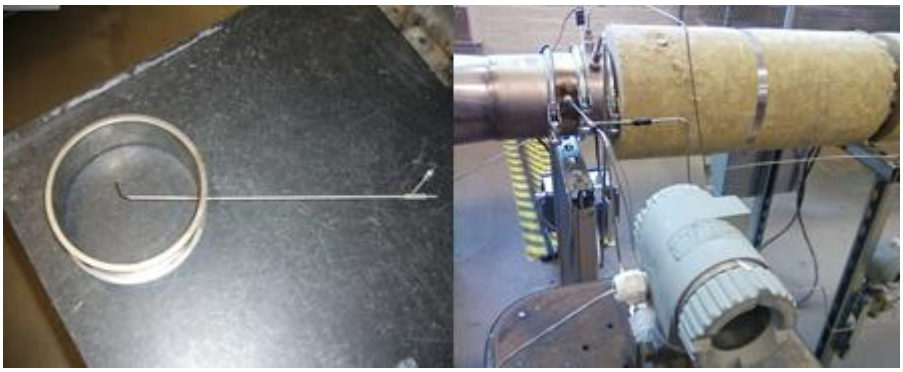

Figure I-10. Commercial pitot tube used to verify system speed

Figure I-11. Pitot tube inside structure measuring pressure difference at the two ends of the tip

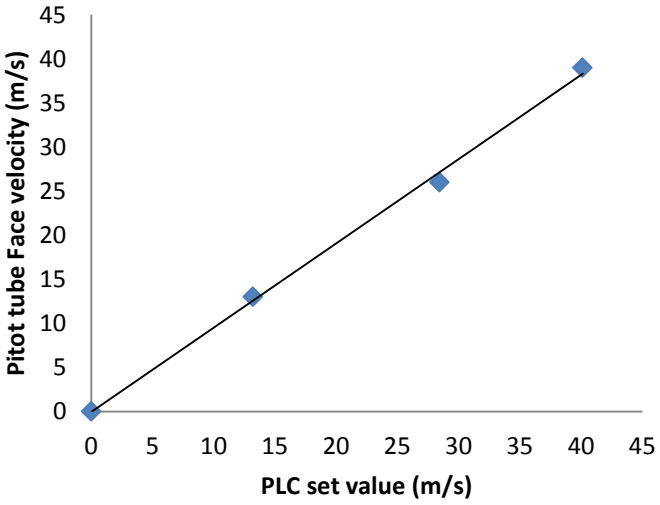

Figure I-12. Accuracy of system speed by comparing speed from bare rig pressure drop and the commercial pitot tube at 150 ºC

The comparison of the pitot tube speed and system speed has been shown in Figure I-12. The verification shows good agreement between the pitot tube speed result and bare rig speed result. However, by inserting a pitot tube in the test duct, the flow

pattern in the rig is interrupted. By analyzing the Reynolds number, turbulent flow exists in the duct. The pitot tube may increase the degree of turbulence by splitting and mixing the flow.

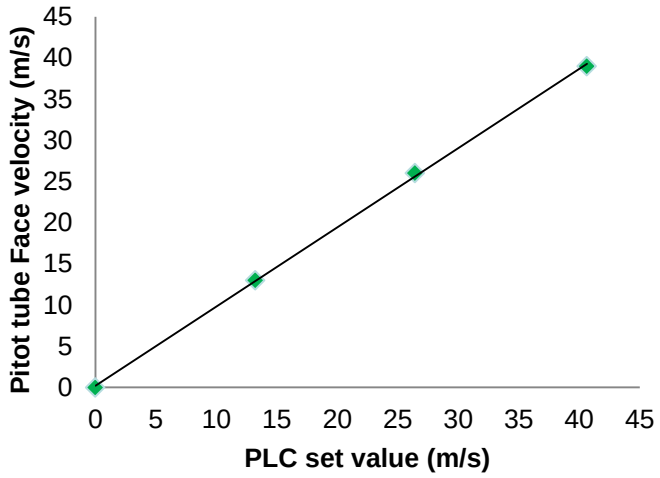

Figure I-13. Accuracy of system speed by comparing speed from bare rig pressure drop and the commercial pitot tube at 200 ºC

To eliminate the possible effect of the pitot tube, the system speed is also verified by testing the pressure drop across the blower and comparing the corresponding system speed with blower curve. In this verification, no internal interruption has been brought into the system. The system is running exactly the same conditions as testing for catalyst performance.

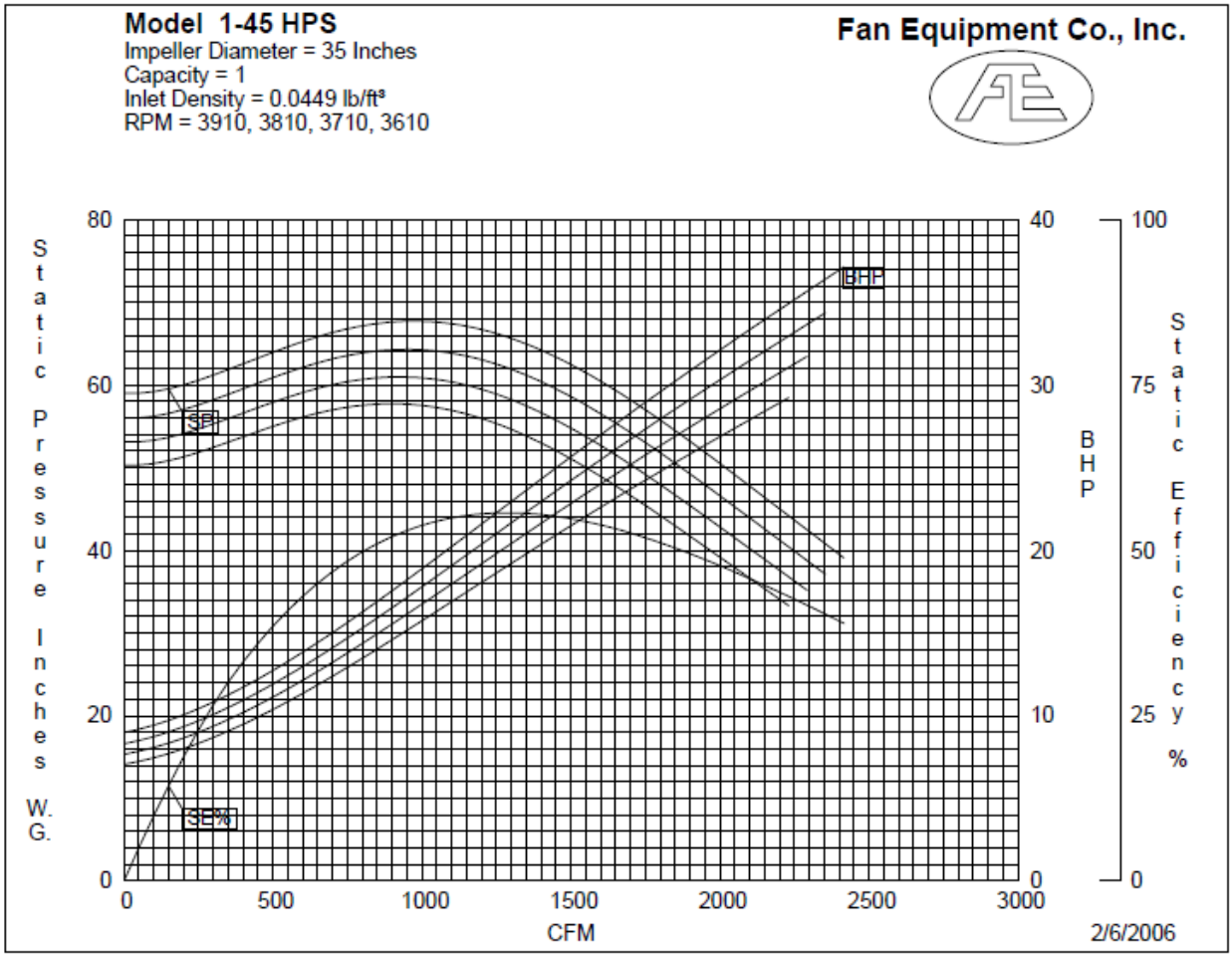

Figure I-14. Blower curve at three velocities

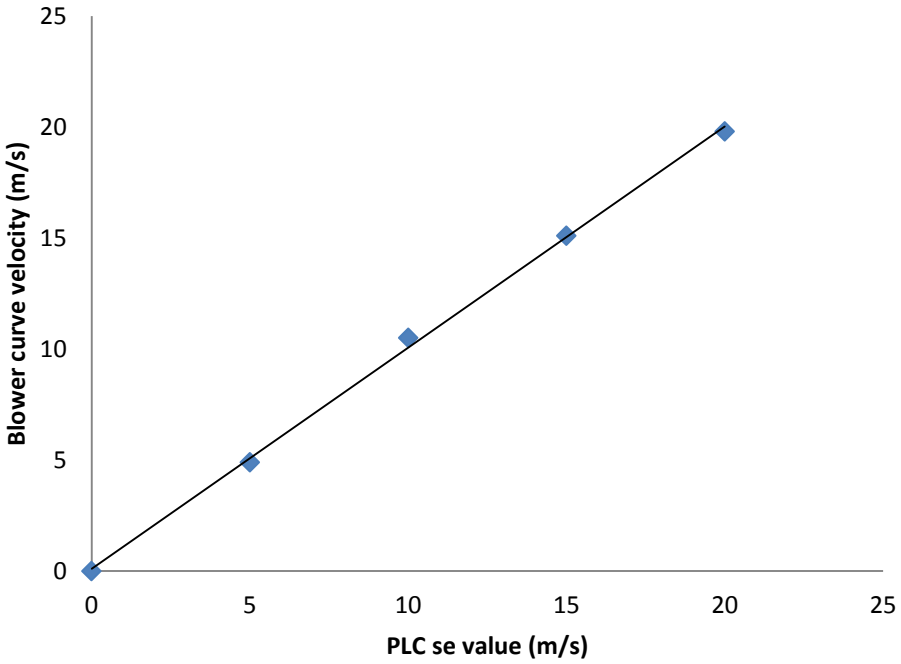

Figure I-15. Accuracy of system speed by comparing speed from bare rig pressure drop and the blower curve at 75 ºC

I.6.2. Reactor section

In this application, microfibrous material needs to be entrapped with catalyst support particles, which will bring pressure drop penalty to filter. Also, flat sheet microfibrous material has relatively small loading capacities; therefore, microfibrous media are designed to be pleated (Figure I-16), reducing the face velocity within each pleat as well as increasing available surface area to load active catalyst. Because of the high pressure difference, the structure intensity has to be considered. Normal filter

support using metal wire mesh has proved insufficiently strong at these speeds. Final structure is done by pleating single flat sheet media using u channels to increase the strength; RTV silicon is used to seal the edges and slot bottom of the structure. Figure I-17 shows the rectangular to round transition section and the rectangular test section. The purpose of the transition is simply for easy installation of applying pleat structure in the reactor.

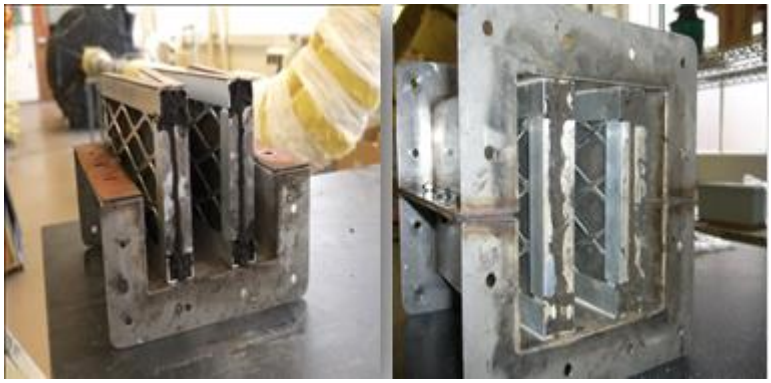

Figure I-16. Pleated microfibrous material reactor

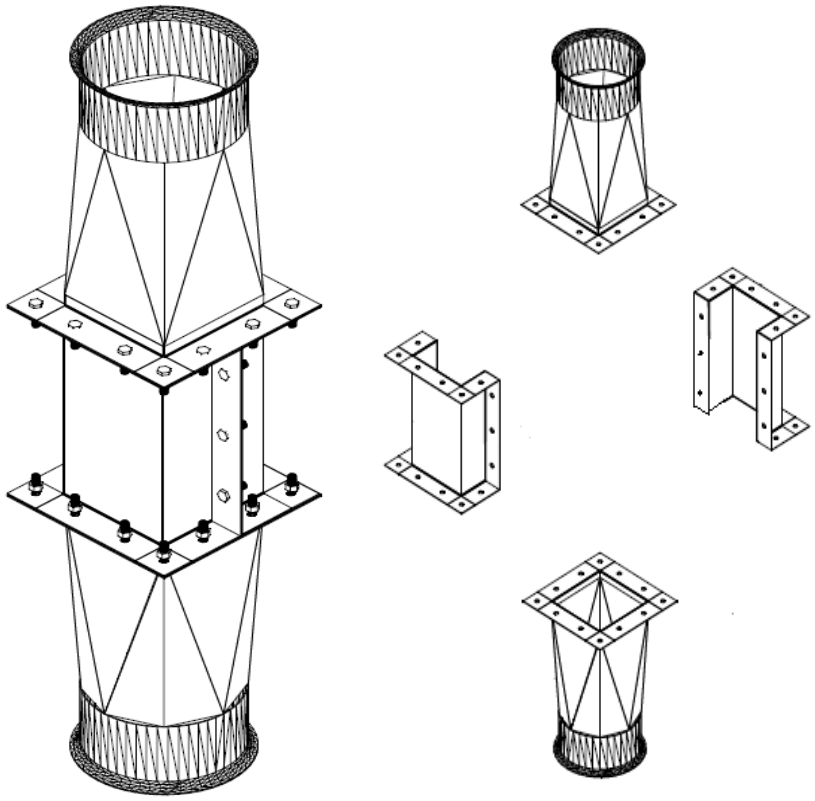

Figure I-17. Reactor section assembly

I.6.3. Heat balance of the system

Heat balance on the volumetric is complicated, since there are several sources that determine the temperature (Figure I-18). First, high face velocities of the air lead to a large amount of heat generated by the skin friction of test rig. However, velocity ranges from 10-40 m/s on the system, which means that heat generated by skin friction varies dramatically for different speeds. Second, six 1800W heaters were attached to the blower

plates. At higher speeds, the system is venting some portion of the hot air to cool the system, while at lower speeds, additional heater plates on the blower work to assist with the temperature performance. Third, microfibrous media test section for system generates a maximum of 50" H_2O pressure drop. The PV work on the micro fibrous material also generates heat for the system. This heat generation also involves the same type of skin friction as on the test rig, but in different places. Last, the test rigs are insulated with 2" thick mineral wool insulation, which helps the system to respond to temperature change quickly. The blower heaters are insulated with 6" thick mineral wool to assist heater performance.

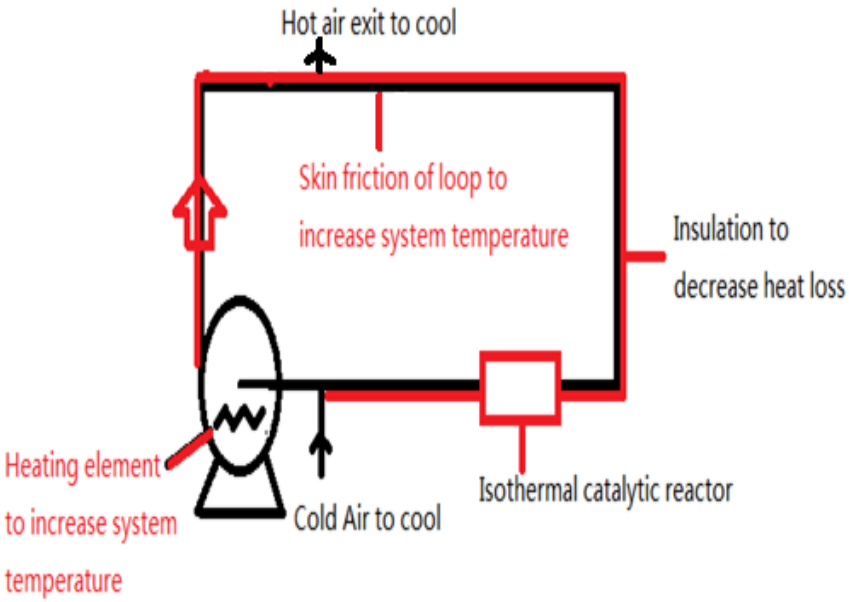

Figure I-18. Heat balance of the test rig; heat source: heater, friction; cooling source: ambient air; performance enhancer: mineral wool insulation

I.7. Summary

Ozone, as a major contaminant on commercial jet aircraft, is under closer consideration as FAA sets regulations to protect onboard customers. Efforts have been made to decompose ozone in several different ways. Catalytic conversion has proven to be the most efficient method for aircraft ozone decomposition. Monolith reactor is currently used as the converter model. However it suffers from quite a few disadvantages.

Microfibrous material is a novel structure of sinter-lock networks of fibers, which has been proved to allow lower pressure drop compared with packed bed and is expected to be better in turbulence enhancement compared with monolith reactors. By introducing microfibrous entrapped catalysts into aircraft applications, better performance in both pressure drop and catalytic decomposition is expected.

References

[1] Martha J. Boss, Dennis W. Day, Building vulnerability assessments: Industrial hygiene and engineering concepts

[2] Donald R. Cahela, Bruce J. Tatarchuk, Permeability of sintered microfibrous composites for heterogeneous catalysis and other chemical processing opportunities, Catalysis Today 69 (2001) 33-39

[3] B. Dhandapani, S.T. Oyama, Gas phase ozone decomposition catalyst, Applied Catalysis B: Enviromental 11 (1997) 120-166

[4] Daniel K. Harris, Donald R. Cahela, Bruce J. Tatarchuk, Wet layup and sintering of metal-containing microfibrous composites for chemical processing opportunities, Composites: Part A 32 (2001) 1117-1126

[5] Ronald M. Heck, Robert J. Farrauto, Suresh T. Gulati, Catalytic air pollution control: commercial technology

[6] E. H. Hunt, D. R. Space, The airplane cabin environment-issue pertaining of flight attendant comfort, International in-flight service management organization conference, Canada, November, 1994

[7] Ranjeeth R. Kalluri, Donald R. Cahela, Bruce J. Tatarchuk, Comparative heterogeneous contacting efficiency in fixed bed reactor: Opportunities for new microstructured systems, Applied Catalysis B: Environmental 90 (2009) 507-515

[8] R. R. Kalluri, R. K. Duggirala, D. R. Cahela, C. J. Roy, and B. J. Tatarchuk, CFD analysis of mass transfer enhancement due to inert structures present in fluid flow paths in heterogeneous contacting systems, manuscript submitted to computers and chemical engineering, June 2008

[9] Takashi Kameya, Kohei Urano, Catalytic Decomposition of ozone gas by a Pd impregnated MnO_2 catalyst, Journal of environmental engineering 10.1061/(ASCE)0733-9372(2002)128:3(286)

[10] Joyce E. Penner, Aviation and global atmosphere: a special report of the intergovernmental panel on climate change

[11] Ryan A. Sothen, Bruce J. Tatarchuk, A semi-empirical pressure drop model: part I-pleated filters, HVAC&R Research, Vol 14, Number 6

[12] Xinpeng Wang, Kitai Kim, Changhwan Lee and Jooyong Kim, Prediction of air filter efficiency and pressure drop in air filtration media using a stochastic simulation, Fiber and Polymers 2008, Vol. 9, No. 1, 34-38

[13] National research council, The airliner cabin environment and health of passenger and crew, National Academy Press Washington DC 2002

[14] NASA GASP (Global Atmospheric Sampling Program) Aircraft Observation, 1975 March-1979 July

Chapter II. A CFD Pressure Drop Model for Microfibrous Entrapped Catalyst Filters using Micro Scale Imaging

II.1. Abstract

Because of the dimension difference in fiber and filters, pressure drop modeling for filter structures is usually difficult if the details like fiber dimension and entrapped particle shapes are considered. This issue is solved by studying the fiber media in both micro and macro scale scope. Micro scale CFD pressure drop model for microfibrous material entrapped catalyst (MFEC) is first established using SEM imaging. The micro scale CFD model is based on theoretical calculation of velocity profile within the fiber material, which shows the plug flow pattern. SEM imaging for top and side view of the fiber media is obtained to sketch the geometric structure of the simulation area. Fiber and particle contribution to the pressure drop are studied separately. Shape factor and fiber compressibility are also considered for model accuracy. Micro scale pressure drop simulation results are then transferred into macro scale pleated filter structures for pressure drop modeling. Two kinds of filter fairing are studied for pressure drop reduction performance. All simulation results are compared with experiment data.

Keywords: Pressure Drop, CFD, SEM, MFEC

II.2. Introduction

Molecular filtration needs have been increasing dramatically recently due to the demand of high air quality in working and residential areas. The current effort to meet these demands is to adapt traditional reactors such as packed bed or monolith, even though they are originally intended for very different purposes. For such un-optimized adaptations, issues like pressure drop can lead to much higher energy consumption. Meanwhile, the weight and volume of air handling system have to be increased to compromise the pressure demand, which in many cases cannot be accepted. For example, the air handling system on an aircraft has to be compact in size, while supplying enough fresh air for onboard customers.

All these demands lead to a high voidage metal fiber material developed at Auburn University. Microfibrous entrapped catalysts (MFEC) is a sinter lock of metal fibers manufactured by conventional high speed paper making process. This material shows good structural stability, high thermal conductivity, and high contact efficiency. However, the biggest advantage of MFEC over packed bed and monolith in many applications is its reduced pressure drop. Sothen *et al.* has established a semi-empirical model to predict pressure drop over pleated MFECs. And attempts have been made by Rivers and Murphy to study pressure drop for similar materials. However, considering the huge difference between the scale of fibers and entrapped particles and the scale of

filter or reactor, no model has been constructed to study pressure drop at micro scale level.

In this research, flow pattern of high Reynolds number has been investigated using a theoretical model, which has served as the basis of micro scale pressure drop model. Later, CFD modeling using commercial software FLUENT has been conducted using SEM imaging of the microfibrous material. Also, shape factor effect of entrapped particles has been studied. In addition, compressibility of MFEC under pressure has been added to improve the accuracy to the model. Last, pleated fiber media pressure drop is modeled using micro scale simulation result. All model results have been compared with experimental data.

II.3. Flow pattern in media flow

Reynolds number is widely used as a parameter to determine flow type in certain velocities. In this application, the flow in pipes is no doubt turbulent, since the Reynolds number corresponding to 10-40 m/s is $6*10^4$-$25*10^4$. However the flow pattern within the microfibrous sheet is not easy to determine. For reactor structure that resembles packed bed reactors, Reynolds number is calculated as

$$\mathrm{Re} = \frac{\rho D u}{\mu(1-\varepsilon)} \qquad \text{(II.1)}$$

Since the particle size is used as characteristic length rather than the pipe diameter, the Reynolds number is much smaller than in the pipe. For these systems, fully turbulent flow exists for Reynolds number higher than 2000 and laminar flow exists for Reynolds number lower than 10. The Reynolds number corresponding to 10-40 m/s pipe flow in microfibrous material is 455-1818, which is in the transition state. In this situation, the flow pattern has to be determined according to specific operating conditions to determine whether it is turbulent or laminar. Hill *et al.* has studied the transition from steady to weakly turbulent flow in a close-packed ordered array of spheres. They have found that at Reynolds number of approximately 30, the transition to unsteady flow occurs, which is accomplished by breaking of rotational symmetry, resulting from the development of a vortex. At Reynolds number of approximately 50, further breaking occurs. After this region, with increasing Reynolds number, the velocity fluctuation becomes more isotropic and can be treated as turbulent flow. The result form Hill *et al.* is shown in Figure II-1. Since the Reynolds number in this application is well over the number where breaking happens, the flow within the porous media is treated as turbulent flow in all simulations.

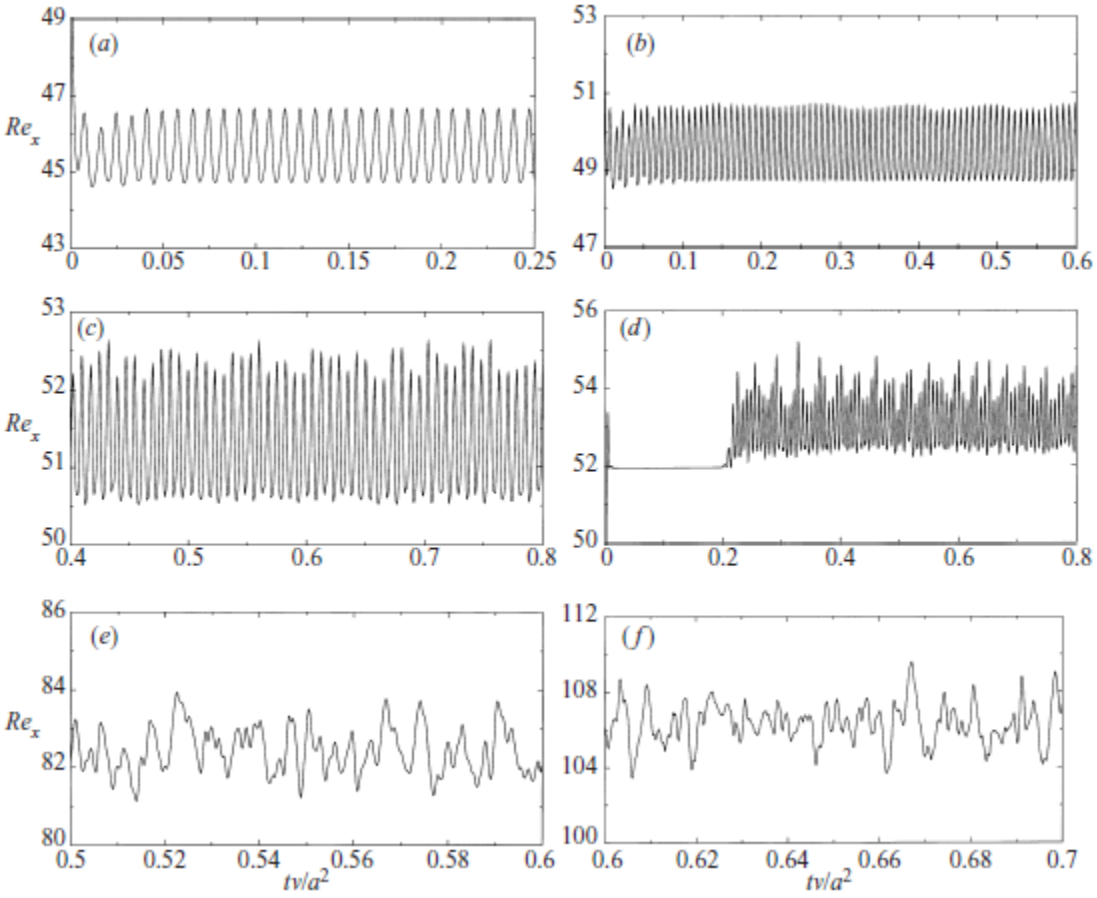

Figure II-1. Time series of stream wise component of the spatially averaged velocity

II.3.1. Velocity profile in flat microfibrous material

For high porosity media, pressure drop at low face velocity (Reynolds number <20) is described as a linear function of the face velocity, which is also known as the Darcy's law

$$\Delta p = \frac{\mu L}{K} u \qquad \text{(II.2)}$$

This equation is invalid for higher velocities. Rivers and Murphy have linked this deviation to the fiber compression by the inertial forces. Forchheimer law has been widely used in these situations to account for the nonlinear deviation, where A stands for Darcy's law constant $\mu L/K$ and B stands for the nonlinear deviation.

$$\Delta p = AV_m + BV_m^2 \tag{II.3}$$

Various approaches have been attempted by Green, Ward, Chen, Rivers and Caesar to determine a universal equation to predict constant A and B. Though all methods have generated accurate results for certain applications, no valid prediction can be made only based on fiber dimension, voidage, particle dimension and other basic properties of the fiber materials. In this research, the media constant is first determined experimentally and then verified by CFD models. Theoretical calculation of flow in microfibrous media is done by solving equation 4, which is volume average Navier-Stoke equation for porous media developed by Vafai and Tien

$$\rho\left(\frac{\partial V}{\partial t} + V \cdot \nabla V\right) = -\nabla p - AV_m - BV_m^2 + \mu\nabla^2 p + \rho g \tag{II.4}$$

Bird *et al.* has presented the Navier-Stokes equation in the following form

$$\rho\left(\frac{\partial v_z}{\partial t} + v_r\frac{\partial v_z}{\partial r} + \frac{v_\theta}{r}\frac{\partial v_z}{\partial \theta} + v_z\frac{\partial v_z}{\partial z}\right) = -\frac{\partial p}{\partial z} - AV_z - BV_z^2 + \mu\left[\frac{1}{r}\frac{\partial}{\partial r}\left(r\frac{\partial v_z}{\partial r}\right) + \frac{1}{r^2}\frac{\partial^2 v_z}{\partial \theta^2} + \frac{\partial^2 v_z}{\partial z^2}\right] + \rho g_z \tag{II.5}$$

Since v_z is independent of θ and the effect of gravity is ignored in this situation, the above equation finally reduces to

$$\rho\left(\frac{\partial v_z}{\partial t}+v_z\frac{\partial v_z}{\partial z}\right)=-\frac{\partial p}{\partial z}-AV_z-BV_z^2+\mu\left[\frac{1}{r}\frac{\partial}{\partial r}\left(r\frac{\partial v_z}{\partial r}\right)+\frac{\partial^2 v_z}{\partial z^2}\right] \quad \text{(II.6)}$$

with boundary conditions

$$v_z=0 \text{ at } r=R \text{ and } \frac{\partial v_z}{\partial r}=0 \text{ at } r=0$$

The equation expands to

$$\rho\left(\frac{\partial v_z}{\partial t}+v_z\frac{\partial v_z}{\partial z}\right)=-\frac{\partial p}{\partial z}-AV_z-BV_z^2+\frac{\mu}{r}\frac{\partial v_z}{\partial r}+\mu\frac{\partial^2 v_z}{\partial r^2}+\mu\frac{\partial^2 v_z}{\partial z^2} \quad \text{(II.7)}$$

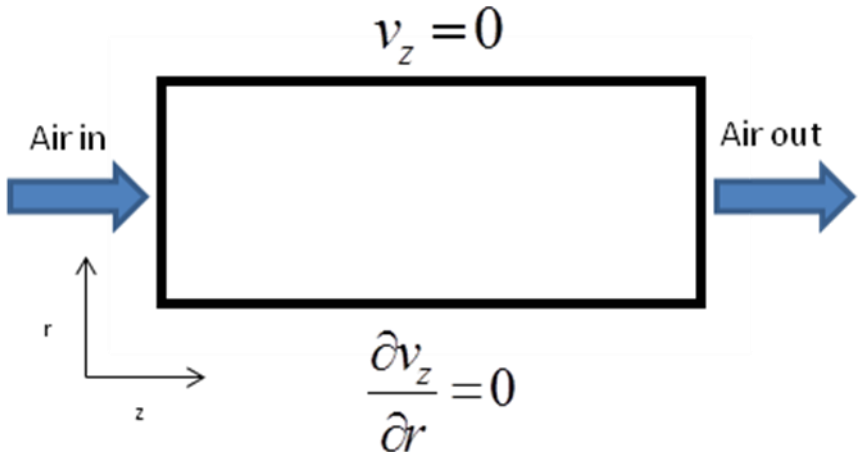

Figure II-2. Boundary condition of velocity PDE

II.3.2. Numerical process

The PDE was discretized with central difference formulation and integrated by Euler explicit method. Grid dependence was tested for the numerical solution. Final results were generated based on uniform grid spacing, using 600 divisions on radial direction and 20 in the axial direction. Domain was also meshed with 700 divisions on radial and 30 in axial for comparison. Both were calculated to steady state based on same

error estimate and the final results were identical. Von Neumann stability analysis was performed for the PDE, indicating that the scheme was conditionally stable for Courant number less than 0.5.

The discretization process is shown below. All velocity schemes are discretized using central difference for r and z directions with Euler explicit method.

$$\rho\left(\frac{v_{i,j}^{n+1}-v_{i,j}^{n}}{\Delta t}+v_{ij}^{n}\frac{v_{i,j+1}^{n}-v_{i,j-1}^{n}}{2\Delta z}\right)=\frac{\Delta p}{z}-AV_z-BV_z^2+\frac{\mu}{r}\frac{v_{i+1,j}^{n}-v_{i-1,j}^{n}}{2\Delta r}+\mu\frac{v_{i+1,j}^{n}-2v_{i,j}^{n}+v_{i-1,j}^{n}}{\Delta r^2}+\mu\frac{v_{i,j+1}^{n}-2v_{i,j}^{n}+v_{i,j-1}^{n}}{\Delta z^2} \quad \text{(II.8)}$$

Then the form for iteration is arranged as

$$v_{i,j}^{n+1}=v_{i,j}^{n}\left(1-\frac{2\Delta t\mu}{\rho\Delta r^2}-\frac{2\Delta t\mu}{\rho\Delta z^2}\right)+v_{i+1,j}^{n}\left(\frac{\Delta t\mu}{2\rho r\Delta r}+\frac{\Delta t\mu}{\rho\Delta r^2}\right)+v_{i-1,j}^{n}\left(\frac{\Delta t\mu}{\rho\Delta r^2}-\frac{\Delta t\mu}{2\rho r\Delta r}\right)+v_{i,j+1}^{n}\left(\frac{\Delta t\mu}{\rho\Delta z^2}\right)+v_{i,j-1}^{n}\left(\frac{\Delta t\mu}{\rho\Delta z^2}\right)-\frac{\Delta t}{2\Delta z}v_{i,j}^{n}v_{i,j+1}^{n}+\frac{\Delta t}{2\Delta z}v_{i,j}^{n}v_{i,j-1}^{n}+\frac{\Delta t}{\rho}\frac{\Delta p}{z}-AV_z-BV_z^2 \quad \text{(II.9)}$$

Boundary conditions are applied for the calculation at inlet, outlet, wall, and centerline of the regime.

Boundary condition at inlet

$$@\ z=0\ (j=1)\ v=10\ m/s$$

$$V\ (i,\ 1)\ =10$$

Boundary condition at outlet

$$@z=z\ (j=M+1)\ \frac{\partial v}{\partial z}=0$$

$$v_{i,M+1}^{n+1}=\frac{4}{3}v_{i,M}^{n+1}-\frac{1}{3}v_{i,M-1}^{n+1}$$

Boundary condition at centerline

$$@r=0\ (i=1)\ \frac{\partial v}{\partial r} = 0$$

$$v_{1,j}^{n+1} = \frac{4}{3} v_{2,j}^{n+1} - \frac{1}{3} v_{3,j}^{n+1}$$

Boundary condition at wall

$$@r=R\ (\ i=N)\ v=0\ m/s$$

$$V(N+1,j)=0$$

The velocity profiles in microfibrous material are shown in Figure II-3. The velocity profile resembles the plug flow pattern. The velocity difference only exists at the near wall region, which accounts for less than 3% of the whole area. This means that in most areas of the fiber sheet the average velocity is identical.

Since the dimension of the fiber and particle, the dimension of the fiber sheet and the dimension of the pleat structure are several magnitudes different, it is impossible to simulate the pressure drop of the whole structure, while considering the details of the fibers and particles. However, the details do affect the pressure drop values because certain properties like shape factor, layer thickness and media compressibility are proved to have impact on pressure drop.

With the theoretical calculation of plug flow velocity profile, we can assume that the total pressure drop of a flat sheet should resemble the pressure drop across any select area dissembled from the flat sheet. With this assumption, the CFD simulation is sketched using SEM imaging for real case pressure drop. Simulation using different

sampling from the whole area has been done to avoid location dependence for the pressure drop.

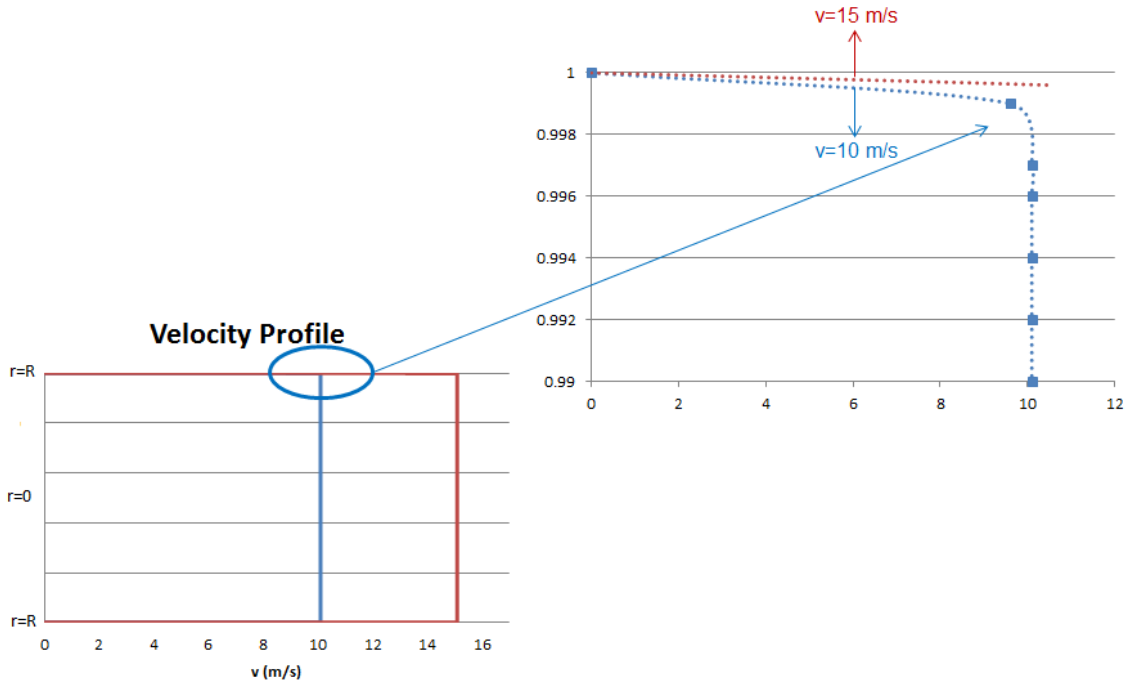

Figure II-3. Velocity Profile of microfiber material at two different face velocities with high Reynolds numbers

II.3.3. Flat sheet pressure drop measurement

The quadratic form pressure drop was measured using a 1 inch diameter steel pipe. Then 80 psi of house air was supplied as velocity inlet for microfibrous material. The test media were blank 8μm diameter nickel fiber with media thickness of 2.5mm and media entrapping 150-250 μm alumina particles with media thickness of 4mm. Both media were kept at a 4-feet distance from pipe inlet so that fluid was fully developed

before entering the media. Also, a reasonable length was maintained at downstream to avoid any unnecessary flow disorder.

Air speed was controlled by two King instrument rotameters. Due to the limitation of air pressure, the maximum face velocity was limited at 8 m/s. Pressure drops were measured using IDP10-T differential pressure transmitters which were connected 50mm upstream of the media and 125mm downstream.

Two-inch diameter samples were punched from pre-manufactured microfibrous media. Each sample was tested three times with increasing and decreasing speed for average result. Since a metal wire mesh was used as downstream support for the microfibrous material, the background resistance was measured with the same method and deducted from total pressure drop value. Figure II-4 shows the equipment sketch used to test the flat media. Quadratic pressure drop data are shown in Figure II-5.

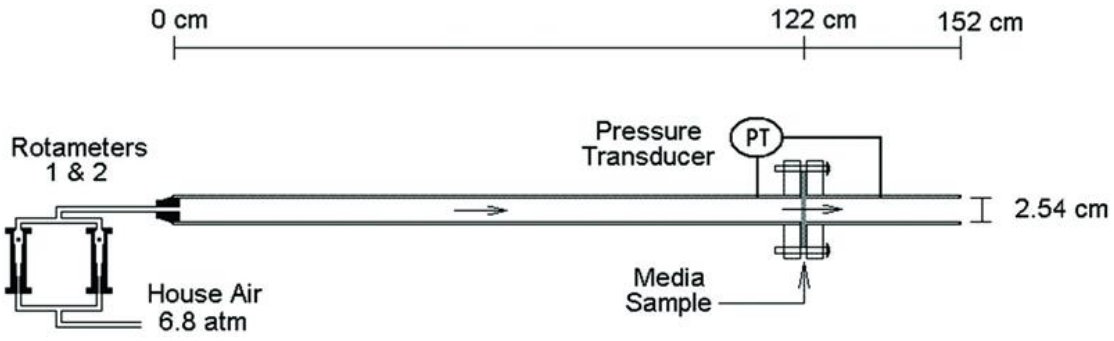

Figure II-4. Flat sheet microfibers sheet pressure drop test rig

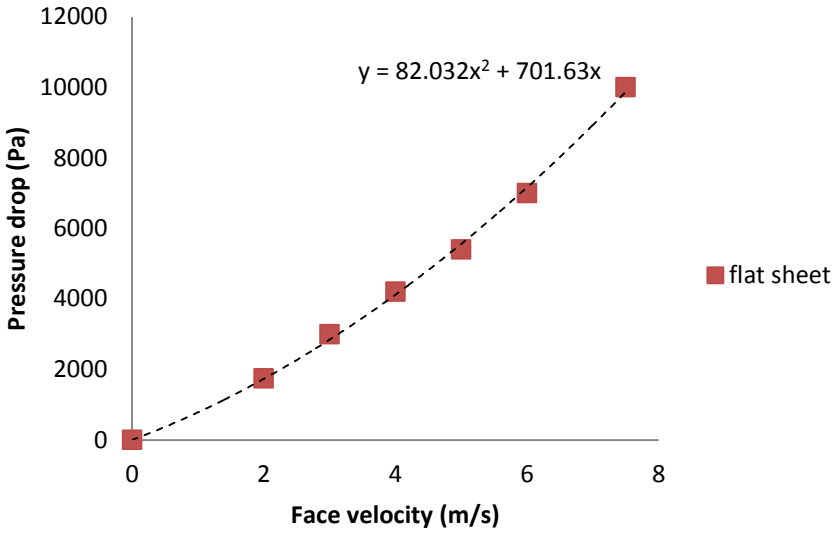

Figure II-5. Pressure drop profile for a flat sheet microfibrous material at velocities from 0-7.5 m/s

II.4. SEM imaging for model detail

When modeling fiber media pressure drop using CFD, the big challenge would be sketching the geometry of the fibers and entrapped particles. Since the ratio of actual reactor size and fiber size is exceptionally large, sketching and meshing the actual reactor with fiber detail will not be possible. However, the previous theoretical model has proved that the average face velocity for a fully developed flow is identical in most areas except near the wall. In addition, the wet-lay process guaranteed that the fibers and particles are randomly dispersed. Bearing these two aspects in mind, it is assumed that pressure drop

across any small area on the media is identical to the actual pressure drop across a flat media.

A sample SEM image of the microfibrous media and its corresponding sketch are shown in Figure II-6 and Figure II-7. Since only the top few layers are visible and easy to distinguish from one another, sketching the fiber media structure by SEM will be based on these layers. As to the inner layers, the top layers are translated because all layers are randomly dispersed and assumed to be similar in performance.

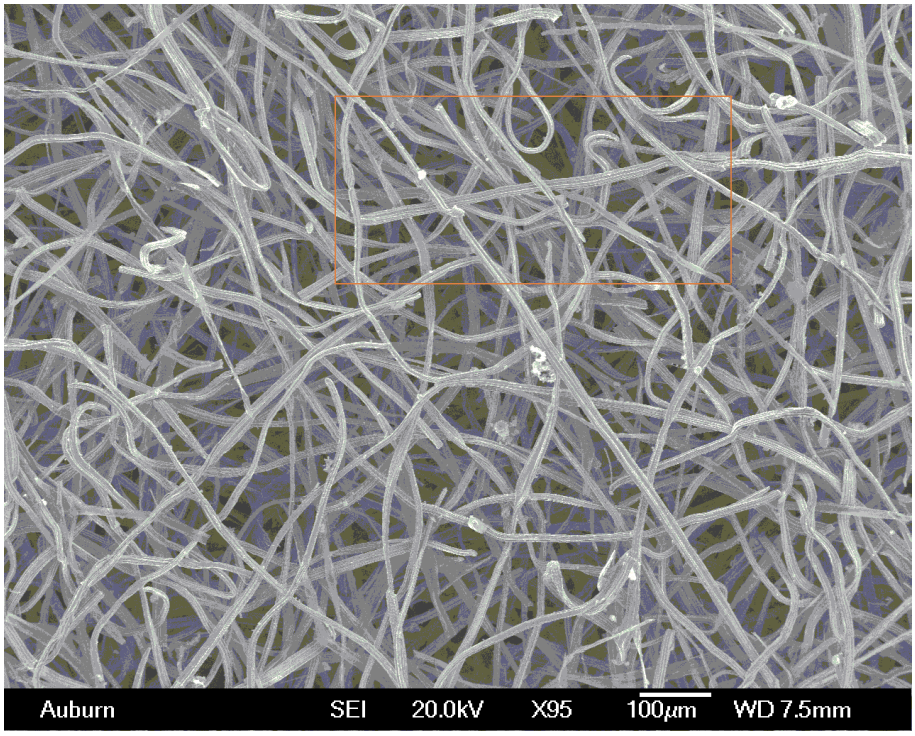

Figure II-6. Sample SEM imaging of sintered microfibrous material surface

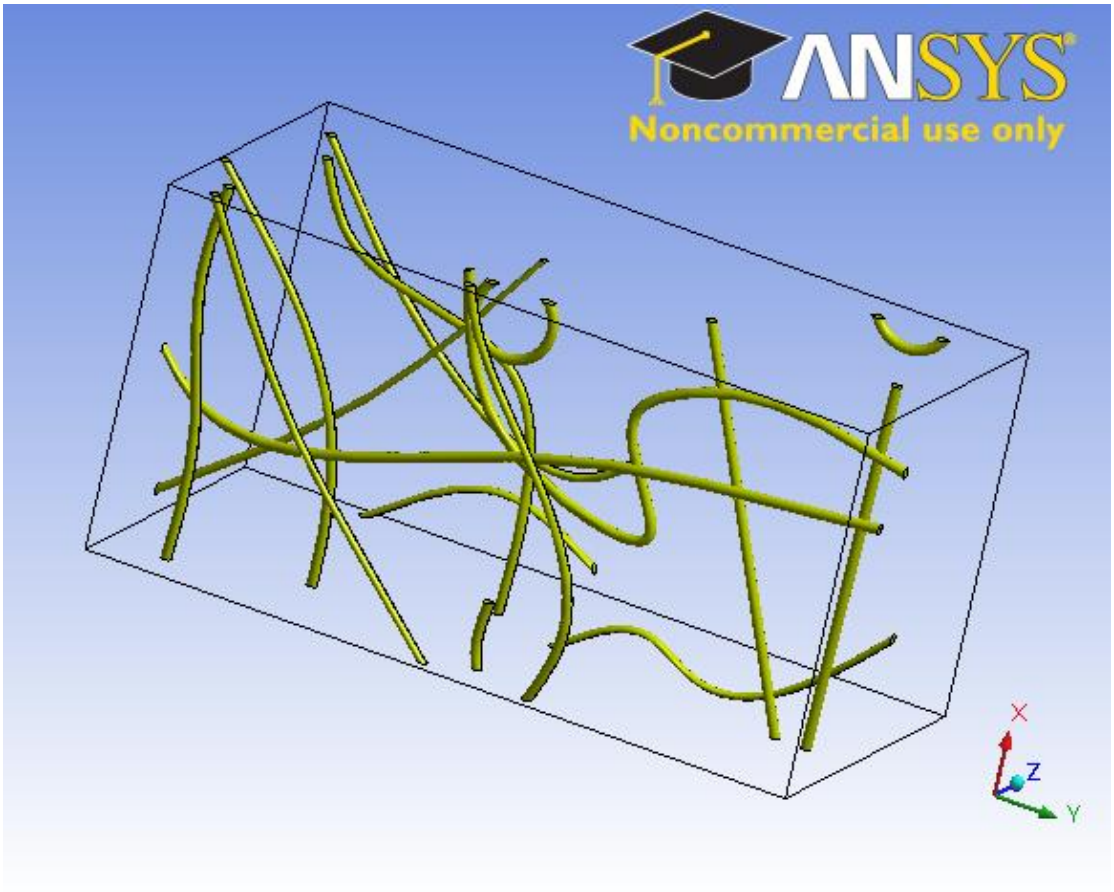

Figure II-7. Sketch of selected area of microfibrous material for simulation

Another aspect to consider when sketching the geometry is media thickness. Since fibers are randomly dispersed and vary in shape, the actual media thickness is much larger than the sum of single fiber thickness. To estimate the average space each fiber takes in thickness direction, SEM image has been taken for the side of the material. As indicated on the Figure II-8, average layers of fibers for a given thickness of media are similar. The SEM image averaged 10-11 layers for 280μm thickness of media. For actual modeling, layers are isolated 30 μm away from each other. Since a small area has been isolated from microfibrous surface to compare pressure drop, sampling from

different spots has been tested for geometry dependence. Each CFD geometry is drawn to the maximum similarity to the real SEM imaging, while the volume loading of fibers is controlled according to the original specification by which fiber sheets were made.

When comparing the difference between the cases of blank fibers and those entrapping particles, drawing is according to the cases with particles entrapped. For blank simulation, particles were disassembled from the previous drawings and adjust volume loading. In this way, the particle effect on the pressure drop can be observed without any disturbance from fiber geometry.

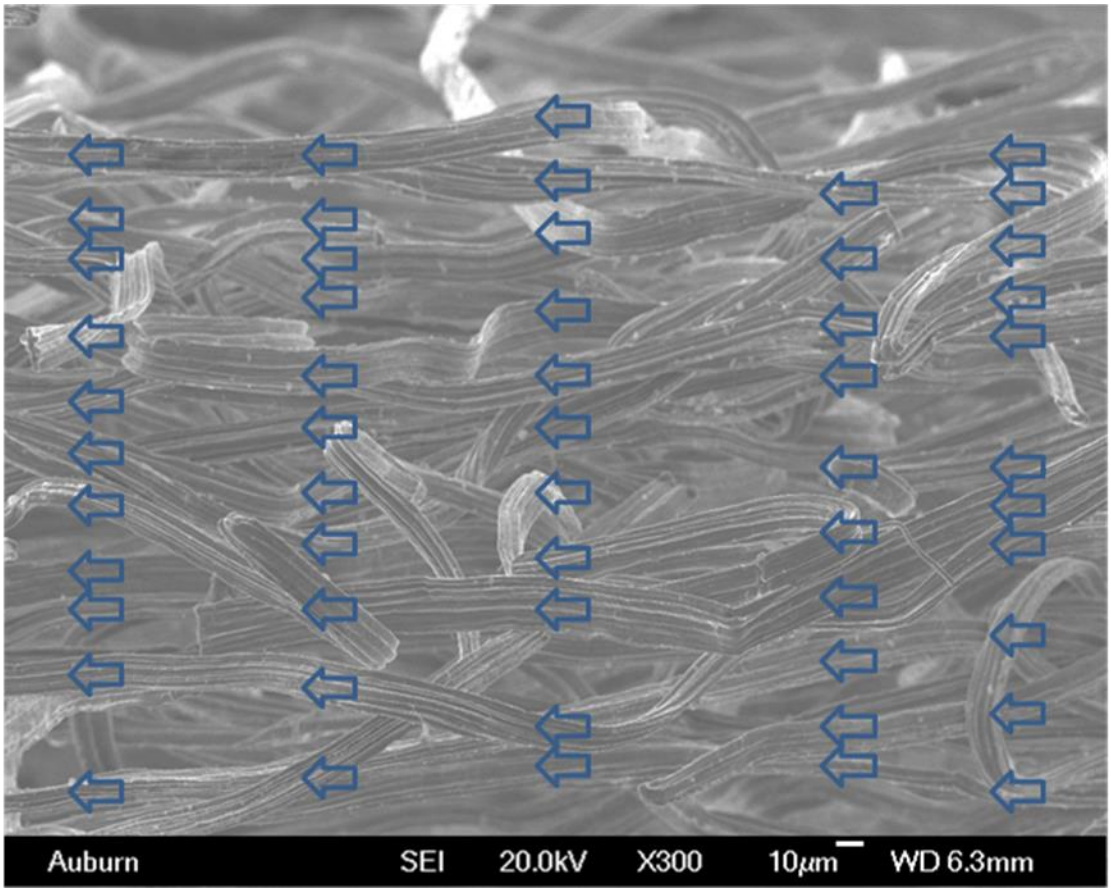

Figure II-8. Side SEM imaging of microfibrous material for average fiber spacing determination

II.5. Pressure drop modeling by FLUENT

II.5.1. Fiber only

In this research, pressure drop from 10-40 m/s flow was tested for microfibrous material. Though Reynolds number in the test rig ranges from 50,000-250,000, the

Reynolds number within the test media is fairly small. This means flow in the duct is turbulent, while flow in the test media is still transition region. Since *Hills et al.* has studied flow type in this Reynolds number range and determined it to be weakly turbulent, the simulation is carried with a turbulent model.

For the simulation, the air property is at 200℃, which corresponds to 0.75 cc/g of density and $3.5*10^{-5}$ m^2/s of viscosity. The velocity is simulated using second order upwind method and outlet pressure is set at 1 atm. Since this simulation is only a disassembled part from the whole media sheet, all boundaries for the simulation are set to be symmetric so that no wall effect will be shown for the pressure drop and velocity profile simulation.

The pressure drop across a blank 8μm nickel fiber was first simulated. The fiber material used is 1.2% in volume loading. The distance between fibers is determined by SEM imaging method. The simulation applied for four layers of unit cell (Figure II-9), which is 1.1 mm (Figure II-10). Experimental tests are based on 4 mm thick fiber sheet and these results will be compared on a pressure drop per millimeter basis.

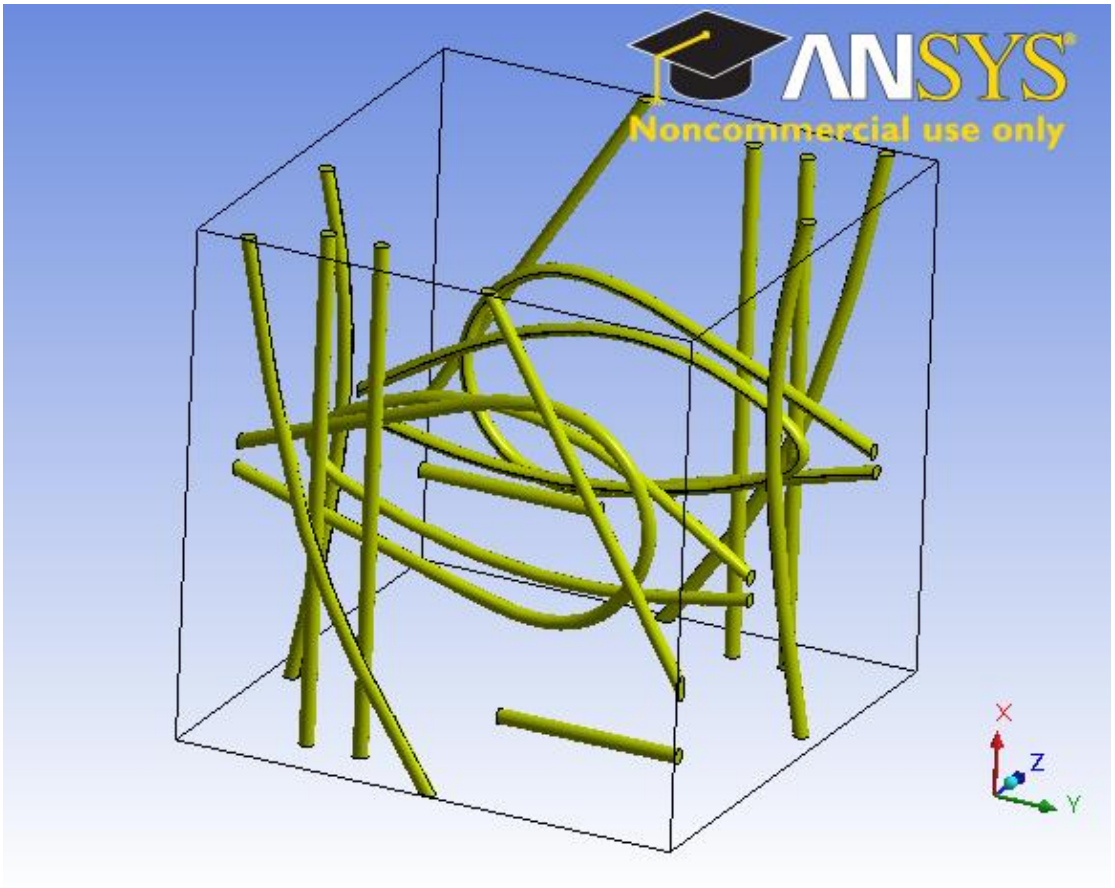

Figure II-9. Unit cell of fiber material only for CFD simulation; fiber volume loading 1.5%; 10 layers in a unit cell

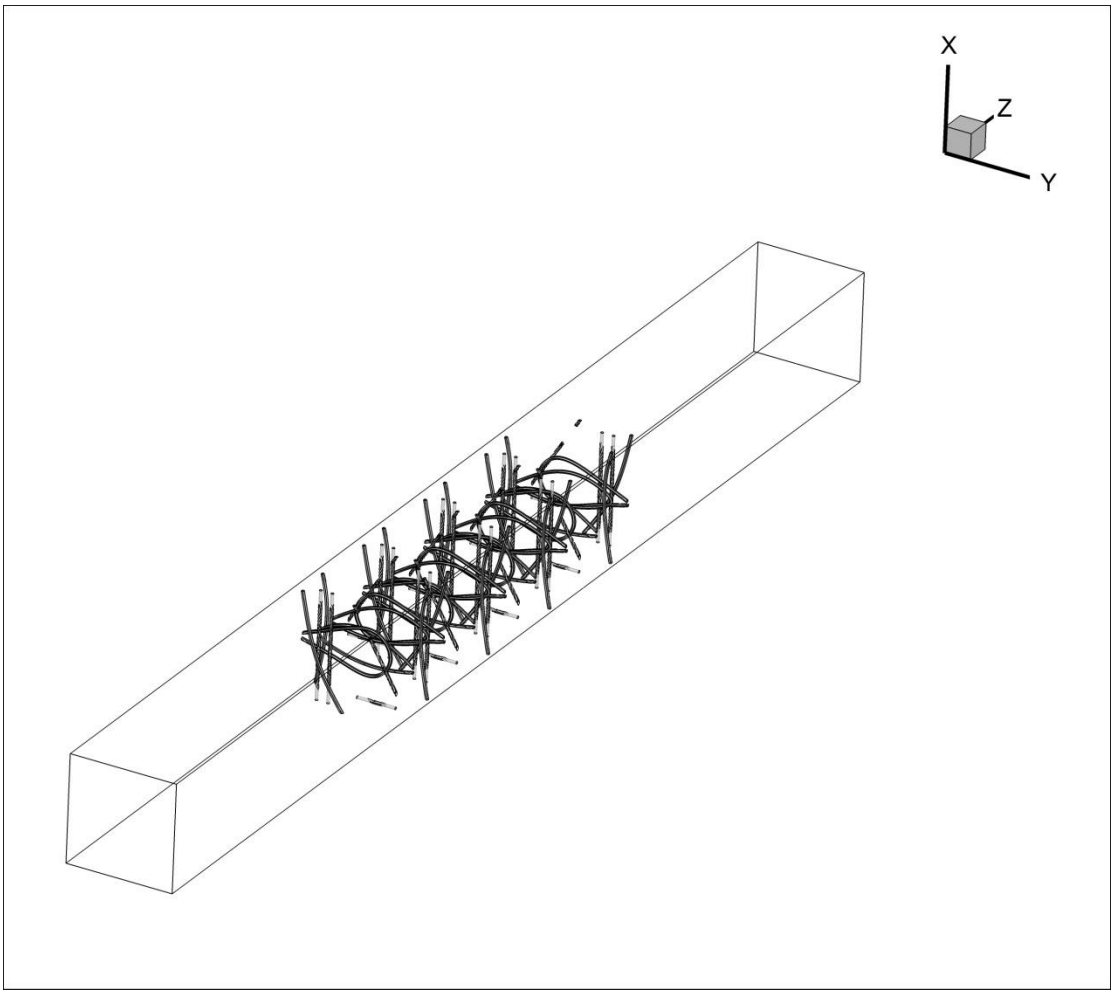

Figure II-10. Four unit cell attached together for CFD simulation with bare section connected to upstream and downstream for a fully developed flow; fiber volume loading is 1.5%; fiber section length is 1.1 mm, bare section is 1.0 mm each, total length is 3.1 mm

Figure II-11 shows a sample simulation of pressure drop across fibrous media. Inlet velocity is at 10 m/s and total pressure drop 2750 Pa/mm. The simulation is repeated at 5 and 15 m/s; quadratic pressure drop is shown in Figure II-12. In the media region, the

pressure drop shows gradual reduction throughout the region. This can be explained by gradual contraction across this region, since contraction is known to contribute to pressure drop.

The simulation result is compared with experiment result in Figure II-12. Both experiment and simulation result showed quadratic pattern of pressure drop at these high velocities. However, the simulation result showed a deviation from the experiment data, especially at higher face velocities. The deviation is expected because the metal fiber is under compression at high face velocities since high pressure difference exists at two sides of the fiber media. This effect will be studied in a later section of this research, which serves to increase the accuracy of this pressure drop model.

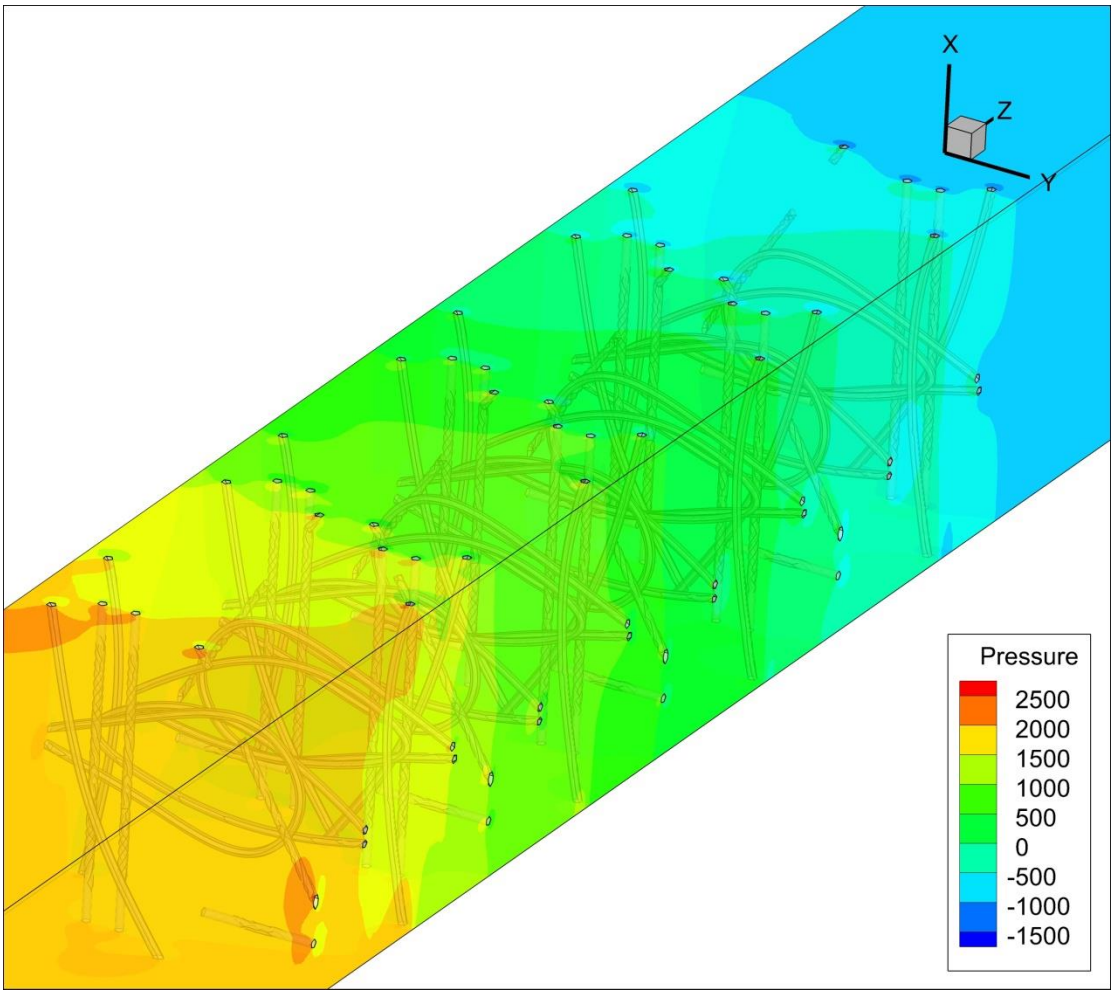

Figure II-11. Pressure drop simulation result for fiber only situation in a four-unit cell series with bare section connected to each end; upstream pressure is bulk pressure in bare section, 2250 Pa; Downstream pressure is bulk pressure in bare section, 0 Pa

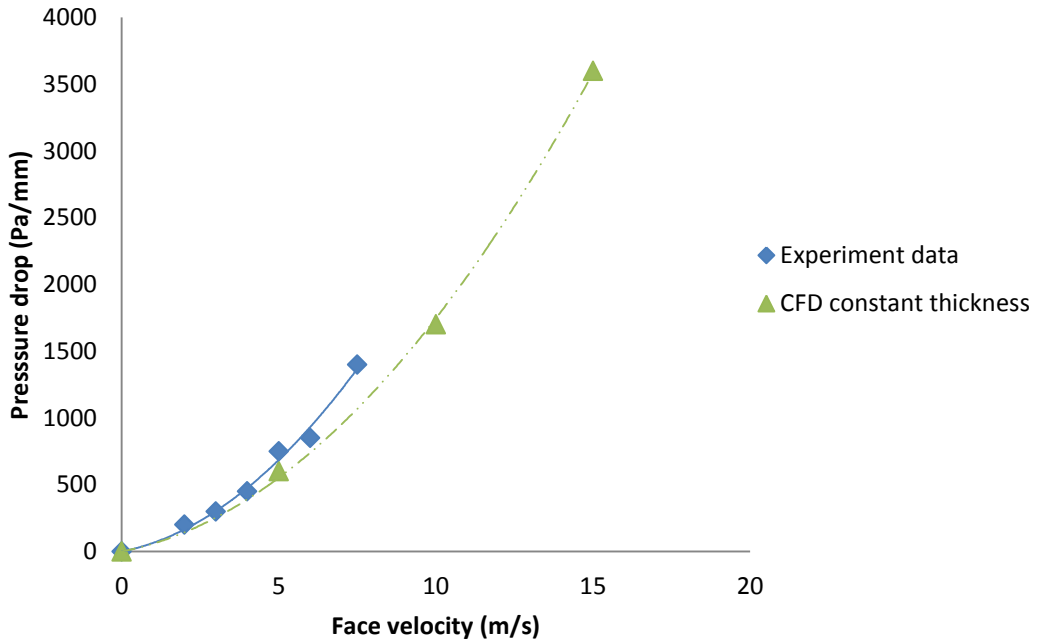

Figure II-12. Pressure drop comparison between the model and experiment data

II.5.2. Fiber with round particles

Since volume loading of particles in entrapped fiber sheets is much higher than fiber itself, the particles contribute to a large portion of pressure drop to the total pressure drop of the sheet. Typically volume loading of particles ranges from 20% - 30% for metal fiber sheet. In this application, particle volume loading is set at 20%. Particles used are ground and sieved to 150-250 μm. In this part, the particles are assumed to be ideal in shape (sphere) and average in size (200 μm). In the simulation, the particles are sketched

as spheres with surfaces defined as wall conditions. Other simulation criteria are the same as fiber-only case. Figure II-13 shows SEM imaging of particle-entrapped fiber media, which is sketched in Figure II-14 as simulation unit cell.

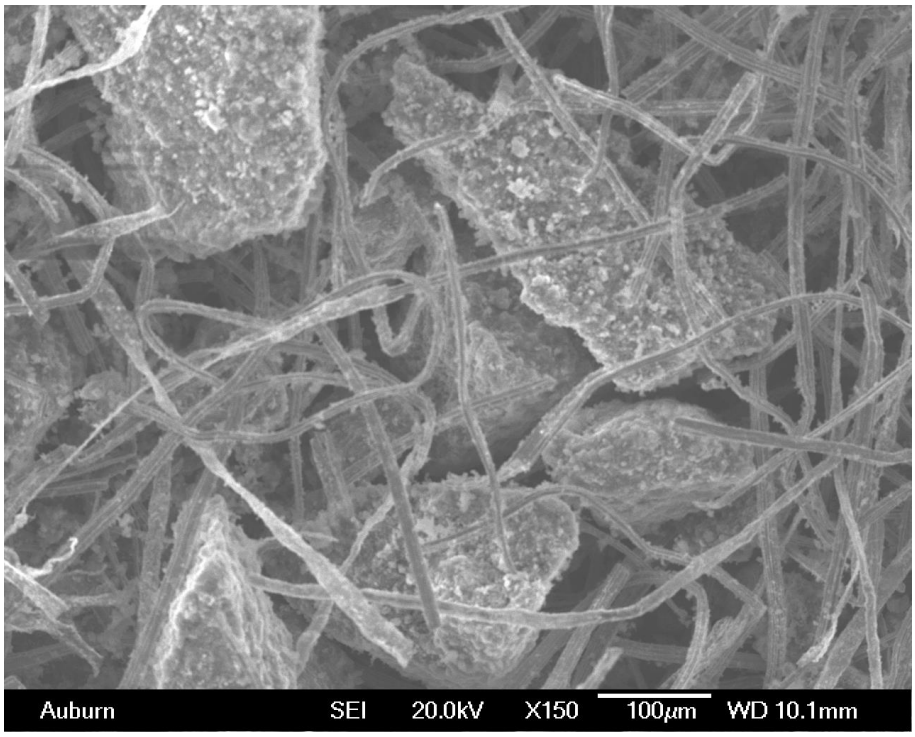

Figure II-13. SEM imaging of an entrapped particle microfibrous sheet surface; 8μm & 150-250 μm alumina particles entrapped

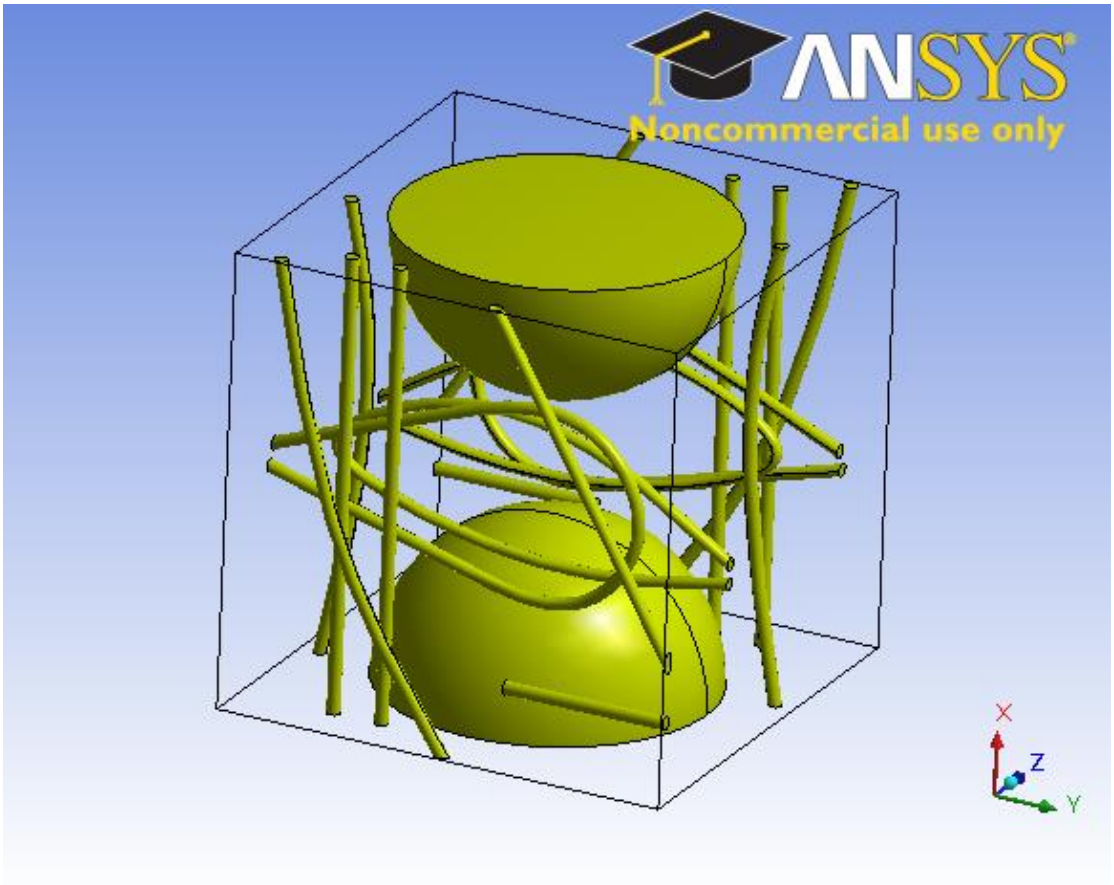

Figure II-14. Unit cell of entrapped sphere particle situation for CFD simulation; particle volume loading 20%; fiber volume loading 1.5%, 10 layers in a unit cell

Then the unit cells are stacked into a four-in-series structure for pressure drop simulation (Figure II-15). Bare sections are left both upstream and downstream within the simulated area so that flow can be fully developed before entering the fibers and immediately after the fibers. In actual simulation, four unit cells are attached together for pressure drop and the result is compared with experiment result on a pressure drop per millimeter media basis.

Figure II-16 shows a sample simulation of pressure drop across fibrous media. Inlet velocity is at 10 m/s and total pressure drop 3750 Pa/mm. The simulation is repeated at 5 and 15 m/s for pressure drop properties. This simulation result will be contrasted considering shape factor so that the importance of shape factor is demonstrated.

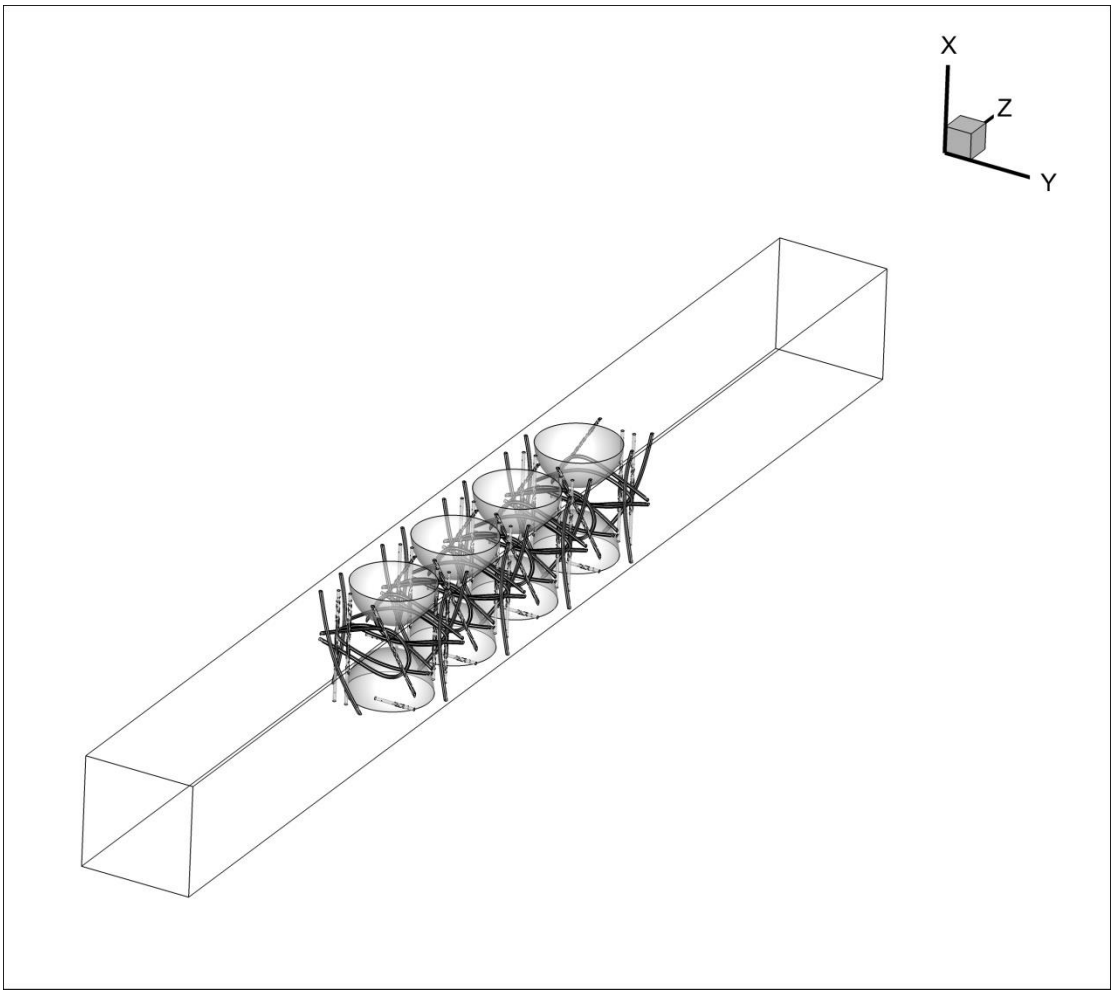

Figure II-15. Four round particle unit cell attached together with bare section connected to upstream and downstream for a fully developed flow; fiber section 1.1 mm, bare section 1.0 mm each for upstream and downstream; total length 3.1 mm

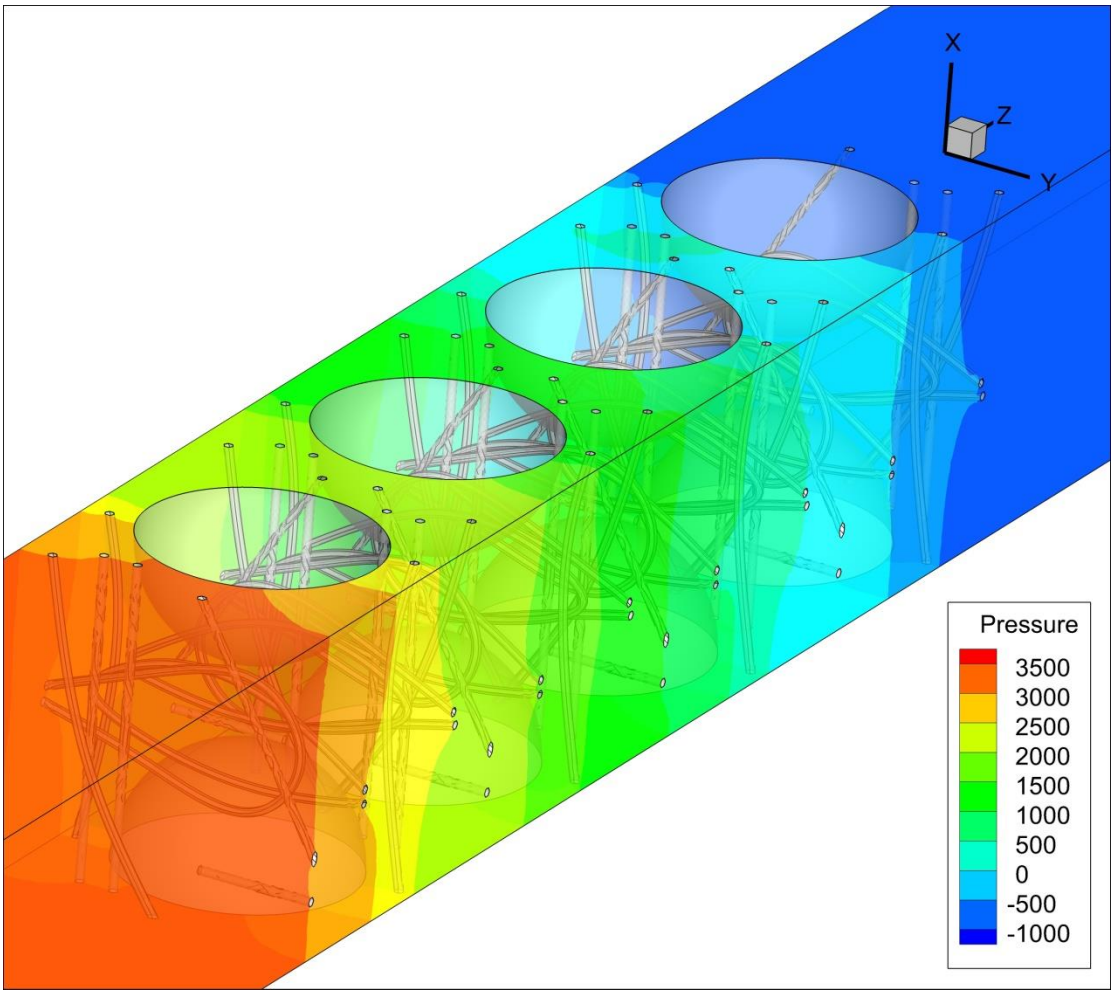

Figure II-16. CFD pressure drop simulation result for fiber material entrapped with round particles, four unit cells attach together and bare section up and down stream; upstream pressure is bulk pressure in bare section, 3750 Pa; downstream pressure is bulk pressure in bare section

II.5.3. Fiber with elliptic particles

Shown by SEM imaging, shape of entrapped particles is not perfectly round. In this simulation, shape factor also known as sphericity has been investigated for contribution to the total pressure drop of the fiber material. Karwa *et al.* have empirically obtained shaped factors using Blake Kozeny equation for microfibrous material (Table II.1). In this research, 180-210 μm particles are used and shape factor of 0.8 was chosen as simulation criteria.

Table II.1 Measured shape factor using Blake Kozeny equation for various components of MFEC

Particles/fibers	Shape factor (Φ)	Solid fraction during measuring 'ϕ'
90–125 μm particles	0.77	0.62
180–210 μm particles	0.80	0.62
500–600 μm particles	0.74	0.62
4 μm fibers	1.09	0.39
8 μm fibers	1.09	0.41
12 μm fibers	1.04	0.40

Close investigation of SEM imaging of the particles reveals that the shape of particles is in great approximation to a sphere (Figure II-17), only sharp at two ends in most cases. This shape is best simulated with an ellipsoid. Then the volume and

sphericity equations are solved for dimensions of the simulation ellipsoid, assuming that particle volume remain unchanged.

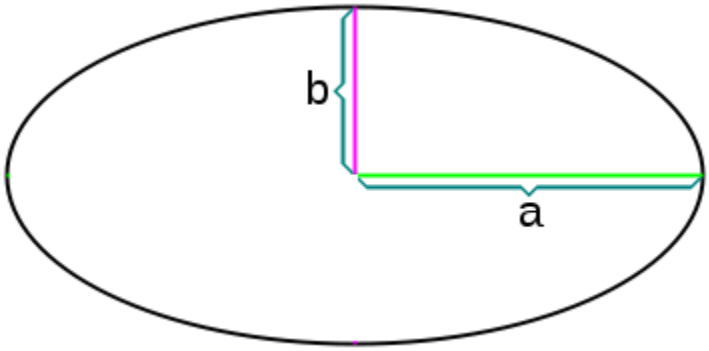

Figure II-17. Illustration of simulated ellipsoid; volume equal to the volume of a 200 μm diameter sphere, shape factor 0.8

$$\Phi = \frac{\pi^{\frac{1}{3}}(6V_p)^{2/3}}{A_p} = \frac{2\sqrt[3]{ab^2}}{a+\frac{b^2}{\sqrt{a^2-b^2}}\ln(\frac{a+\sqrt{a^2-b^2}}{b})} \quad (10)$$

$$V = \frac{4}{3}\pi ab^2 \quad (11)$$

With same volume loading of particles as round particles and shape factor of 0.8 for entrapped particles, the calculated result for a and b for the ellipsoid is 206μm and 69μm. Then the ellipsoid is arranged in a style that the particles are mostly dispersed. The sketch for simulation is shown in Figure II-18. The fiber layout of the unit cell is the same as previous fiber only and fiber with round particle situation; only the particles are more realistic than round particles.

Then the unit cells are stacked into a four-in-series structure for pressure drop (Figure II-19). Bare sections are left both upstream and downstream within the simulated area so that fluid can be fully developed before entering the fibers and immediately after the fibers. According to Blake Kozeny equation, the expected pressure drop for lower shape factor particles will be higher due to the shape irregularity. This criteria can be used to compare the previous round particle simulation and verified by determining which simulation best approximates the experiment result. Simulation result is compared with experiment on a pressure drop per millimeter media basis.

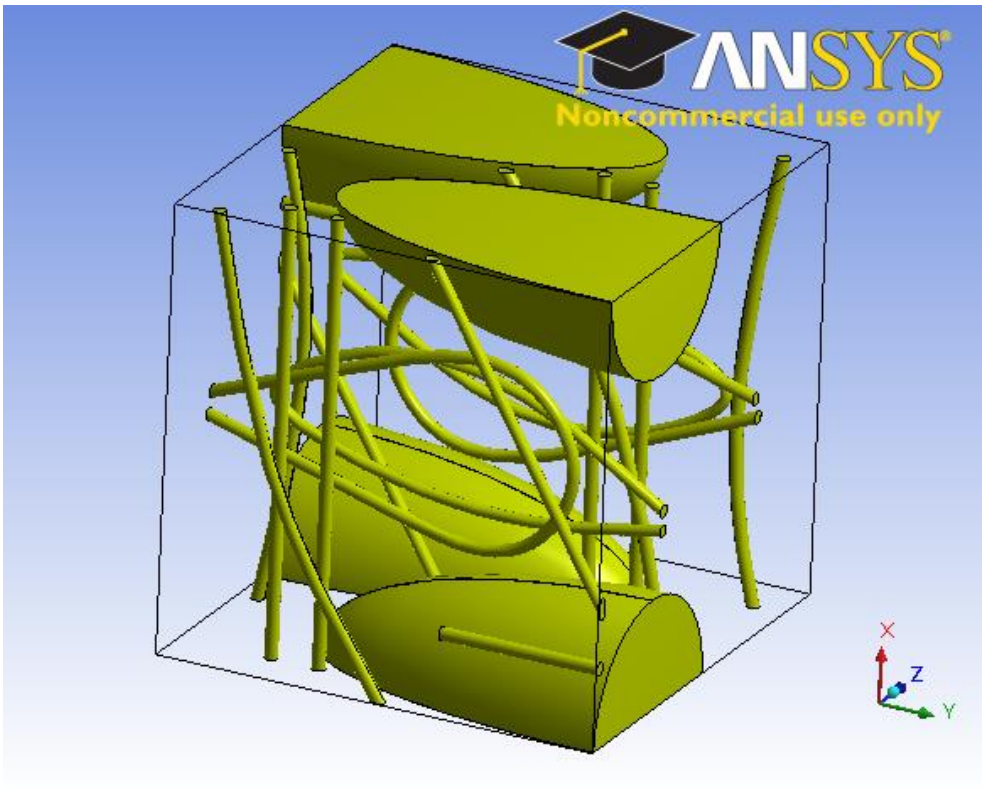

Figure II-18. Unit cell of entrapped ellipsoid particles for CFD simulation; particle volume loading 20%; fiber volume loading 1.5%, 10 layers of fiber in a unit cell

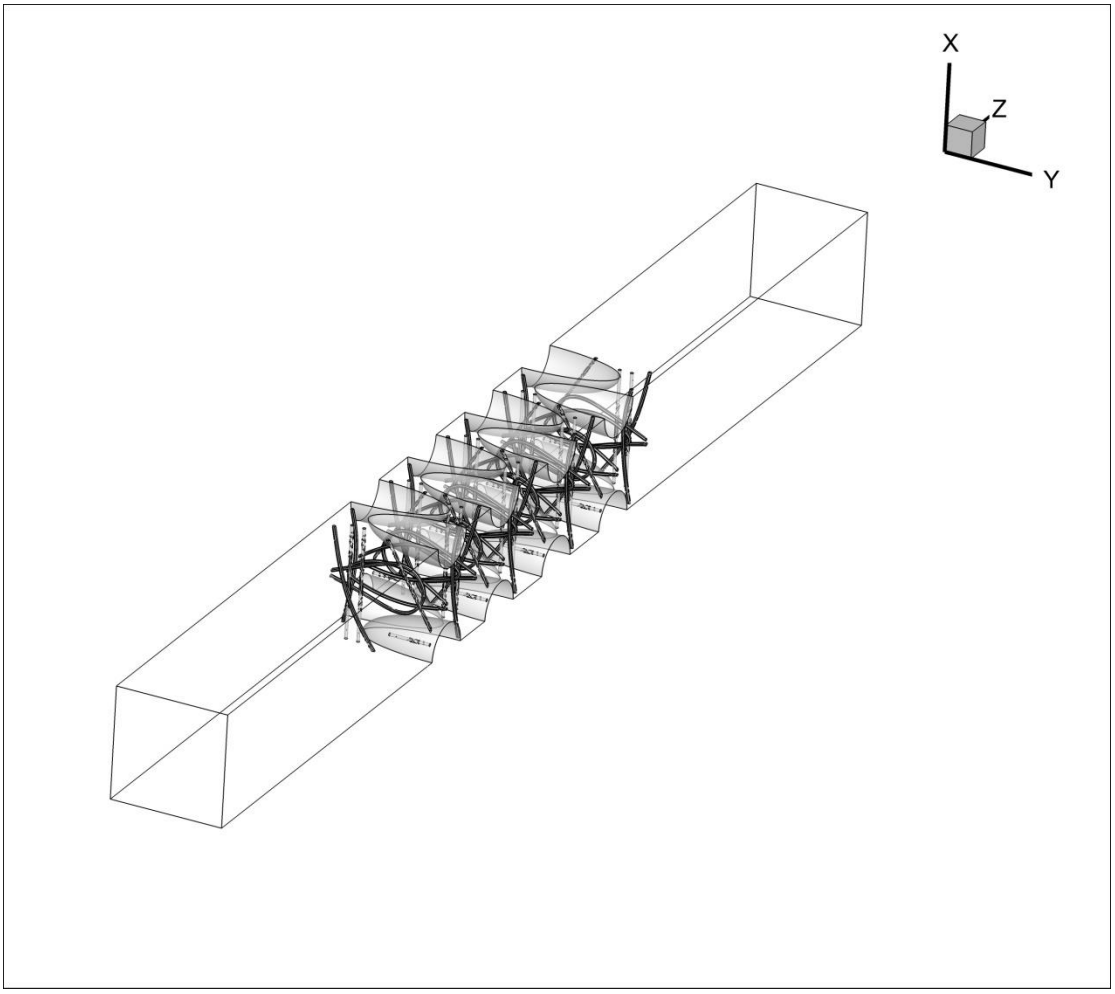

Figure II-19. Four ellipsoid particle unit cell attached together with bare section connected upstream and downstream for a fully developed flow; fiber section 1.1 mm, bare section 1.0 mm each for upstream and downstream; total length 3.1 mm

Figure II-20 shows a sample simulation of pressure drop across fibrous media with elliptic particles. Inlet velocity is at 10 m/s and total pressure drop 4250 Pa/mm. The simulation is repeated at 5 and 15 m/s; quadratic pressure drop is shown in Figure II-21.

The simulation result is also compared with experiment result in Figure II-21. Both experiment and simulation results show quadratic pattern of pressure drop at these high velocities. By comparing the round and elliptic particle simulation, it is shown that the elliptic simulation result is better in approximating the experiment result, which proves the previous statement that lower shape factor contributes to larger pressure drop. However, the simulation is smaller in pressure drop than experiment due to the media compression.

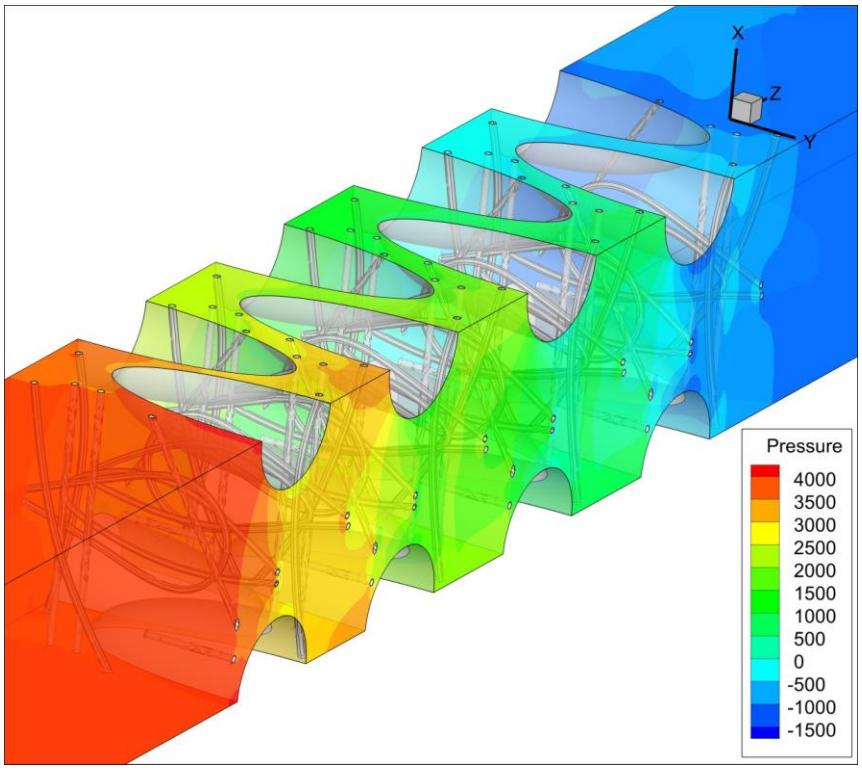

Figure II-20. CFD pressure drop simulation result for fiber material entrapped with round particles, four unit cells stacked together and bare section up and down stream; upstream pressure is bulk pressure in bare section, 4250 Pa; downstream pressure is bulk pressure in bare section

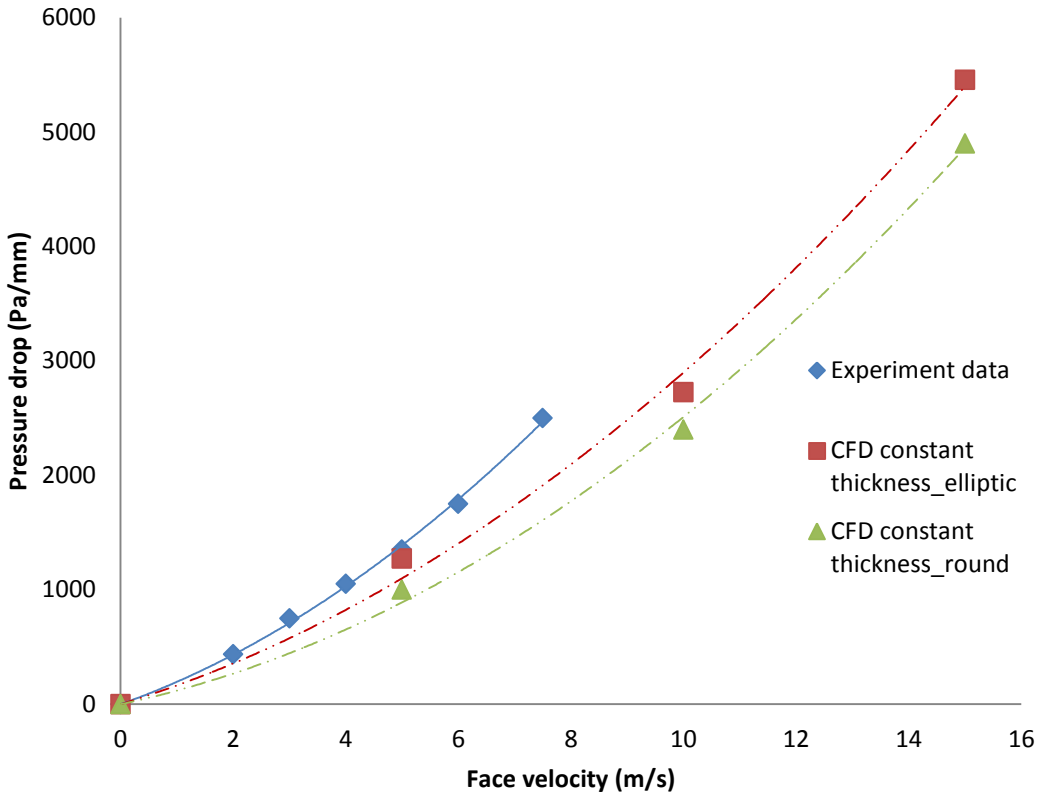

Figure II-21. Pressure drop comparison of experiment, round particle and elliptic particle media by CFD simulation

II.6. Fiber compressibility

Volume loading of different components substantially changes the pressure drop property of a fiber material. When tested at high face velocities, the pressure difference at two sides of the fiber material does compress the fiber material. The compression causes

a temporary volume loading change of the fiber component. To take these effects into consideration, fiber thickness is tested at different pressures using a thickness measuring machine. Wang *et al*. has suggested that fiber thickness is a linear function of the applied pressure. Linear regression of media thickness at different pressures is then transferred to thickness vs. velocity profile for simulation purposes, using the pressure drop data obtained experimentally for flat sheet microfibrous materials.

To improve CFD model accuracy, fiber and particle spacing has been adjusted according to the thickness tested. Due to the volume loading increment of fibers and entrapped particles, the pressure model accuracy has been improved dramatically especially at higher face velocities because of the larger compressions at these velocities.

The media thickness tests using thickness machine is shown in Figure II-22. Linear regression is observed for both fiber only and entrapped particle cases. It is shown that the media compresses up to 20% in thickness in operating conditions. These compression data are applied to fiber-only case (Figure II-23) and fiber with entrapped particle cases (Figure II-24). For media-only case, the adjusted thickness pressure drop shows good consistency with experiment result. For entrapped-particle cases, the elliptic simulation is more accurate since it takes the shape factors into consideration. The shape factor contribution to the total pressure drop can be distinguished by comparing the experiment result and round particle simulation. Since the volume loading of fibers in the

media is relatively small and shape factor of fibers is close to one in most cases, shape factor is not considered for fibers in this simulation.

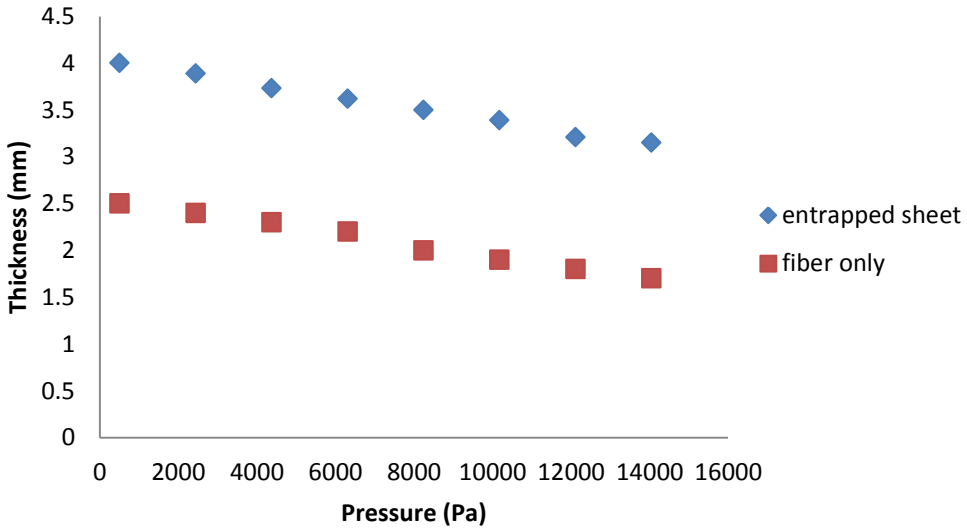

Figure II-22. Microfiber media thickness at different pressures; initial volume loading, fiber 1.5%, particles 20%; initial thickness 4 mm

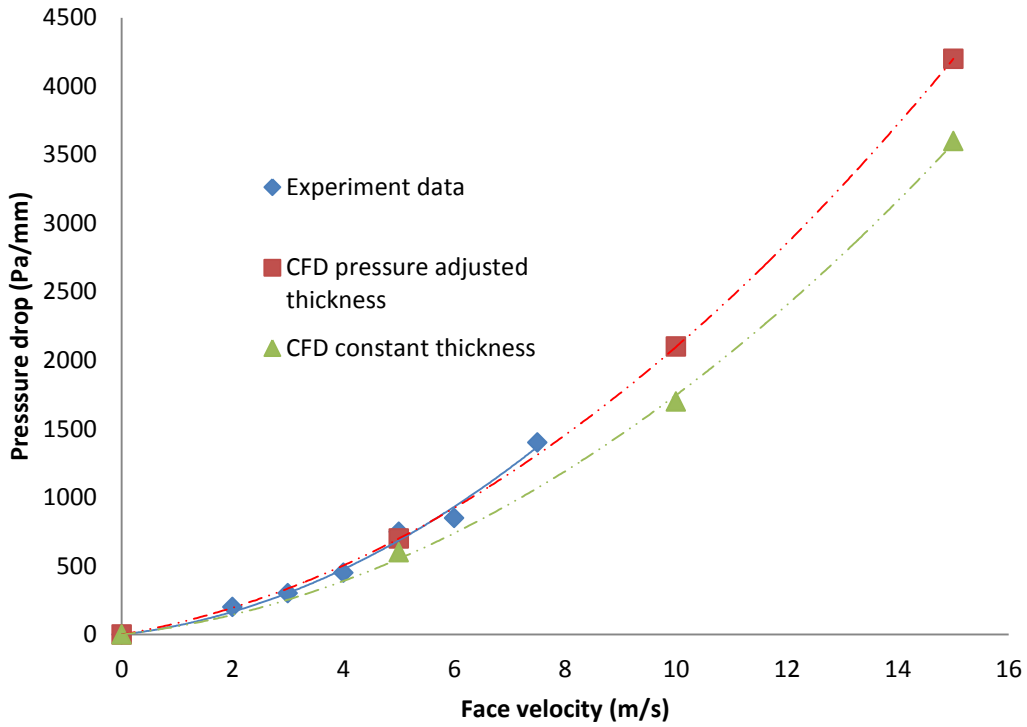

Figure II-23. Pressure drop for fiber-only case; CFD simulation in both uncompressed and compressed consideration; experiment result collected up to 7.5 m/s due to limitation of air supply; data fitted with second order polynomial

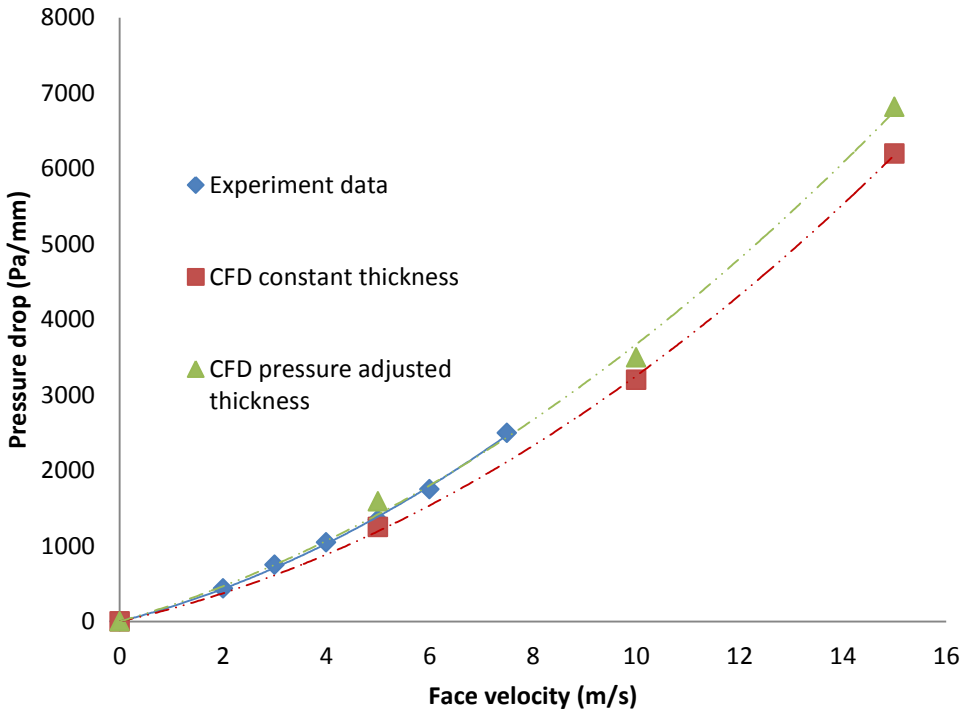

Figure II-24. Pressure drop for fiber with elliptic particle case; CFD simulation in both uncompressed and compressed consideration; experiment result collected up to 7.5 m/s due to limitation of air supply; data fitted with second order polynomial

II.7. Pressure drop for pleated MFEC using micro scale data

The previous analysis using micro scale method precisely predicts pressure drop for certain properties of fibers and particles at high Reynolds numbers. As mentioned before, the gigantic difference in the dimension of pleat structure, fiber sheet and fiber and particles made it impossible to predict the whole filter pressure drop using CFD.

However, by simulating at different speeds of the micro scale structure, a quadratic form of pressure drop (Forchheimer law) curve can be obtained for each fiber sheet. This curve is then used as property of porous zones in filter simulations. In this way, the dimension difference is connected by treating the same porous media in both micro and macro scope. It is important to mention again that this situation is only applied to high Reynolds number cases where average face velocity profile resembles plug flow.

Figure II-25. Picture of no fairings added to the pleat tip of microfibrous media filter; fairings at upstream when running tests

In high volumetric tests, the microfibrous media is engineered into pleat structure to reduce pressure drop. These structures help with reduction of amount of air going into each of the pleats. The pressure drop and velocity profile for these complicated structures are simulated using previous flat sheet simulation results. In addition, the pleat structure has brought in pleat tips which increase the total pressure drops. Fairing added

to the pleat tip has been tested experimentally and by simulation using FLUENT CFD to explain the benefit of those fairings.

First, pleated MFEC filter without fairings is simulated using elliptic particle simulation result with thickness adjustment. All surfaces including channel and pleat tips are defined as wall conditions in simulation. MFEC is defined as porous zone using previous simulated data.

By observing filters without fairing simulation, it is found that upstream there exist high pressure spots at the pleat tips which are much higher than the bulk pressure upstream, and downstream there exist low pressure spots which are lower than the bulk pressure downstream (Figure II-26). These spots are more clearly shown in pressure values at stream-wise direction figure (Figure II-27). These extreme pressure spots all contribute to the increased total pressure drop and energy consumption, since a higher pressure environment has to be created by blower/engine for the system to reach required face velocity. When looking at the velocity profile (Figure II-28), the extreme pressure spots are created by the flow diversion at the upstream pleat tip and vortex flow forms at the downstream, which is very similar to the sudden contraction and expansion in pipe flows.

The pressure drop for MFEC filter without fairings is obtained. Figure II-29 shows experimental data tested for MFEC filter without fairings at three temperatures. Simulations are compared with these experiment results. Figure II-30 shows the

comparison at 200℃. The simulation result is in good consistency with experimental data. This case will serve as the basis for observing the effect of adding fairings, since any change in pressure drop will be solely from the fairings.

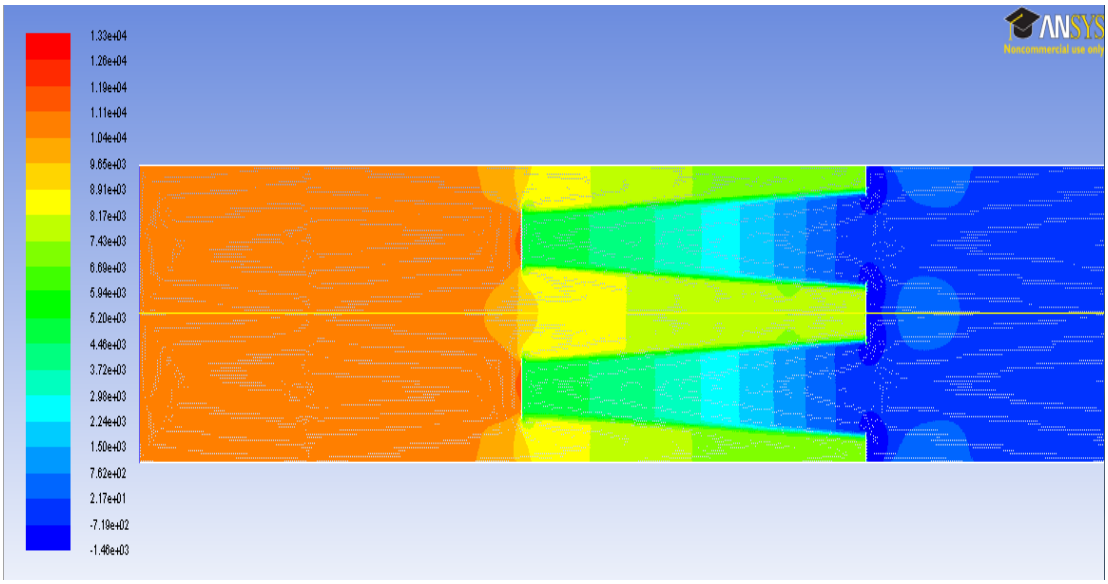

Figure II-26. Pressure drop simulation for pleated microfibrous material filter; high pressure spot at upstream pleat tip; low pressure at downstream pleat tip; overall pressure drop increased due to sudden contraction and expansion upstream and downstream

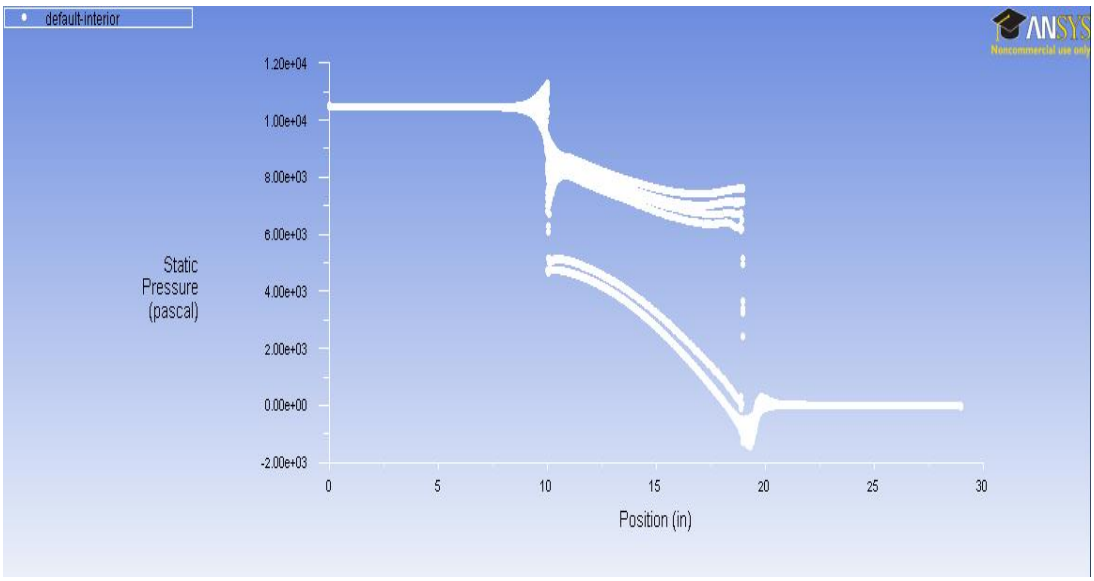

Figure II-27. Pressure value at stream wise direction; downstream bulk pressure @ 1 atm; total pressure drop @$1.05*10^4$ Pa

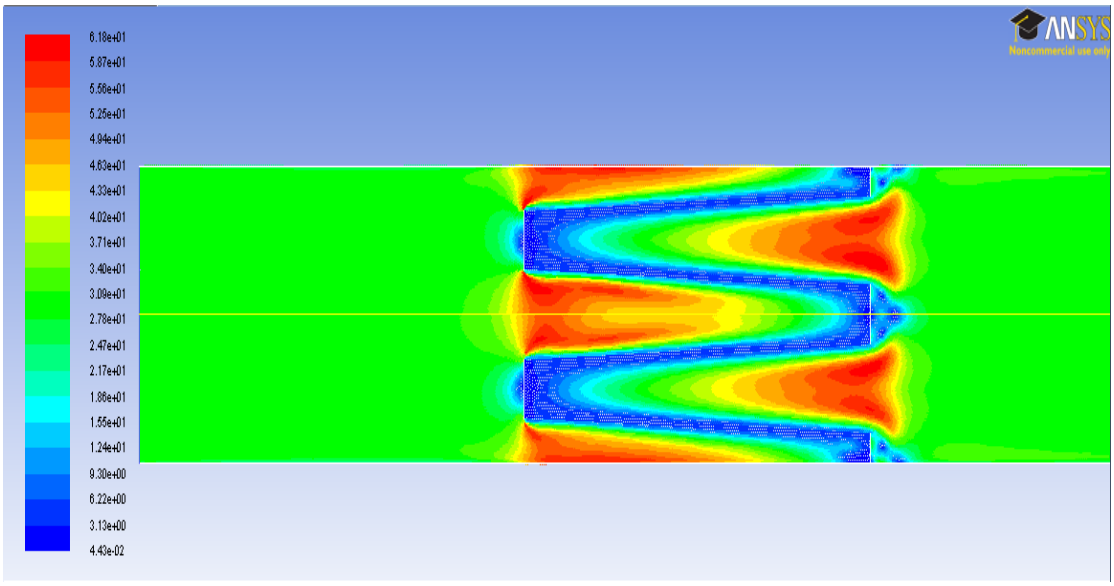

Figure II-28. Velocity profile for pleated microfibrous material filter; eddy flow at pleat tip of both upstream and downstream

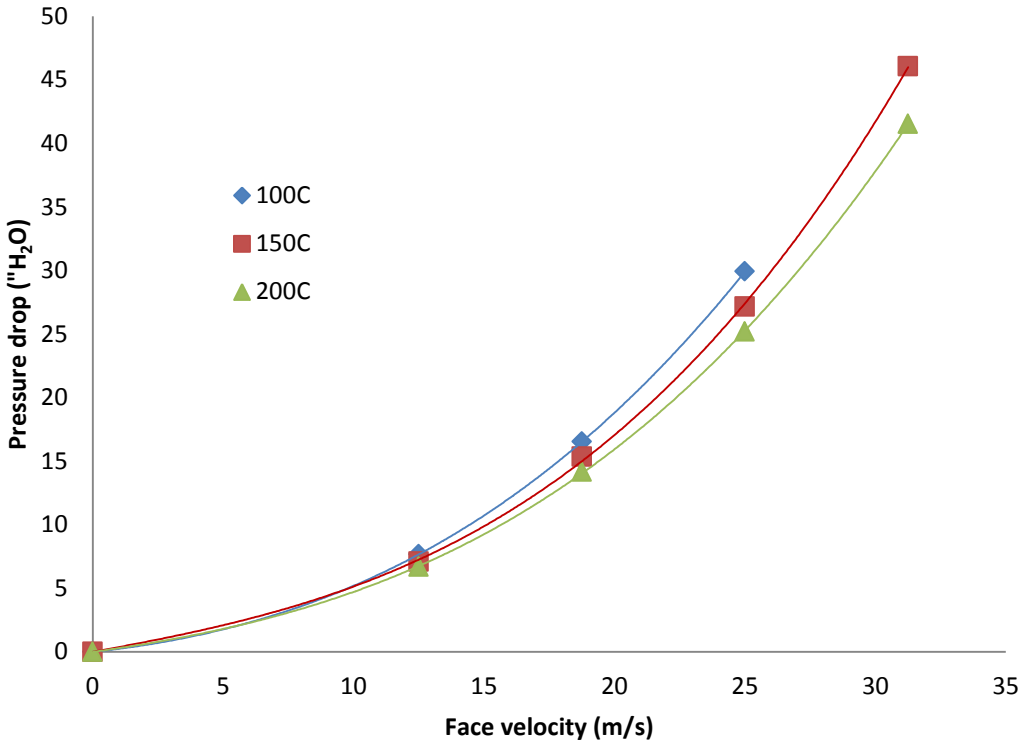

Figure II-29. Pressure drop of Microfibrous media without fairings added at three temperatures

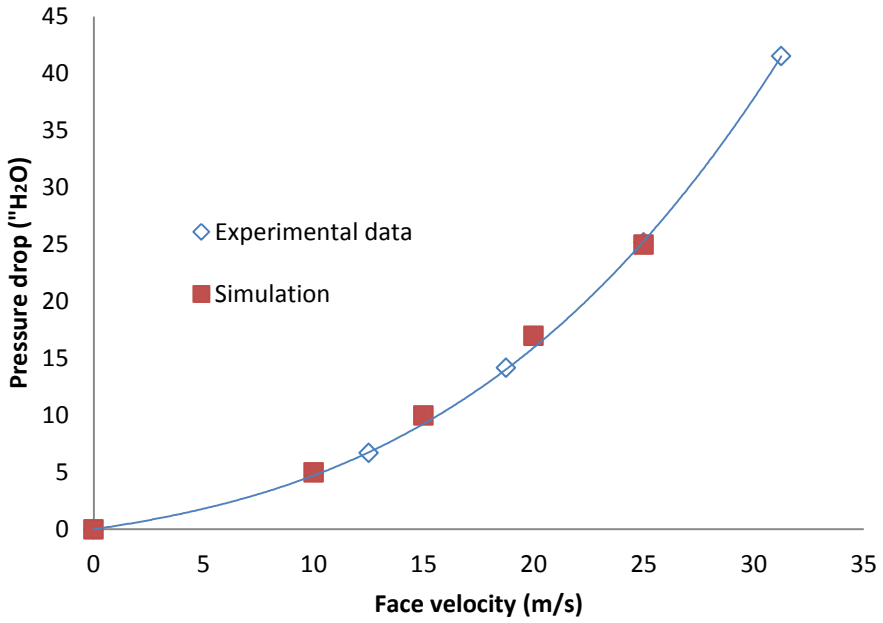

Figure II-30. Pressure drop comparison of experimental data and simulation results; Temperature @ 200℃

To help with the total pressure drop, extreme high and low pressure spots have to be minimized or removed. Since the situation is similar to sudden contraction and expansion in pipe flow, the solution is also similar, which is to make the change progress smoothly. This can be done by adding fairings. At upstream, adding fairings is expected to help the air compress gradually before reaching the fibrous media. At downstream, by helping the expansion progress gradually, the vortex flow should be minimized.

First, round top fairings are added. Figure II-31 shows a pleated MFEC filter with round-top fairings added upstream. Since the first touch point on the filter by the

flow is reduced from a flat surface pleat tip to the top spots of the round top of the fairings and gradually increasing to the same area as the pleat tip surface, flow contraction is smoother and high pressure spots should be minimized. Simulation result did prove the previous hypothesis (Figure II-32). However, the gradual compression still progresses too quickly, meaning the pressure reduction only exists at the tip of the fairing. This is more apparent by investigating Figure II-33, which shows the pressure values at the stream-wise direction. It is observed that pressure increase at the tip is smaller compared with the case without fairings. But pressure drop near the fairing tip is still not smooth. By investigating the fairing tip, we still find similar velocity distribution as with no fairing (Figure II-34), only with smaller areas. Much of the depth of the fairing has little effect with the round-top fairings. But, the gradual change effect does reflect in the total pressure drop. By comparing the total pressure drop with the case of no fairings added to either tip, the total pressure drop reduces 500 Pa at 30 m/s of velocity and 200℃ of temperature.

The simulation result is compared with experimental for this structure. Figure II-35 shows experimentally determined pressure drop for this structure at three temperatures. Figure II-36 compares the simulation and experiment at 200℃, which shows good consistency.

Figure II-31. Picture of two round-top fairings added to the pleat tip of microfibrous media filter; fairings at upstream when running tests

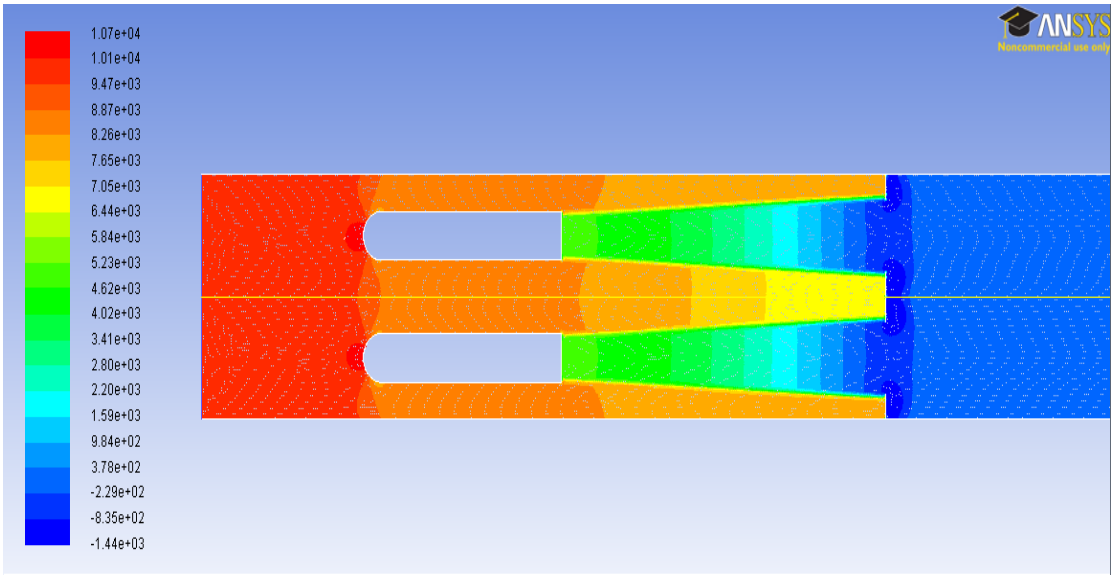

Figure II-32. Pressure drop simulation for pleated microfibrous material filter with round-top fairings at upstream; smaller high pressure spot at upstream tip; reduced overall pressure drop compared with no fairings

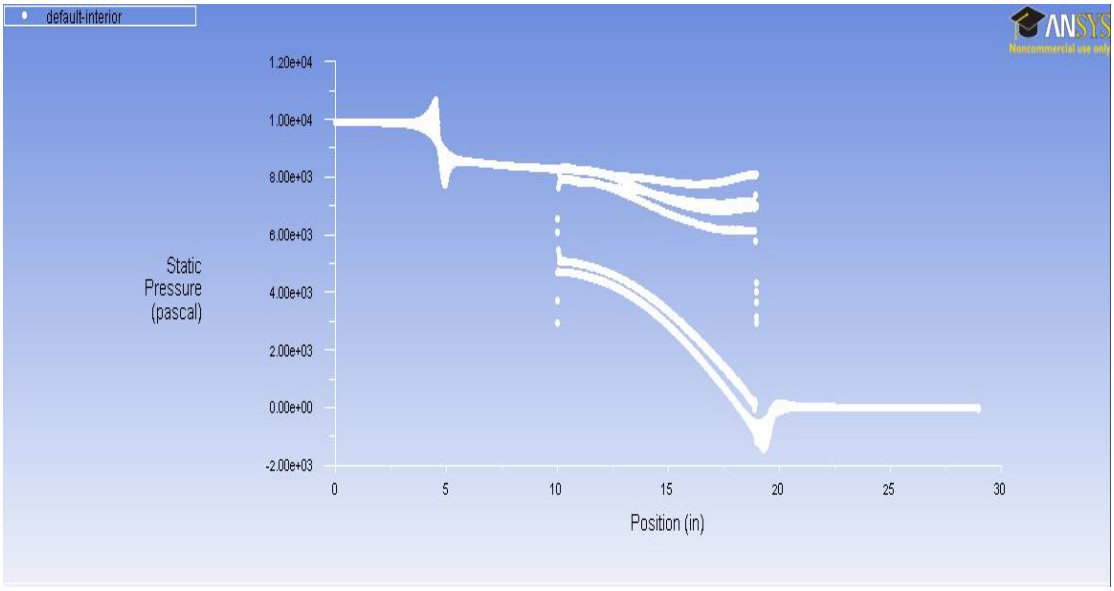

Figure II-33. Pressure value at stream wise direction; downstream bulk pressure @ 1 atm; total pressure drop @$1.0*10^4$ Pa

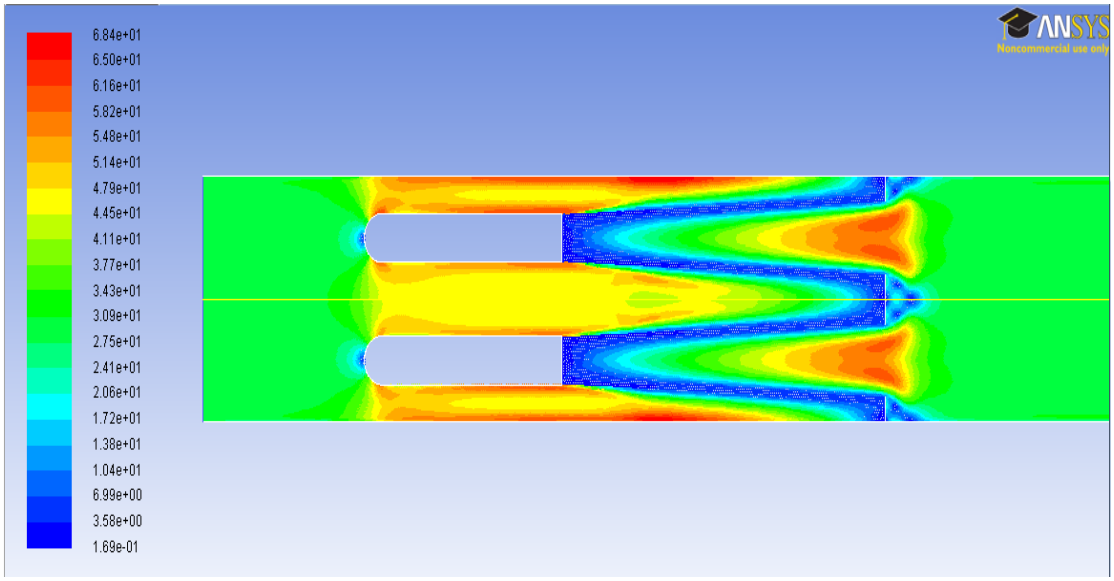

Figure II-34. Velocity profile for pleated microfibrous material filter with round-top fairings; eddy flow removed by added fairings

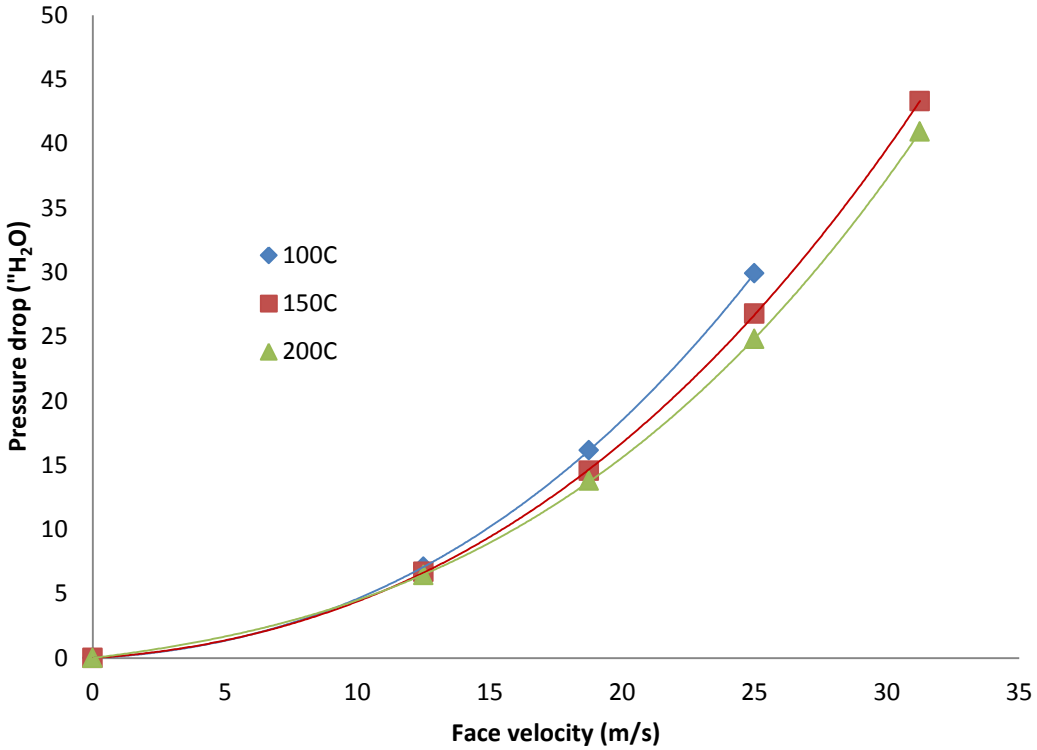

Figure II-35. Pressure drop of Microfibrous media with round-top fairings added at three temperatures

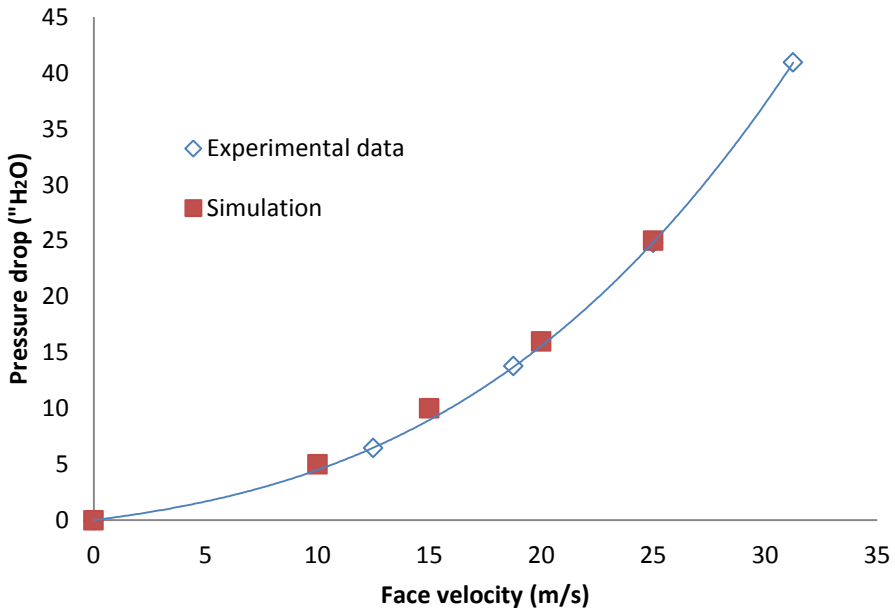

Figure II-36. Pressure drop comparison of experimental data and simulation results; Temperature @ 200℃

Since the round-top fairings help with the gradual pressure change only at the tip part, a smoother way to change the pressure is needed. Triangle fairings are brought to attention, because fairings expand constantly from the top to the end, which will be the optimum choice for gradual compression of the air. Figure II-37 shows triangle fairings added to the upstream of a pleated microfibrous material filter. Figure II-38 is the corresponding simulation for pressure drop. As the pressure drop simulation indicates, there is no apparent high pressure spot existing upstream. Comparing figure of pressure value at the stream wise direction (Figure II-39) with previous simulation result, it is apparent that by adding triangle fairings the pressure drop progresses much more

smoothly, leading to a removal of the high pressure spots. Also, for the velocity profile upstream (Figure II-40), no apparent flow diversion was found, which means the flow changes direction and is being compressed gradually.

Since the high pressure spots were successfully removed upstream, it is expected that the total pressure drop with the triangle fairings performs better than that with round-top fairings. Figure II-41 shows the experimentally determined pressure drop for MFEC filter with triangle fairings at three temperatures. Compared with round-top fairings, a 300 Pa greater pressure drop was removed at 200℃. The simulation result is also compared with experiment data at 200℃ for model accuracy check in Figure II-42.

Figure II-37. Picture of two triangle fairings added to the pleat tip of microfibrous media filter; fairings at upstream when running tests

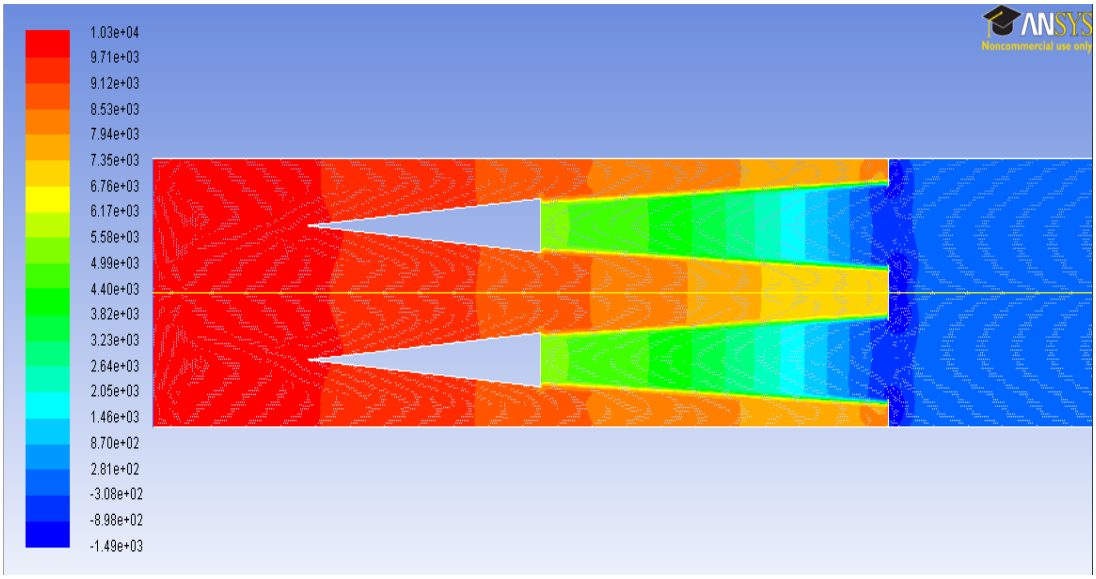

Figure II-38. Pressure drop simulation for pleated microfibrous material filters with triangle fairings at upstream; no apparent high pressure spot observed; reduced overall pressure drop compared with round-top fairings

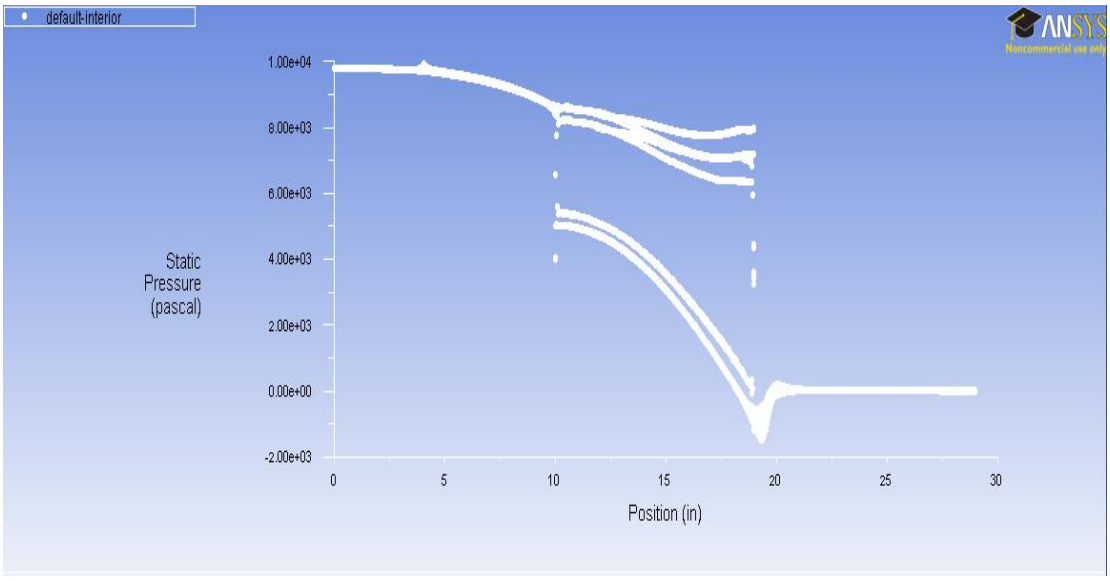

Figure II-39. Pressure value at stream wise direction; downstream bulk pressure @ 1 atm; total pressure drop @$9.7*10^3$ Pa

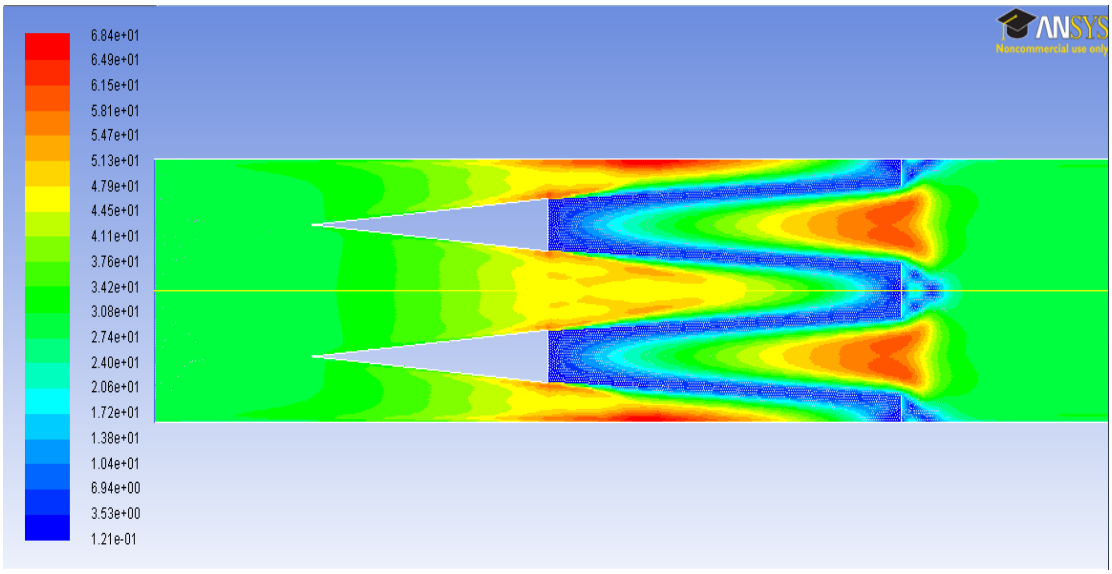

Figure II-40. Velocity profile for pleated microfibrous material filter with triangle fairings at upstream

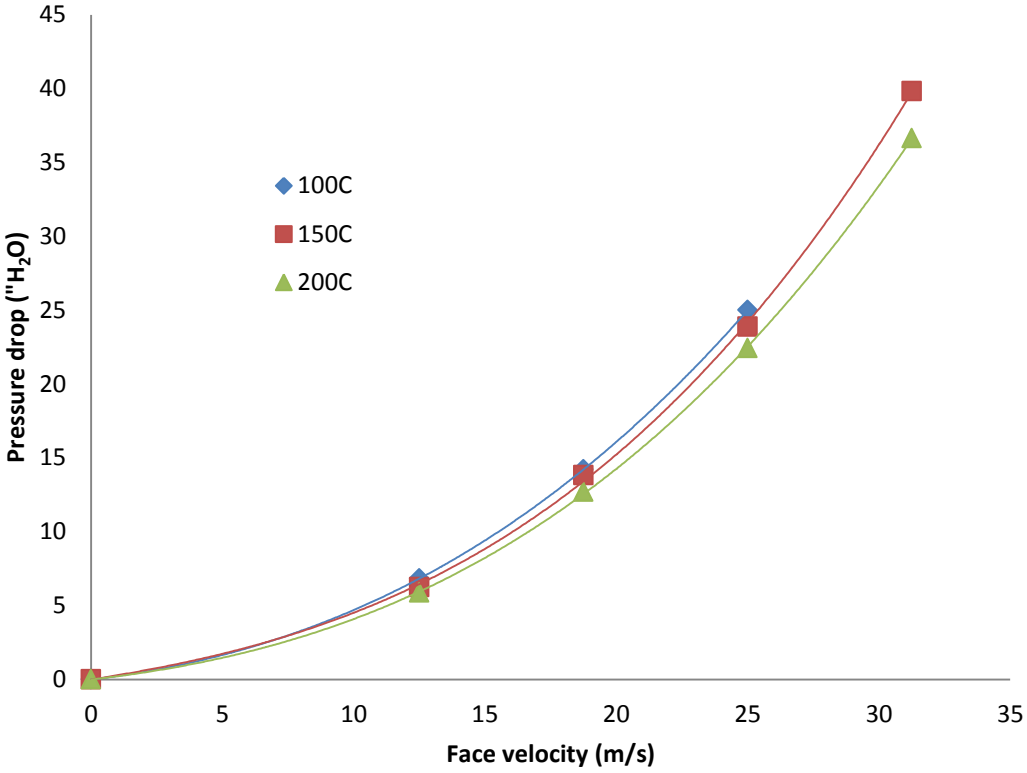

Figure II-41. Pressure drop of microfibrous media with triangle fairings added at three temperatures

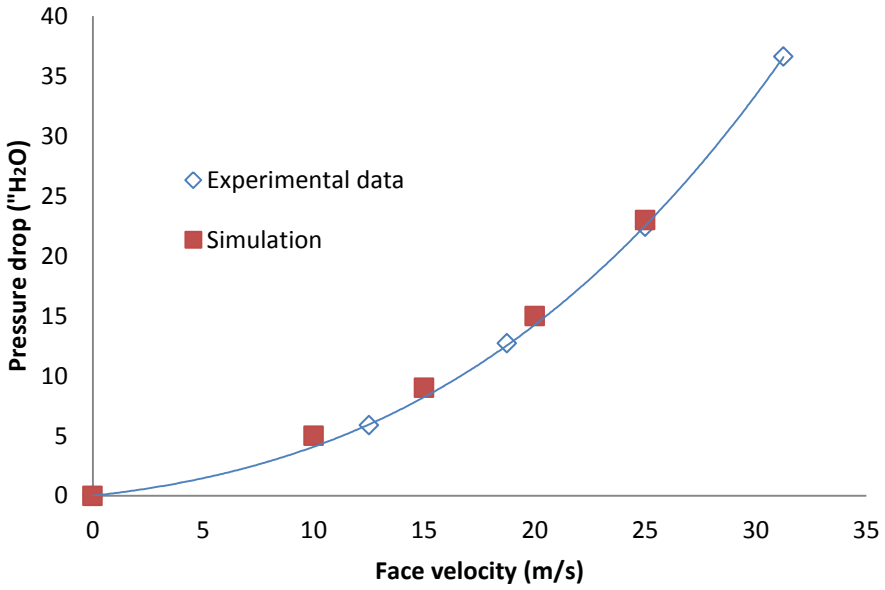

Figure II-42. Pressure drop comparison of experimental data and simulation results; Temperature @ 200℃

Close investigation of the triangle fairings shows great performance in gradual compression of the air and reduction in total pressure drop. However, this is with upstream fairing case only. By similar assumption, triangle fairings should also help if they are added to the downstream to avoid the vortex flow formed by the sudden expansion. As previous simulation showed, the vortex flow mainly exists at the downstream pleat tip area, which is not totally symmetric with the upstream fairings. However, if being added together, the total area and number of fairing is the same. So it is expected that they will perform similarly as adding fairings to the upstream.

Simulation result (Figure II-43) shows that the vortices are completely removed downstream. The velocity profile shows that the flow coming out of each pleat is mixing more gradually to avoid vortex flows. Since flow is less intended for the low pressure vortex area, pressure drop is reduced. By adding triangles at both upstream and downstream, the total pressure drop reduction is maximized. Figure II-44 shows pressure value at stream wise direction for adding fairings at upstream and downstream, which indicates the reduced extreme pressure spots in these areas. Velocity profile (Figure II-45) for this case also shows no apparent flow diversion and vortex, which are all desired flow pattern by adding fairings.

Figure II-46 compares the pressure drop reduction by adding different kinds of fairings to the pleat tip. By adding triangle fairings to the upstream and downstream of the pleat tip, the pressure drop can be reduced up to 15% at 30 m/s and 200 ℃. Considering the energy required to push the air through the filter,

$$\text{Energy} = Q * \Delta P * t \tag{II.12}$$

where Q is volumetric flow rate, ΔP is pressure drop, t is operation time, operating cost for the whole system can be reduced dramatically.

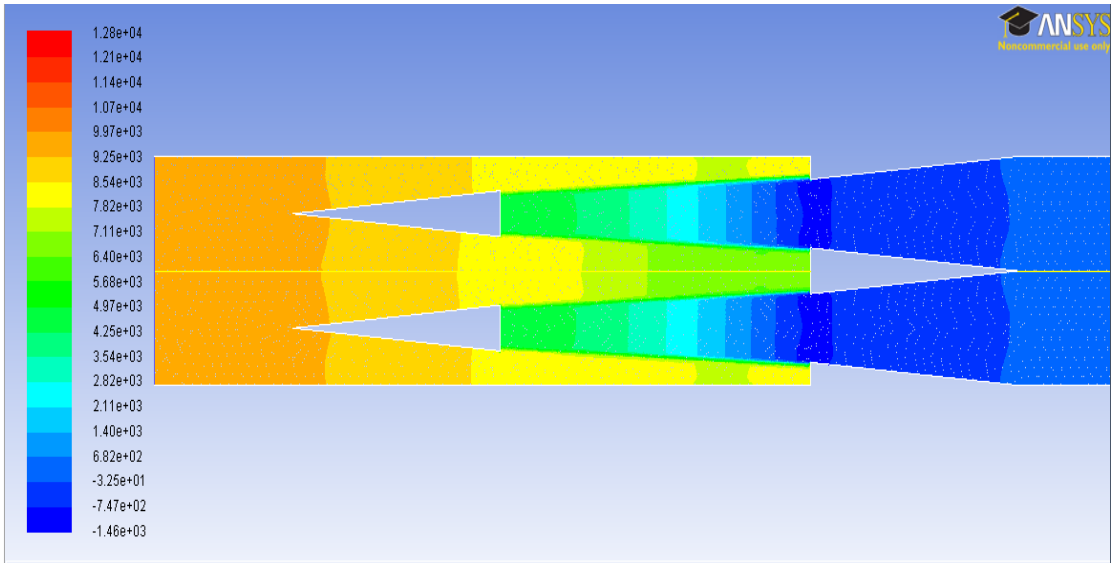

Figure II-43. Pressure drop simulation for pleated microfibrous material filters with triangle fairings at both upstream and downstream; pressure drop changes gradually through the whole area, no extreme pressure spot observed; reduced overall pressure drop with triangle fairings added only to upstream

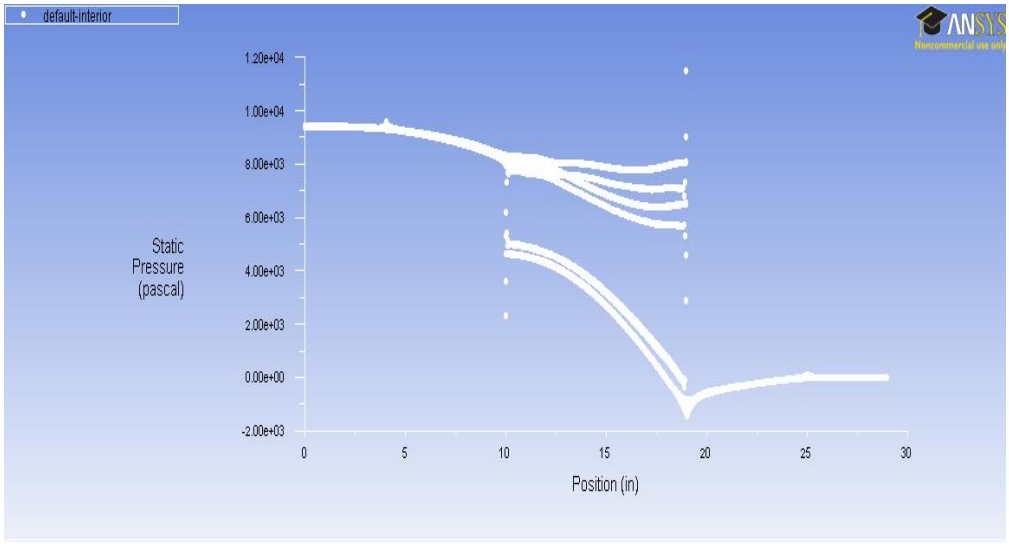

Figure II-44. Pressure value at stream wise direction; downstream bulk pressure @ 1 atm; total pressure drop @$9.2*10^3$ Pa

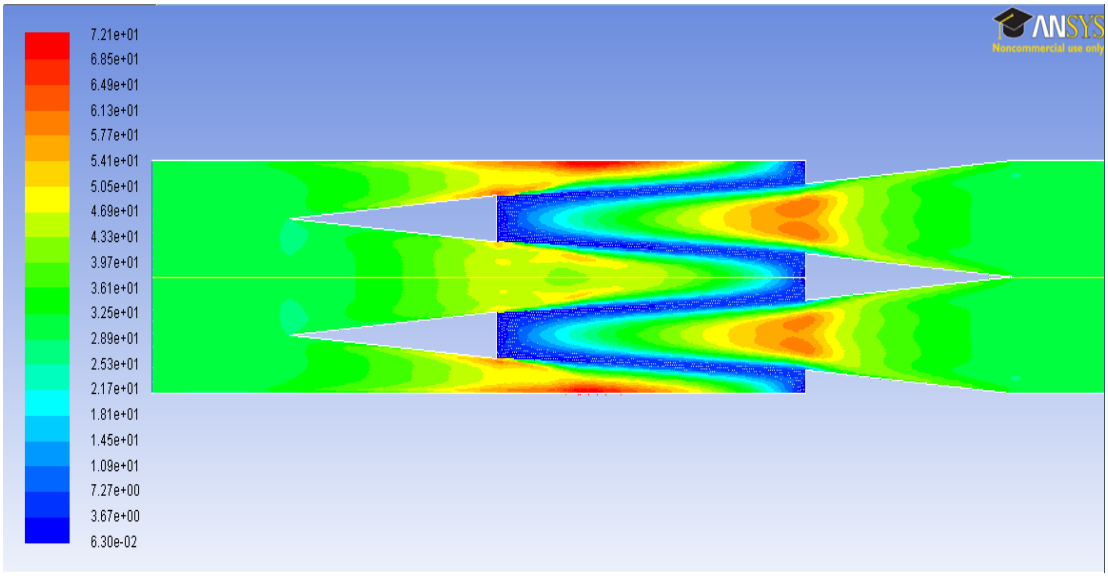

Figure II-45. Velocity profile for pleated microfibrous material filter with triangle fairings added to both upstream and downstream; eddy flow removed by added fairings

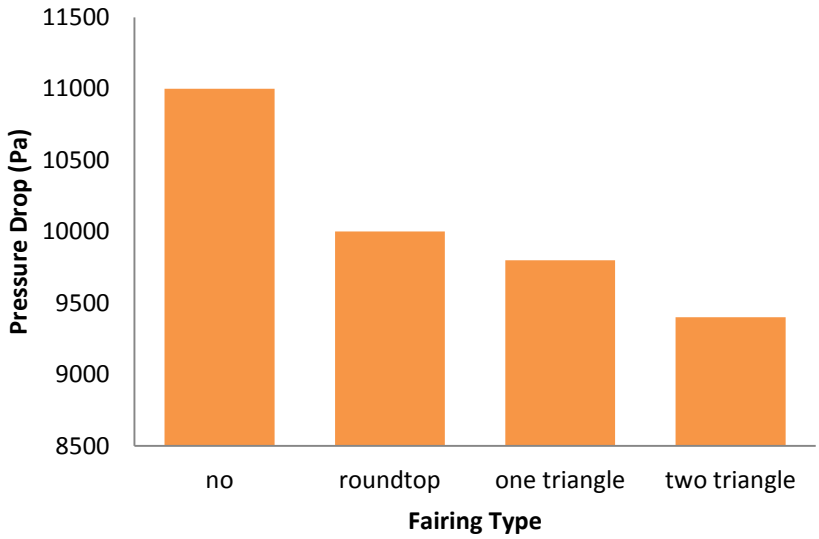

Figure II-46. Comparison pressure drop of adding different kinds and amounts of fairings to pleat tips

Figure II-47 shows a typical U-curve for a pleated air filter. There is an optimum pleat number for each pleat structure depending on the filter media and pleat depth. This number exists because of the switch between the media dominant low pleat number regime and geometric dominant high pleat number regime. Due to the limitation of structure preparation (Max pleat number 4), the optimum pleat number is obtained using simulation. Figure II-48 is simulation using pleated microfibrous media at 30 m/s and 200℃. The optimum pleat number is 4 which is the same as the W structure used in most tests.

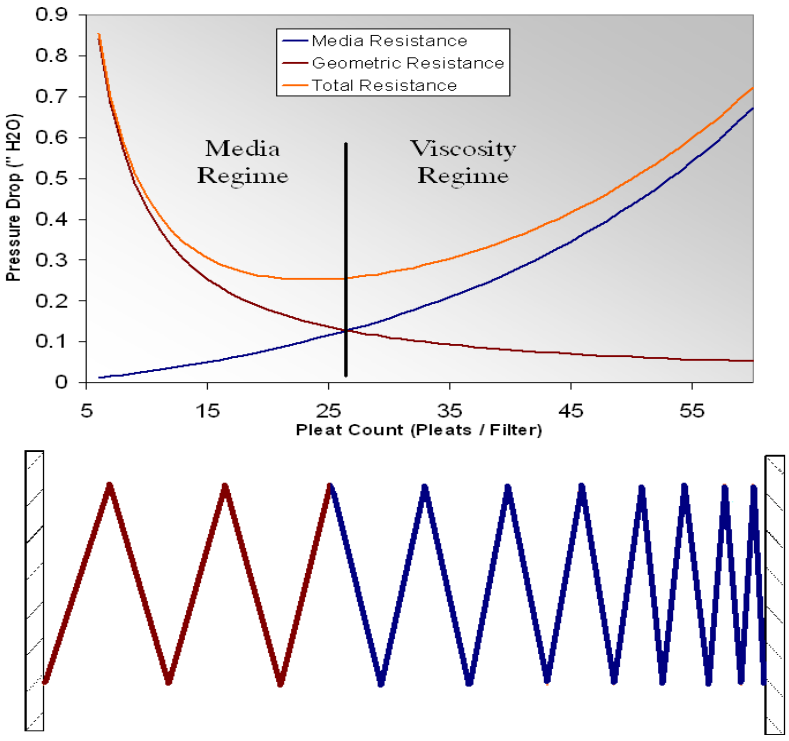

Figure II-47. Pleat number effect on pressure drop

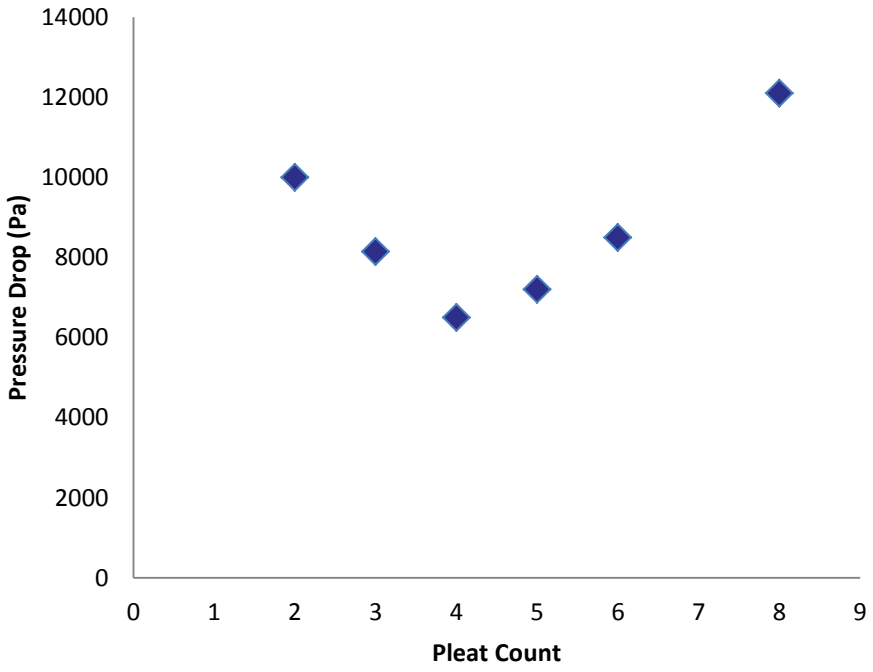

Figure II-48. U curve by simulation; optimum pleat number at 4

II.8 Summary

A pressure drop model for pleated microfibrous media has been established by considering the micro scale structure of the material. SEM images for top and side of microfibrous media were obtained to sketch the structure of the simulation. Pressure drops were modeled for fiber material only and fiber with entrapped particle cases, which showed the significant contribution to the pressure drop by the entrapped particles. To

best approximate the real case scenario, shape factor effect of the entrapped particles was also investigated. The simulation result was consistent with theoretical models about the shape factor: lower shape factor leads to a larger pressure drop. Due to the malleable nature of the metal fibers, they can be temporarily compressed when running at high pressure drop cases. This effect contributes to higher volume loading of both the fiber and particles. Simulation process also took this into consideration by measuring media thickness at different pressures and adjusting the simulation correspondingly. Flat media pressure drop was accurately simulated taking into consideration the shape factor and compressibility.

Pleat structure pressure drop of the microfibrous media was simulated based on the simulation of flat media. Fairings added to reduce pressure drop were investigated, which showed triangle fairings help with gradual compression of the air and the total pressure drop. Optimum pleat number was also obtained based on simulation results.

References

[1] Devarakonda Angirasa, Forced convective heat transfer in metallic fibrous materials, Journal of Heat Transfer, August 2002, Vol. 124 739-745

[2] Donald R. Cahela, Bruce J. Tatarchuk, Permeability of sintered microfibrous composites for heterogeneous catalysis and other chemical processing opportunities, Catalysis Today 69 (2001) 33-39

[3] B. Dhandapani, S.T. Oyama, Gas phase ozone decomposition catalyst, Applied Catalysis B: Enviromental 11 (1997) 120-166

[4] Daniel K. Harris, Donald R. Cahela, Bruce J. Tatarchuk, Wet layup and sintering of metal-containing microfibrous composites for chemical processing opportunities, Composites: Part A 32 (2001) 1117-1126

[5] Reghan J. Hill, Donald L. Koch, The transition from steady to weakly turbulent flow in a close-packed ordered array of spheres, Journal of Fluid Mechanics (2002), vol. 465, pp 59-97

[6] Ranjeeth R. Kalluri, Donald R. Cahela, Bruce J. Tatarchuk, Comparative heterogeneous contacting efficiency in fixed bed reactor: Opportunities for new microstructured systems, Applied Catalysis B: Environmental 90 (2009) 507-515

[7] R. R. Kalluri, R. K. Duggirala, D. R. Cahela, C. J. Roy, and B. J. Tatarchuk, CFD analysis of mass transfer enhancement due to inert structures present in fluid flow paths in heterogeneous contacting systems, manuscript submitted to computers and chemical engineering, June 2008

[8] Takashi Kameya, Kohei Urano, Catalytic Decomposition of ozone gas by a Pd impregnated MnO_2 catalyst, Journal of environmental engineering 10.1061/(ASCE)0733-9372(2002)128:3(286)

[9] Amogh N. Karwa, Bruce J. Tatarchuk, Pressure drop and aerosol filtration efficiency of microfibrous entrapped catalyst and sorbent media: Semi-empirical models, Separation and Purification Technology 86 (2012) 55-63

[10] Rivers, D.R., D.J. Murphy, Air filter performance under variable air volume conditions, ASHRAE Transactions 106(2): [3]-44 2000

[11] Ryan A. Sothen, Bruce J. Tatarchuk, A semi-empirical pressure drop model: part I-pleated filters, HVAC&R Research, Vol.14, Number 6

[12] Vafai, K., Tedn, C. L., Boundary and inertia effect on flow and heat transfer in porous media, International J. Heat Mass Transfer. Pp1183-1190, 1982

[13] Xingpeng Wang, Kitai Kim, Changhwan Lee, and Jooyong Kim, Prediction of air filter efficiency and pressure drop in air filtration media using a stochastic simulation, Fiber and Polymers, Vol. 9, No. 1, 34-38

Chapter III. Ozone Removal at Short Contact Time using a New High Contact Efficiency Microstructured System

III.1. Abstract

Microfibrous Entrapped Catalysts (MFEC) manufactured from 8 μm diameter nickel fibers are engineered into a pleated heterogeneous catalytic reactor to compare the removal performance from conventional packed bed and monolith reactors at high mass flow condition, since MFEC can entrap small particles (150-200 μm) which significantly improves inter-phase mass transfer rate. Optimized pleated MFEC reactors can be operated at short contact time (~100 μs) while maintaining high catalytic performance and offering low pressure drops. This unique reactor is targeted toward ozone in this research. MFEC is investigated under turbine bleed air conditions of high temperature (100-200 ºC) and high face velocity (10-30 m/s) resulting in an inter-layer contact time of 67-200 μsec. Noble metal (Pd) and transition metal (Mn) catalysts are impregnated onto entrapped particles (e.g. γ-Al2O3, slilica) using incipient wetness method. Results show that a high level of ozone decomposition is achieved with a significant reduction of catalyst consumption compared with monolith reactors. External mass transfer rate and effective reaction rate are analyzed and compared with packed bed and monolith rectors. Compared with packed bed and monolith, MFEC demonstrates good gas-solid mass transfer rate, while offering small pressure drop. Besides, several aspects including humidity, system pressure and catalyst deactivation have been investigated for their effects on reactor performance.

Keywords: Ozone, Microfibrous Entrapped Catalyst, High Mass Flow, Heterogeneous Catalysis

III.2. Introduction

III.2.1. Background

In a series of high mass flow rate catalytic applications like aircraft cabin air filter, power plant filters and automobile catalytic converts, a reactor structure with high gas-solid mass transfer rate and low pressure drop is demanded to provide high quality breathing air. Conventional fixed bed reactors, including packed bed and monolith, are adapted to be used in these operating conditions. However, reactor performance is limited because of intrinsic properties of both beds. Packed bed offers good gas-solid mass transfer rate, while causing unacceptably high pressure drop. Monolith structure reduces pressure drop at high mass flow rate, while demonstrating very low gas-solid mass transfer rate. Meanwhile, both beds show poor heat management for highly exothermic reactions, because they are usually made of low heat conductivity metal oxide materials like alumina and silica. Bad heat management causes reduced catalytic performance and shorter catalyst life.

MFEC is a new structure of matter that offers both good gas-solid mass transfer and small pressure drop. However, changing the reactor type from packed bed or monolith to MFEC also presents challenges from other aspects. The dimension difference between these reactors is large. MFEC is usually only millimeters in thickness, while the monolith is usually more than 100 times thicker. This thickness difference has resulted in

a much shorter reactant contact time for MFEC. To maintain a similar or even better catalytic performance, MFEC has to entrap the smallest particles possible to provide larger surface area to improve the contact efficiency. Because of their larger surface area, the smaller particles also have the benefit of less catalyst consumption. However, a larger pressure drop across the reactor is usually expected as a penalty by using smaller particles. Large pressure drop does not exist in MFEC applications, since MFEC is a high voidage material (>70% void). MFEC material structure resembles a frozen fluidized bed. Therefore, the total pressure drop benefits from the high voidage and is not significantly affected by the smaller particles. Besides, this non-woven material can be pleated to further decrease the pressure drop across reactors and increase catalyst loading. For a specific application requirement, fiber diameter, particle size and pleat number can be considered simultaneously for optimum design, which provides MFEC material with flexibility over conventional monolith reactors. The weight and volume of MFEC is usually less compared with monolith reactor, which are crucial factors for a compact system such as a commercial aircraft, where more space for other on-board equipment is made available.

III.2.2. Microfibrous Entrapped Catalysts (MFEC)

MFEC is a high contact efficiency composite material prepared using high speed and low cost wetlay paper-making equipment and techniques [1-2]. In the preparation process, micrometer diameter metal, polymer or ceramic fibers are slurried into an aqueous suspension with cellulose fibers and other selected particulates and/or fibers. The resulting mixture is then cast into a preform sheet using a wetlay process and dried to

create a sheet or roll of preform material. Subsequent sintering of the preform at elevated temperatures (ca. 1000ºC) removes the cellulosic binder and entraps the selected particulates/fibers within a sinter-locked network of fibers. The effective channel size in these materials can be designed almost independently from the particle diameter, since channel size also depends on voidage and the mixture of fiber diameters chosen to design the MFEC. This allows small particles with high surface to volume ratios to be entrapped in a very open material. SEM images of the material are shown in Figure III-1. Figure 1(a) shows 8 μm nickel fibers. Figure III-1(b) shows 8 μm nickel fibers entrapped with 150-250 μ m alumina particles. Investigations have been performed to fundamentally understand this new material. Yang et al. [3-4] have studied the external mass transfer effect in the desulfurization process and showed improved performance by MFEC over packed bed. Dhage et al. [5] have studied ZnO/SiO_2 adsorbent in gas phase desulfurization and showed the improved performance over packed bed. Sheng et al. [6] have studied the heat transfer property of MFEC at low mass flow rates and showed the improved performance in Fischer−Tropsch synthesis process. Zhu et al. [7] have studied the electrical conductivity of the metal MFEC sheet in fuel cell. Moreover, MFEC has been studied in by Sothen et al. [8-9] to demonstrate its improved performance in removal of airborne particles using pleated MFEC material.

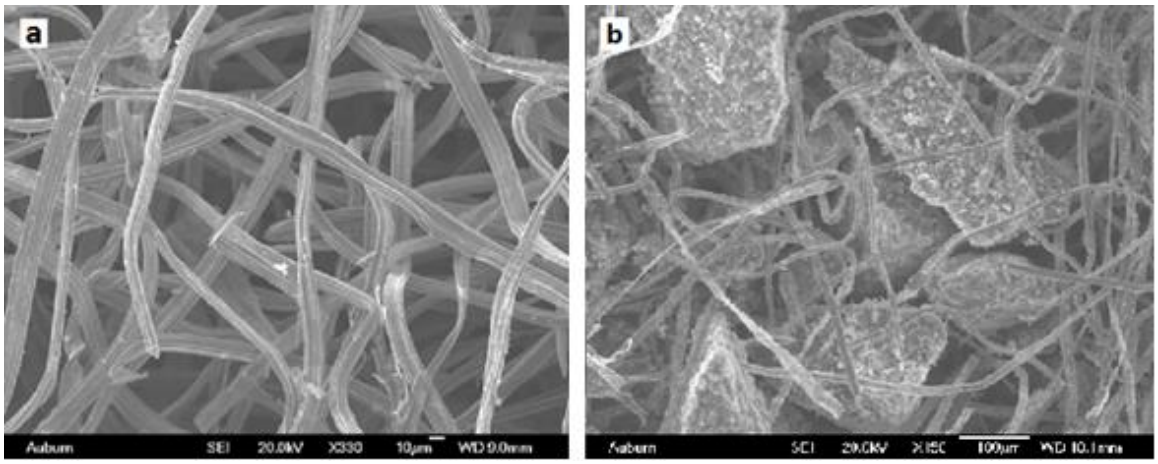

Figure III-1. SEM image of microfibrous material: (a) 8 μm nickel fiber, (b) 8 μm nickel fiber entrapped with 150-250 μm alumina particles

III.2.3. Catalytic ozone decomposition and aircraft cabin air treatment

Photochemical conversion of oxygen creates ozone in the atmosphere [10]. Ozone is usually found in the earth's upper atmosphere [11-12] (10~30 miles above the earth's surface). The concentration increases with latitude and changes with seasons and weather. Ozone concentration up to 6 ppm can be found in the atmosphere. Ozone is also created by common equipment, including copiers, pool cleaners, and water purification processes. The Environmental Protection Agency (EPA) sets ozone exposure limits as 0.08 ppm for 8 h and 0.12 ppm for 1h. Long exposure to ozone will cause a series of health problems, including coughing, throat irritation and chest discomfort. Several methods, including catalytic decomposition, thermal decomposition and adsorption, are available to treat ozone in various situations. In high flow rate applications, the quantity of adsorbent required is excessive because of the large demand for clean air. The thermal

decomposition method usually requires a higher temperature and higher pressure environment. Compared with thermal decomposition and adsorption, catalytic decomposition operates at lower temperatures without large consumptions of adsorbent. This research will study the catalytic removal of ozone using MFEC and demonstrate the advantage of MFEC material over conventional packed bed and monolith reactors in terms of improved gas-solid mass transfer rate, reduced pressure drop across reactor and lower catalyst consumption.

III.3. Material and Methods

III.3.1. High Volumetric Test Set Up

Figure III-2(a) shows the schematic of the test system. The high velocity test set up includes a 40 horse power blower (Fan Equipment Company Inc.) circulating air inside a closed loop system. A variable drive is used to control the system speed ranging from 10-40 m/s. The system is running at near atmospheric pressure. Ozone is introduced at the outlet of the blower and is monitored upstream and downstream of the reactor using two Eco Sensor UV100 ozone sensors. Pressure drop across the reactor is monitored using IDP10-T differential pressure transmitters. System speed is acquired by calculating the pressure drop across a bare section on the rig and verified by a Dwyer® 1/8" stainless steel pitot tube at different temperatures. System temperature, which changes continuously from 100-200℃, is controlled by balancing several energy sources. Figure III-2(b) shows the schematic of heat balance of the system. Heat sources of the

system include ring heater on the blower plate, skin friction generated heat and exothermic reaction released heat. The reactor is constructed using pleated structure (Figure III-3) with metal wire mesh to enhance the mechanical strength of the MFEC.

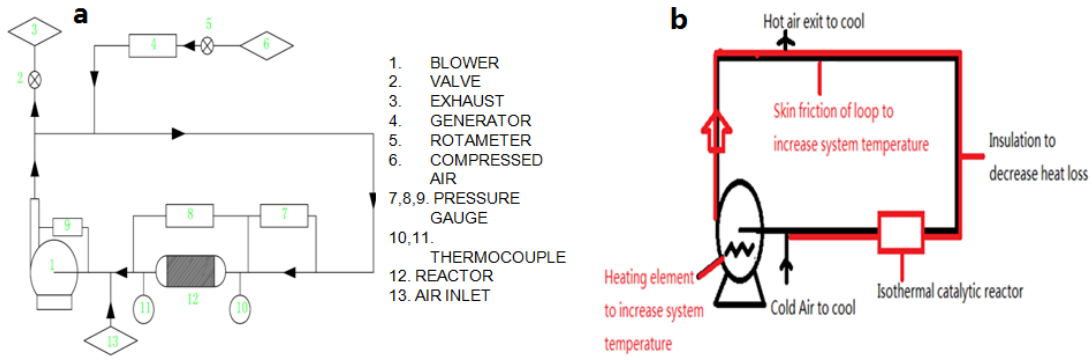

Figure III-2. Sketch of high face velocity test setup: (a) Schematic of test set up (b) Heat balance of the system, heat source in red, cooling source in black

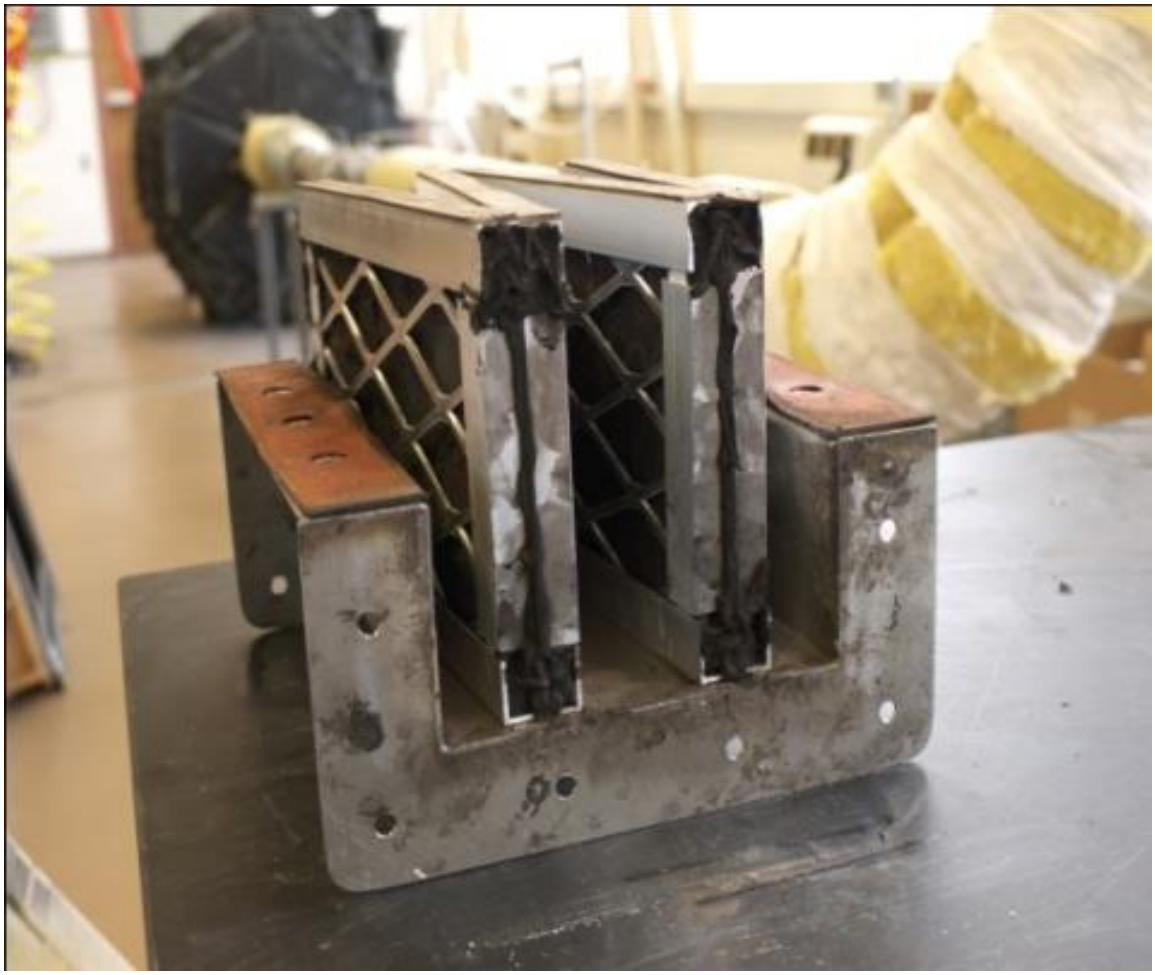

Figure III-3. Pleated structure installed in the reactor for ozone decomposition tests (4 pleats)

III.3.2. Pressurized System Test Set Up

The test for a pressurized system is carried out in a small scale set up for easier comparison of catalytic performance. The reaction condition in a single flat sheet of MFEC in a tube reactor is essentially the same as that for a single pleat in the full scale structure in terms of temperature, catalyst structure and face velocity within the bed. Figure III-4 shows the test set up for the pressurized system. In this system, the reactor

tube is confined in an oven to maintain the system temperature. Omega® J type thermocouple is installed downstream of MFEC to test accurate air temperature. System pressure is controlled by varying the supplied air pressure. Cole-Parmer® pressure gauge WU-68920-38 is used to monitor system pressure downstream of the MFEC. Ozone level is monitored by two Eco Sensor® UV-100 ozone meters upstream and downstream. Rotameter is used to control the system face velocity. While this smaller test set up can maintain high temperature and identical ozone level, this system cannot hold any pleat structures. Because of this limitation, it can only test a flat MFEC sheet with a reduced face velocity (up to 15 m/s). However, face velocity within each pleat is only 1/n of the system velocity in the pipe (i.e. 1/4 if W structure is used for pleat structure) on a full scale structure. The in-bed face velocities for both pleat structure and flat structure cases are within the same range. Catalytic performance at higher system pressures is compared with lower pressure performance based on the results generated on the same system.

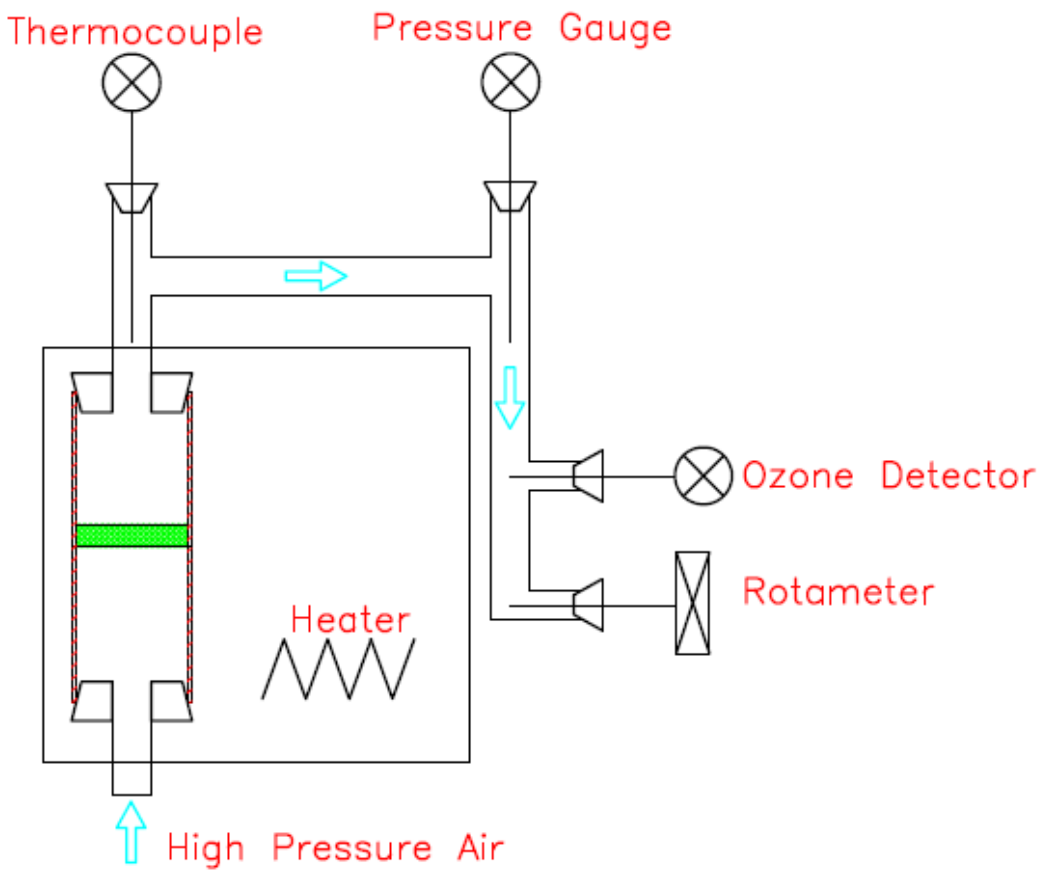

Figure III-4. Schematic of the tubular reactor for evaluation of catalytic performance in the pressurized system

III.3.3. Set Up for Humidity Tests

Humidity plays an important role in catalyst performance, since it can either promote a reaction by providing favorable environment or reduce reaction rate by blocking active catalyst sites. In certain application environments like high altitude ambient air, the humidity level can drop dramatically. Catalytic performance at these environments cannot be predicted based on ground level results. In this research, the effect of humidity on catalytic performance is performed by comparing ozone removal

efficiency at different RH levels. An Omega HX15 high temperature relative humidity probe transmitter is used to monitor humidity levels at different temperatures.

III.3.4. MFEC and Catalyst Preparation

For this study, 8 μm nickel (Ni-200) fibers were acquired from IntraMicron, Inc., AL., and γ-Al_2O_3 was acquired from Alfa Aesar®. In making MFEC sheets, metal fibers were blended with cellulose into a suspension using low speed blending in early stages to avoid chopping of the fibers and high speed in later stage to fully disperse the fibers. The suspension was then transferred into an 8"×8" sheet former. Then Al_2O_3 was added to the suspension with rapid stirring. Water was drained rapidly, minimizing the different precipitation speed of the fibers and supports. The preform sheets were fully dried (24 h). At this stage, added cellulose acts as the binding agent of the fibers. However, these cellulose fibers can affect the mechanical strength of the sheets if not removed properly before sintering. This was done by leaving the dried sheet at 400℃ for 1 h. The dried sheets were then sintered at 1050℃ in a reducing environment (H_2) using BTU-1000 furnace for 40 min. As for catalysts, $Pd(NO_3)_2$, $AgNO_3$ and $Mn(NO_3)_2$ were acquired from Alfa Aesar®. These catalysts were added to MFEC by incipient wetness process. MFEC was soaked in catalyst solution for 30 min and drained of excess water afterwards. Impregnated sheets were dried overnight and calcined at 673 K for 4 h.

III.4. Result and Discussion

III.4.1. Catalytic Decomposition of Ozone using MFEC

Ozone decomposition catalysts have been thoroughly studied over the past decades [13-17], since ozone is widely used as a disinfectant. Decomposition catalyst is required in various situations to protect individuals as ozone is harmful to the human respiratory system. Dhandapani et al. [17] reviewed noble and transition catalysts for ozone decomposition at low temperature. Both theses catalysts show catalytic activity in ozone decomposition at different temperature regions. Among the transition metal catalysts, MnO_2 has the highest activity for low temperature applications (<50℃). Many low temperature applications use MnO_2 as the active catalyst. However, for higher temperature commercial ozone scrubbers, Pd based catalysts are widely used. These catalysts are generally more resistant to poisoning in certain applications and most importantly have better aging performance.

Figure III-5 shows the Pd/Al_2O_3 catalyst tested at three temperatures. As observed in the figure, the catalytic performance had a linearly reducing relationship with increasing face velocities. Even though convective heat and mass transfer at these velocities increase with increasing face velocities, the catalytic performance was not affected by these factors, leaving contact time as the crucial factor that determined the performance of the these catalysts. At these velocities, the Reynolds number within the test rig is in the turbulent flow region ($\sim 10^6$). However, considering the small characteristic dimension of the entrapped particles, the Reynolds number within the

MFEC is much smaller (~10^2). Hill et al. [18] studied the flow type for the beds made of similar size particles and found the flow to be weakly turbulent in this range. Since there is no flow type transition from inlet to the inner part of the media, face velocity is regarded as the only factor affecting the reaction. This is verified by other test results by using different catalyst materials, including Ag, Mn and bi-metal catalysts. The results are shown in Table III-1. For every catalyst tested, all showed the same linear relationship as Pd catalyst. The only difference is their temperature sensitivity. Mn based catalysts are widely used as low temperature ozone decomposition catalysts since they are known to have smaller activation energies. Therefore, Mn based catalysts showed better performance at lower temperatures; Pd catalyst activity dropped dramatically when running under 150℃. In all these tests, thermal decomposition of the ozone by itself is not considered since the temperature is not high enough. An experiment was carried out to verify this assumption. MFEC reactor was replaced with a bare rig. No ozone concentration change was observed when running tests at same conditions.

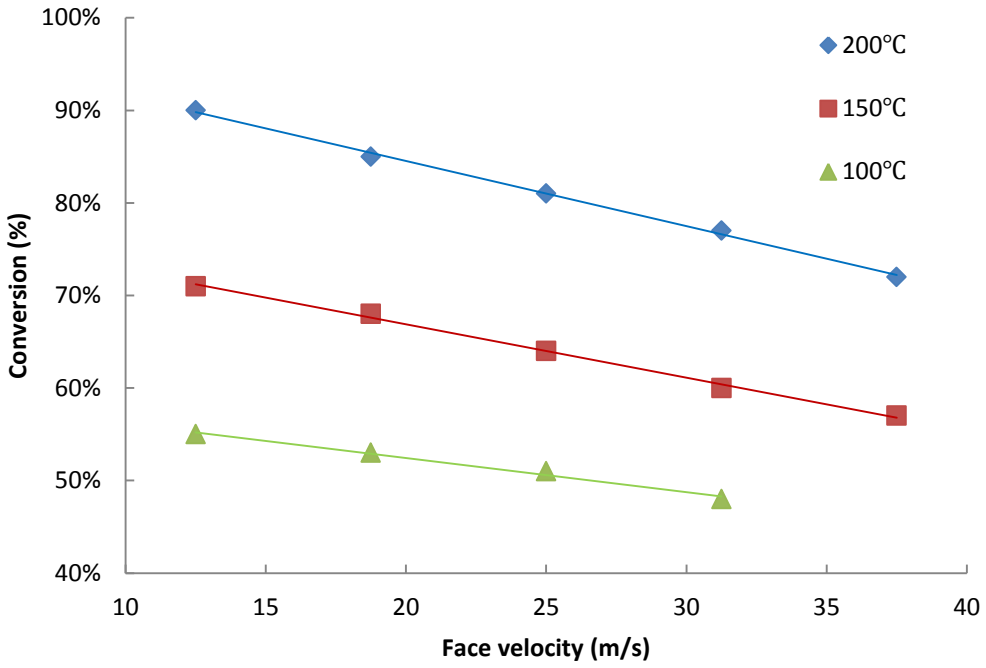

Figure III-5. Pd-based catalysts for ozone decomposition at high temperatures and high face velocities

Table III-1. Catalyst performance for ozone decomposition at different temperatures and velocities

Catalysts	Velocity (m/s)	Conversion		
		200 ℃	150 ℃	100 ℃
1% Pd/SiO_2	12.50	89%	68%	53%
	18.75	85%	64%	49%
	25.00	81%	59%	45%
	31.25	80%	54%	N/A
1% Ag/Al_2O_3	12.50	90%	81%	68%

	18.75	89%	74%	59%
	25.00	84%	68%	55%
	31.25	81%	61%	N/A
10% MnO_2/Al_2O_3	12.50	92%	90%	89%
	18.75	89%	88%	84%
	25.00	85%	82%	79%
	31.25	80%	78%	N/A
1% Pd-10% MnO_2	12.50	100%	95%	92%
	18.75	96%	90%	82%
	25.00	94%	84%	75%
	31.25	88%	81%	N/A

As mentioned earlier, the flow type within the MFEC is weakly turbulent; the flow type is therefore assumed to be turbulent. This assumption was verified in a separate paper, which numerically solved the Navier-Stoke equation within the MFEC. Results showed the flow type is plug flow with a very thin boundary layer accounting for less than 1% of the cross section of the reactor. Kameya et al. [16] studied the gas phase ozone decomposition over Pd catalyst and found it was under first order reaction. In this study, reaction constants for different catalysts were acquired by experiment results at $100 \pm 2℃$, $150 \pm 2℃$, $200 \pm 2℃$ using Arrhenius equation,

$$\ln(\mathrm{k}) = \frac{-E_a}{R}\frac{1}{T} + ln(A) \qquad \text{(III.1)}$$

in which A is frequency factor (s^{-1}), R is gas constant (J mol^{-1} K^{-1}). The relationship between 1/T and ln(k) is linear. Summary of the catalysts tested is shown in Table III-2. Turn over frequency for each catalyst is calculated using H_2 chemisorption results.

Table III-2. Ozone decomposition reaction kinetics analysis using Arrhenius equation

Catalysts	Rate constant k (s^{-1})			E_a (kJ mol^{-1})	TOF (10^{-2} s^{-1})
	100℃	150℃	200℃		
1% Pd/AlO_3	885	1640	4530	23.6	5.12
1% Pd/SiO_2	574	1463	4403	29.7	5.08
1% Ag/Al_2O_3	1921	3001	4527	12.5	3.37
10% MnO_2/Al_2O_3	3801	4304	4710	3.2	N/D
1% Pd-10% MnO_2	4144	5313	8302	10.0	N/D

Heck et al. [11] reported that ozone decomposition under 150℃ is limited by reaction kinetics and reaction is generally limited by bulk mass transfer rate above 150℃. Since the application temperatrue in this research is generally over 150℃, but the contact time for the reaction is fairly short, a few analyses have been performed to confirm the reaction limitation process in ozone decomposition at high volumetric flows. The Weisz-Prater Criterion is used to estimate the influence of pore diffusion on reaction rates. Thiele modulus and catalyst effectiveness factors are calculated based on the following equations.

$$\phi = \left(\frac{\varphi_p d_p}{6}\sqrt{\frac{k_r \rho_c x_c}{D_e}}\right) \quad \text{(III.2)}$$

$$\eta = \frac{1}{\phi}(\coth(3\phi) - \frac{1}{3\phi}) \quad \text{(III.3)}$$

The Weisz-Prater criterion proved that the pore diffusion limitation in this reaction is negligible, while the Mears' criterion demonstrated that the external mass transfer rate limited the reaction. To further verify these analysis results, a comparative experiment has been conducted to show the effect of the external and internal mass transfer limitations. Two kinds of aluminum support were obtained from Alfa Aesar with different pore volume and total surface area (Table III-3). These two supports are ground down to same particle sizes to provide identical external surface areas. Ozone decomposition for both catalysts was run at the same operating conditions (Temperature, Pressure, and Housing Structure). Figure III-6 shows the results for both catalyst supports run at 150℃ and 200℃. Even though the internal surface area differs for both catalyst supports, the results showed no difference in conversion rate. Previous analysis demonstrated that pore diffusion is not the rate limiting process, while the external mass transfer is. This result was consistent with the previous finding by showing particles with same external area and different internal structure have the same catalytic performance.

Table III-3. Two kinds of aluminum supports used for external mass transfer effect test

Support type	Pore volume	Surface area	Particle size
Catalyst support 1	0.62 cc g^{-1}	220 m^2 g^{-1}	150~250 μm
Catalyst support 2	1.14 cc g^{-1}	255 m^2 g^{-1}	150~250 μm

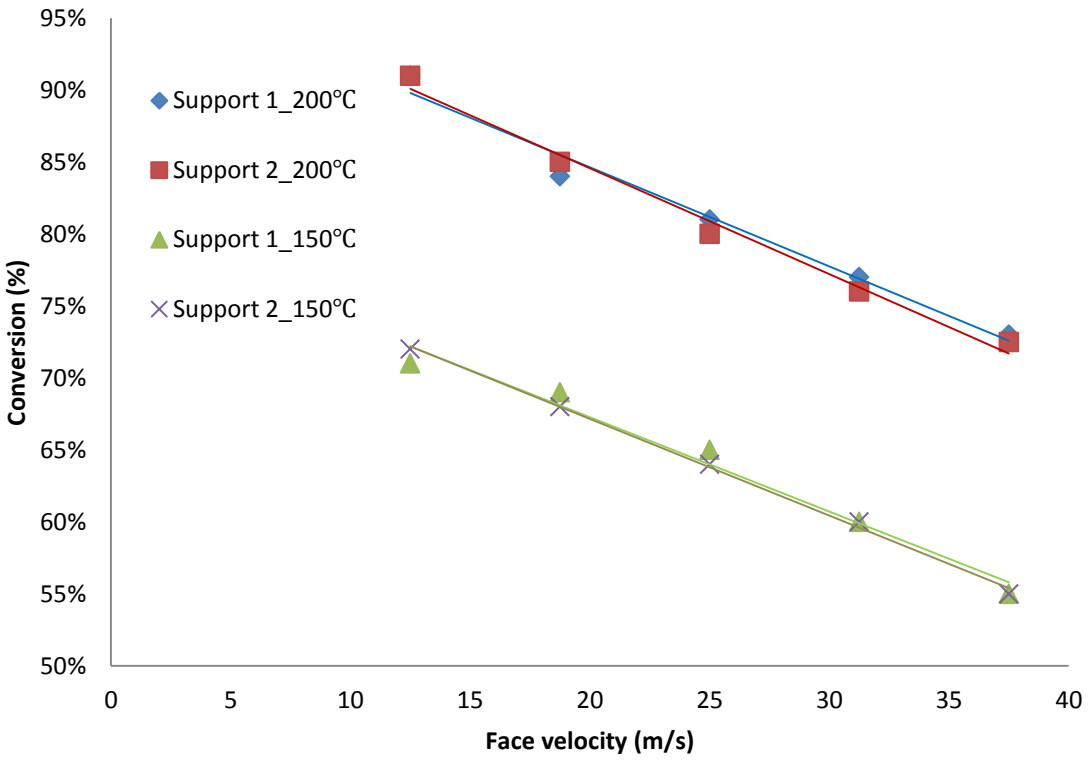

Figure III-6. Effect of catalyst support structure on ozone decomposition

III.4.2. Humidity Effect on Catalytic Performance

Water is known to be easily adsorbed on mineral oxide surface in large amount. Goodman, Al-Abadleh and Grassian et al. [19-21] showed that water adsorbs on Al_2O_3 surface in significant amounts. Kameya et al. [16] have studied humidity effect on Pd and MnO_x catalysts for low temperatures and high RHs and have shown noticeable catalytic performance change. In addition, we have noticed some performance differences between samples that have been dried before tests and those that have not. Thus, it is reasonable to assume that catalytic performance of these catalysts will change if the RH changes in different applications.

Humidity effect on the previous tested catalyst was evaluated at 150℃ and 200℃. RH level is controlled by passing system inlet air through desiccant. RH level in both conditions at two temperatures is listed in Table III-4. All test conditions were kept the same as catalyst screening process to guarantee fair comparison.

Table III-4. Humidity level at two temperatures for comparative tests

Temperature	Without the desiccant	With the desiccant
200℃	4%	15%
150℃	<1%	2%

Figure III-7 shows the Pd based catalyst performance for fresh calcined samples and samples that were exposed to air for a month. As expected, the exposed samples showed less activity than the fresh calcined sample, assuming water molecules blocked the active sites. The same exposed sample was dried again overnight and repeated the same test. The third line in Figure III-7 shows that the catalytic performance almost recovered to that of the fresh samples, which proved the previous assumption. Moreover, catalytic performance evaluation by controlling the system humidity was also carried out. Figure III-8 shows the results of humidity effect at two temperatures. At both temperatures, low humidity levels clearly gave higher conversion of ozone, since more active sites are available at lower humidity levels.

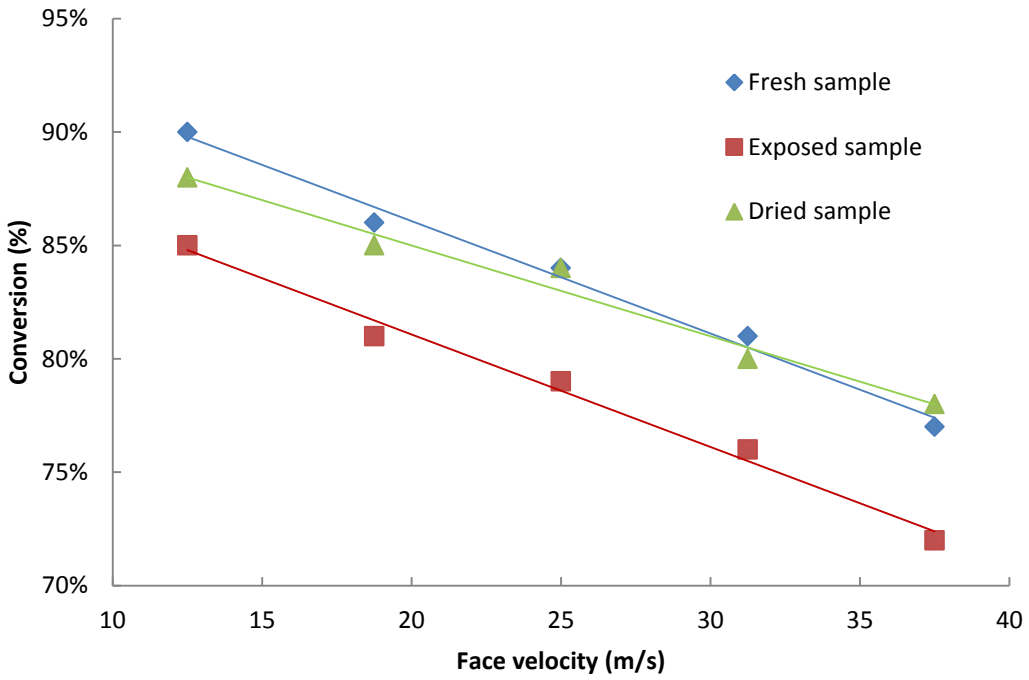

Figure III-7. Ozone decomposition for fresh, exposed and dried samples

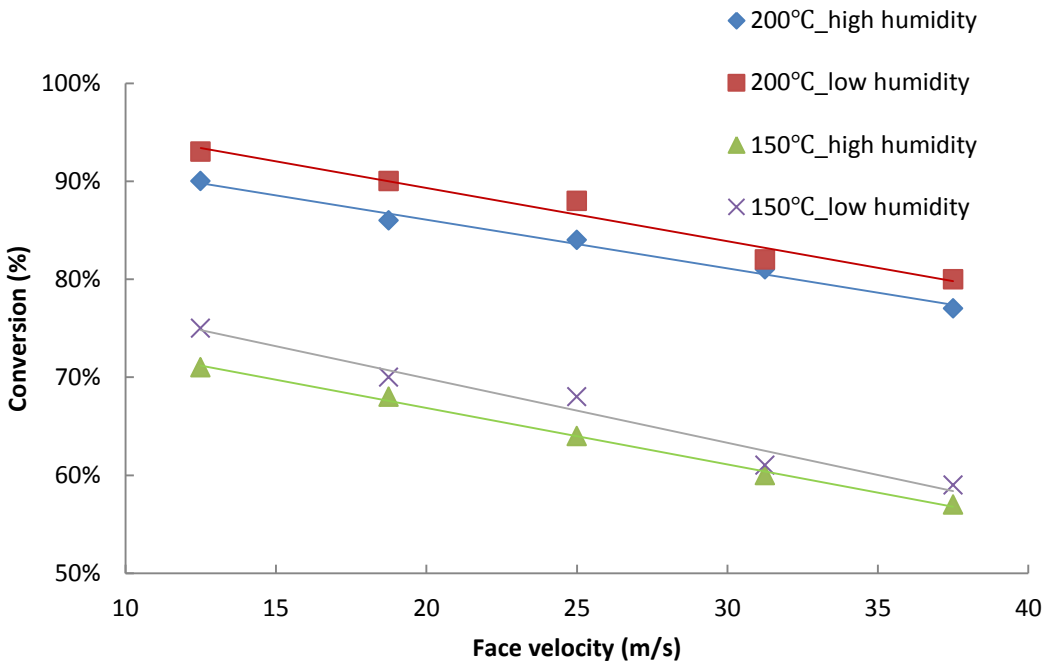

Figure III-8. Catalytic performance of Pd catalyst at different humidity levels when operating at two temperatures

III.4.3. Effect of System Pressure on Catalytic Performance

Real world high mass flow applications usually involve using the bleed air of turbo engines. Bleed air usually contains not only high flow rate and high temperature, but also high pressures. Since system pressures affect mass and heat transfer inside the reactor, the effect must be evaluated as an important factor that may affect catalyst activity.

In order to compare performance of catalysts at different system pressures, two major quantities, volumetric mass transfer coefficient and effective reaction rate, are used

to evaluate performances at different conditions. The volumetric mass transfer coefficient was calculated from Sherwood number,

$$Sh = k_m \varphi_p d_p / D_M \quad \text{(III.4)}$$

To estimate Sherwood number used in this calculation, Dwivedi and Upadhyay's method [22] for gas-solid system in fixed bed is used, which can be expressed as

$$Sh = \frac{0.455}{\varepsilon_b} \left(\frac{Re_p}{PF}\right)^{0.59} Sc^{0.33} \quad \text{(III.5)}$$

This correlation is good for voidage ranging from 0.25 to 0.97 and Re_p from 1 to 10000, which covered the conditions used in this research.

Kalluri et al. [10] developed the relationship between effective reaction rate and mass transfer coefficient for first order reactions using MFEC material by assuming gas-solid mass transfer rate equals to the reaction rate inside the catalyst. The correlation used for calculating effective reaction rate is

$$\frac{1}{k_{eff}} = \frac{1}{k_m a_c} + \frac{1}{\eta k_r \rho_c} \quad \text{(III.6)}$$

The third term in Equation 6 was determined experimentally. Due to the pressure limitation on the full scale set up, a tubular reactor was used to determine the reaction rate at different pressures. Figure III-9 shows the volumetric mass transfer rate at different face velocities for packed bed, MFEC and monolith. It was found that mass transfer rate was slightly enhanced by increasing system velocities. However, the catalytic performance did not increase accordingly, because the contact time for the reactant was reduced significantly, which affected the reaction in an inverse way. Also shown in Figure III-9, the gas-solid transfer rate has been enhanced by running tests at

higher system pressures. The reaction was analyzed to be limited by the gas-solid transfer rate. Therefore, it is expected that reaction rate will benefit from the higher pressures.

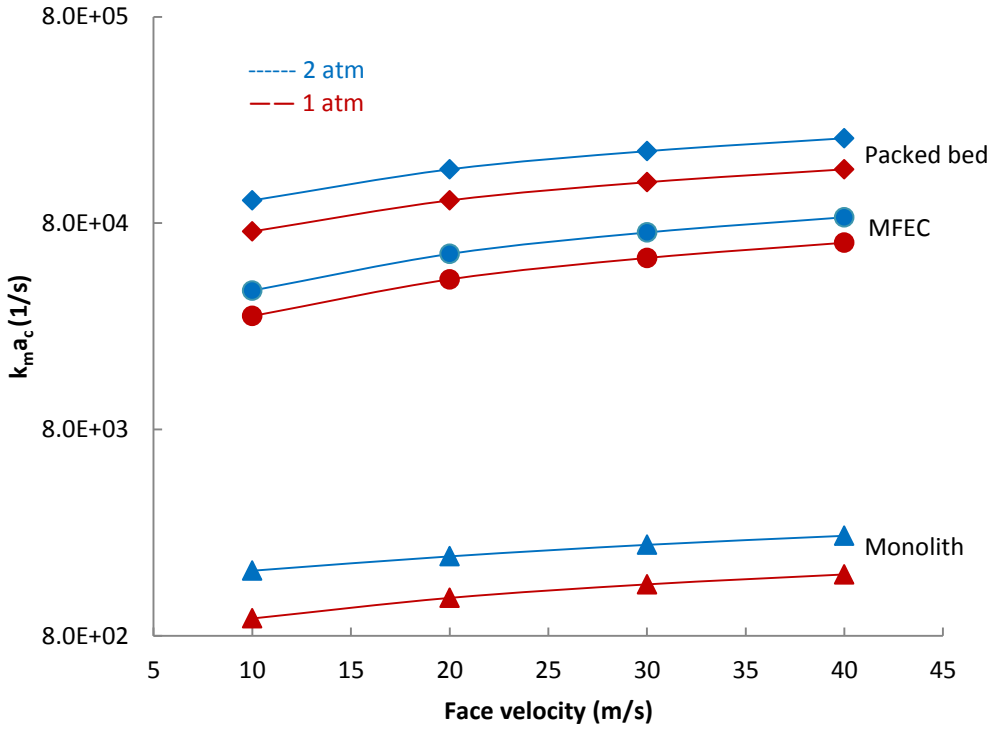

Figure III-9. External mass transfer for packed bed, MFEC and monolith at different system pressures

The effective reaction rate is a measure of the catalyst utilization for the reactor. Since the surface reaction rate is not the rate limiting process, the effective reaction rate showed similar trend as the mass transfer rate. As shown in Figure III-10, the effective reaction rate has been improved by running tests at higher system pressures, indicating better catalyst utilization at these pressures. Though the mass transfer rate and catalyst utilization have been improved by running the system at higher pressures, overall performance of the MFEC at higher pressures cannot be guaranteed, since other

complications, including pressure drop across the reactor, heat management and catalyst aging, must be considered. An overall effectiveness factor was introduced to compare the short term performance between packed bed, monolith and MFEC. Overall performance based on experimentally determined reaction rate, pressure drop and physical property adjustment for all three reactors will be discussed in a separate paper.

$$X = \frac{\ln(C_{Ai}/C_{A0})_{max}}{-\Delta p/\rho v_0^2} \tag{III.7}$$

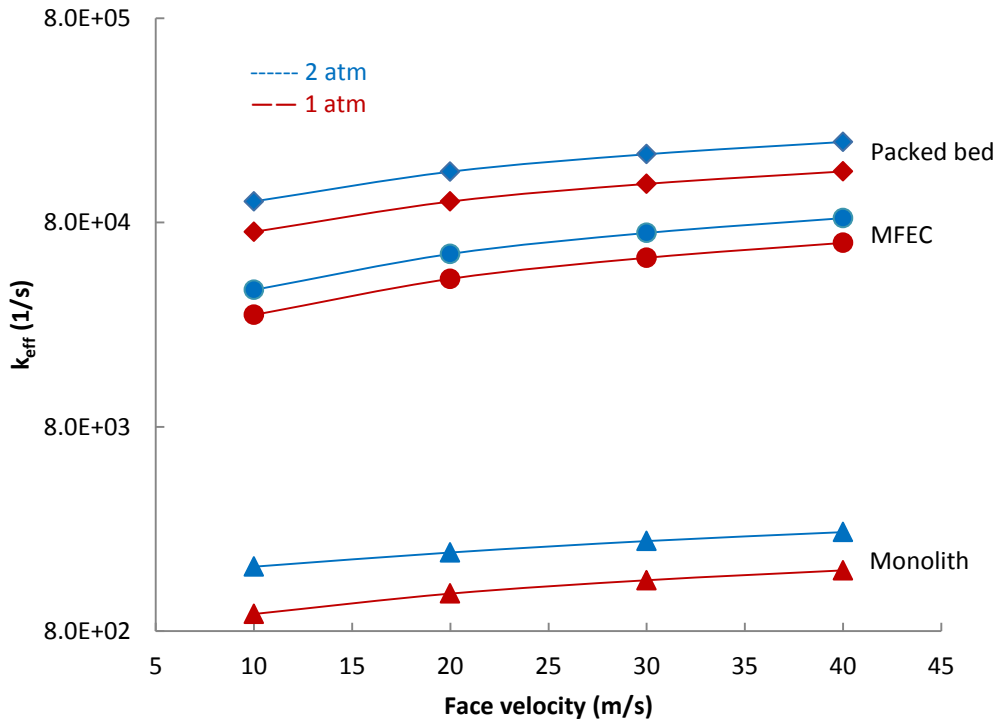

Figure III-10. Effective reaction rates for packed bed, MFEC and monolith at different system pressures

III.4.4. Aging Performance

Ozone reactor aging performance is one of the most significant factors when evaluating the overall performance of the reactor, because ozone concentration is of key importance to the health of on-board passengers in a compact system like a commercial aircraft, especially to airline employees who log far more hours than typical passengers. Heck et al. [11] reported that noble metal catalysts outperform base metal catalysts in airplane applications because of their better aging performance, even though initial conversion rate of most base metal catalysts for ozone is fairly high.

For a high volumetric flow MFEC reactor, aging performance for noble metal catalysts, base metal catalysts and bi-metal catalysts has been investigated. These tests are run at slower speeds with higher ozone concentration. The test conditions are 200℃ temperature, 20 ppm ozone concentration, and 5 m/s face velocity; ultra-high purity air is used to guarantee no other contaminants are introduced into the system. Two standards have been set to regulate the ozone filter minimum efficiency. ASHRAE standard 62.1-2010 has set the design value of maximum ozone level not to exceed 0.107 ppm and a minimum efficiency of 40% for one pass conversion rate. ASHRAE standard 189.1-2009 uses the same efficiency for filter efficiency as ASHRAE standard 62.1-2010, but it used the US EPA non-attainment criterion of 0.075 ppm of maximum ozone level. In this test, the 40% minimum efficiency has been adopted as the evaluation criterion. The results shown in Figure III-11 are for noble metal and transition metal catalyst aging performance. Base metal catalysts had a high initial conversion rate while their activity declined rapidly in aging tests. Nobel metal catalysts maintained their aging performance

relatively better. The bi-metal catalyst demonstrated an overall better aging than both of the Pd and Mn based catalysts.

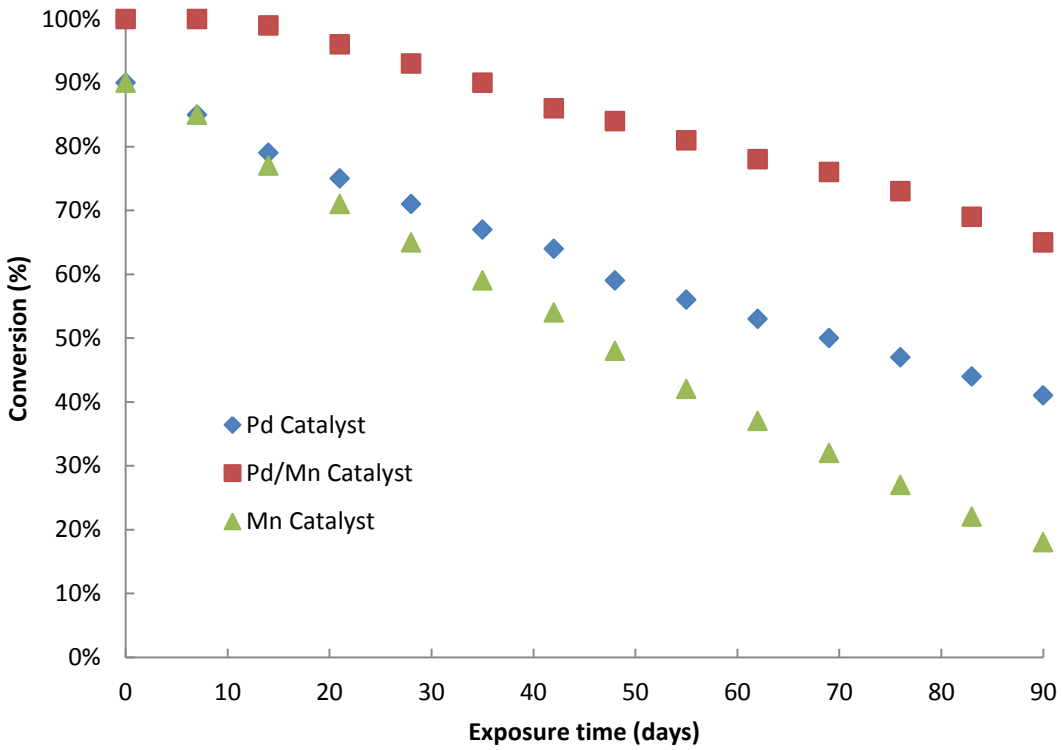

Figure III-11. Pd and Mn based catalysts aging performance with a minimum conversion rate of 40%

Deactivation mechanism has also been analyzed to evaluate the real case application performances. In this aging test, ultra high purity air is used to conduct tests to exclude any contaminants that might be introduced. In real world, even though the air purity at high altitude is high, there are still a few sources of contaminants for the catalysts, including lubricants and hydraulic fluids, salt water mist which is high over ocean and exotic air containing sulfur and phosphorous. These complicated cases are not

evaluated in this research. The focus will be on the temperature effect on the catalyst only. The deactivation mechanism that involves temperature includes carbon fouling, catalyst particle size change, crystallite sintering, thermal degradation and metal-support interaction. The fresh and aged catalysts are compared with dispersion results for utilization of the active sites. Dispersion dropped from fresh catalyst of 31.4% to aged catalyst of 15.5%, indicating the available catalysts are fewer. An experiment was also carried out to verify the reduced active sites. Since low temperature ozone decomposition is largely dependent on the reaction rate rather than mass transfer rate, the fresh and aged catalysts were also compared by running low temperature ozone decomposition. The aged sample did show less catalyst activity than the fresh sample, indicating the reduced active sites.

III.5. Conclusion

Catalytic reactors for high mass flow applications usually involve long reactor length to increase contact time and improve catalytic performance. However, this can be a huge disadvantage if the weight and volume are limited on certain platforms. Heterogeneous catalysis using MFEC to remove ozone for aircraft cabin air cleaning was studied in this research. MFEC has demonstrated much higher gas-solid mass transfer rate compared with conventional monolith reactors. Single pass remove efficiency is increased accordingly. To further increase the catalytic performance of MFEC, a pleated structure was used in this research, which offered a larger area for catalyst loading and reduced effective velocity within the material. Both noble metal and transition metal

catalysts were tested for ozone decomposition at high temperature and high mass flow rate conditions. Since the contact time was shortened because of the high face velocities, the reaction was limited by the external mass transfer rate, meaning the available active sites on the surface of catalyst support is of key importance. This has been verified by running a comparative experiment of entrapping the same number but different pore size supports. In addition, both groups of catalysts showed high initial conversion rate, but noble metal catalysts performed much better in terms of aging. Deactivation mechanism analysis confirmed that noble metal based catalysts are preferred in long term applications. Moreover, humidity was found to have an adverse effect on the catalyst performance due to blockage of the active sites. MFEC, as a new matter of structure, has shown great potential in offering high performance heterogeneous catalysis while maintaining proper pressure drop and weight and volume of the reactor. MFEC is also a potential substitute for packed bed and monolith reactors to remove other environmental pollutants at high mass flows if designed properly.

Nomenclature

A pre exponential factor

a surface area (m^2)

C concentration (ppm)

D diffusivity ($m^2\ s^{-1}$)

E_a apparent activation energy ($J\ mol^{-1}$)

k constant

PF pleat factor

R universal gas constant (J mol^{-1} K^{-1})

Sc Schmidt number

Sh Sherwood number

T temperature (K)

v velocity (m/s)

X overall effectiveness

x volume fraction

Greek

η effectiveness factor

ρ density (kg m^{-3})

ϕ Thiele modulus

φ sphericity

Subscript

A component

b bed

c support

e effective

i inlet

M molecular

m mass

o outlet

p particle

r reaction

References

[1] D.K. Harris, D.R. Cahela, B.J. Tatarchuk, Composites: Part A 32 (2001) 1117-1126.

[2] D.R. Cahela, B.J. Tatarchuk, Catalysis Today 69(2001) 33-39.

[3] H. Yang, D.R. Cahela, B.J. Tatarchuk, Chemical Engineering Science 63 (2008) 2707-2716.

[4] R.K. Duggirala, C.J. Roy, H.Y. Yang, R.R. Kalluri, D.R. Cahela, B.J. Tatarchuk, 232nd ACS National Meeting, 2006.

[5] P. Dhage, A. Samokhvalov, D. Repala, E.C. Duin, M. Bowman, B.J. Tatarchuk, Industrial & Engineering Chemistry Research 49(2010) 8388-8396.

[6] M. Sheng, H. Yang, D. Cahela, B. Tatarchuk, Journal of Catalysis 283 (2011) 254-262.

[7] W.H. Zhu, M.E. Flanzer, B.J. Tatarchuk, Journal of Power Sources 112(2002) 353-366.

[8] R.A. Sothen, B.J. Tatarchuk, HVAC&R 14(2008), 841-860.

[9] R.A. Sothen, B.J. Tatarchuk, HVAC&R 15(2009), 269-286.

[10] R.R. Kalluri, D.R. Cahela, B.J. Tatarchuk, Applied Catalysis B: Environmental 90 (2009) 507-515.

[11] R.M. Heck, R.J. Farrauto, Catalytic air pollution control: commercial technology, Van Nostrand Reinhold, New York, 1995

[12] R.M. Heck, R.J. Farratuo, H.C. Lee, Catalysis Today 13(1992) 43-58.

[13] U. Lassi, Dissertation, University of Oulu, 2003.

[14] C.H. Bartholomew, Applied Catalysis 212 (2001) 17-60.

[15] R.C. Sullivan, T. Thornberry, J.P.D. Abbatt, Atoms. Chem. Phys.4 (2004) 1301-1310.

[16] T. Kameya, K. Urano, J. Environmental Engineering 128(2002) 286-292.

[17] B. Dhandapani, S.T. Oyama, Applied Catalysis B: Environmental 11 (1997) 120-166.

[18] R.J. Hill, D.L. Koch, J. Fluid Mech. 465 (2002) 59-97.

[19] H.A. Al-Abadleh, V.H. Grassian, Langmuir 19 (2003) 341-347.

[20] A.L. Goodman, E.T. Bernard, V.H. Grassian, J. of Physical Chemistry 105 (2001) 6443-6457.

[21] V.H. Grassian, J. of Physical Chemistry 106 (2002) 860-877.

[22] P.N. Dwivedi, S.N. Upadhyay, Industrial & Engineering Chemistry Process Design and Development 16 (1977) 157-165.

Chapter IV. Heat Convection in Sintered Microfibrous Entrapped Catalysts Material

IV.1. Abstract

Conventional packed bed and monolith reactors manufactured with metal oxides have poor heat transfer characteristics. Highly exothermic reactions carried out in these reactors usually have uneven radial temperature distributions, causing shorter catalyst lifespan and lower catalyst effectiveness. Microfibrous Material Entrapped Catalyst (MFEC) is a new matter of structure which improves catalyst bed performance by using high thermal conductivity metal fibers. This fiber media has been introduced in highly exothermic reaction applications to enhance heat transfer and catalytic performance. In this research, MFEC are studied in high volumetric flow environments, where pressure volume (PV) work across fiber media generates large amounts of heat. Forced convection in this condition for MFEC is studied by numerical method. Radial and axial temperature distributions are acquired by both numerical and experimental method, which are compared at different system conditions. Nusselt number is calculated based on temperature distribution results. Results indicate that larger temperature difference exists between centerline and wall at higher face velocities, though PV work generates more heat at these velocities. Therefore, heat convection is enhanced at higher face velocities. Besides, heat convection for different metal fibers is investigated theoretically and experimentally, indicating that heat convection can be enhanced by using more thermally conductive metal fibers.

Keywords: Metal Fiber, Convection, Temperature Distribution, Nusselt Number

IV.2. Introduction

IV.2.1. Background

Transport phenomena in fixed bed and porous media are of great importance in practical applications. Fixed beds, including packed beds and monolith, are widely used in engineering practice. These beds work well as low speed heterogeneous reactors, since they provide high surface area and relatively high contact efficiency. However, these traditional catalyst beds all possess properties of low thermal conductivity because of materials used, including alumina, silica, titanium oxide for example. In highly exothermic applications, these beds are limited in size to reduce maximum centerline temperature and increase catalyst lifespan. For instance, Sheng *et al.* [1] applied MFEC in Fischer–Tropsch synthesis. At low face velocities, they found that MFEC enhanced the conductive heat transfer in the radial direction of the reactor by several folds compared with packed bed reactors. This has decreased the temperature difference between the centerline and wall by several hundred degrees, which significantly enhanced the catalyst life, effectiveness and selectivity. In this research, MFEC is studied under heat convection conditions, where PV work, not highly exothermic chemical reactions, act as the major heat source. A typical example of this application is pushing air through ozone filter for a commercial aircraft. High face velocity air through the filter generates large amounts of heat, typically 1548W by air compression at a face velocity of 30 m/s.

Attempts have been made by Tsotsas et al. [2] to enhance the heat transfer in conventional reactors. The most effective way is to substitute the metal oxide support with a more thermally conductive material. Since the sinter-lock structure of MFEC material can be made by highly thermal conductive metal fibers, including copper, nickel and silver, MFEC is one of the potential solutions of enhancing heat transfer at highly exothermic applications.

The objective of this paper is to theoretically and experimentally study heat convection in microfibrous material. To understand the heat convection in microfibrous media, a numerical model has been attempted to analyze the temperature distribution on a flat microfibrous sheet at steady state. Koch and Brady's ensemble averaging method [3-4] is used in the numerical model to predict radial and axial heat transfer coefficient in the presence of heat convection. Temperature distribution profile is acquired at different face velocities by both theoretical and experimental methods. Nusselt number is calculated according to the temperature distribution profile to compare the degree of convection at various velocities. Furthermore, experimental effort has been made to measure the temperature distribution at different high face velocities for MFEC manufactured using different metal fibers. These results are also compared with Nusselt number calculations to evaluate the effect of thermal conductivity of the fibers on the heat convection at high volumetric flow condition. This model serves to provide design parameters for catalytic reactors applied at high mass flow conditions.

IV.2.2. Microfibrous Entrapped Catalysts (MFEC)

Microfibrous material is high performance porous media [5-6] first developed at Auburn University. Figure IV-1 shows SEM images of microfibrous material with and without entrapped particles. This material is manufactured using traditional wet-lay process with 2-20 μm diameter metal (nickel, stainless steel, and copper) fibers. This material can entrap catalyst support particles as small as 20μm so that pre-manufactured catalysts can be used to make reaction beds. Intra-bed mass transfer and contact efficiency are enhanced by the small entrapped particles. This material also has the property of high voidage compared with similar size particle packed bed and monolith reactors, which results in a smaller pressure drop especially in high velocity applications. Heat conduction property of metal fiber materials was also studied experimentally. Results indicated that the radial thermal conductivity is significantly enhanced for heat conduction, since the majority of fibers in the material sheet are aligned in the radial direction because of the wet-lay process used for manufacturing. This features has enabled MFEC to be used in various highly exothermic reactions to maintain a proper temperature distribution within the reactor bed, which also enhances the performance of the catalyst as well as the lifespan of catalysts.

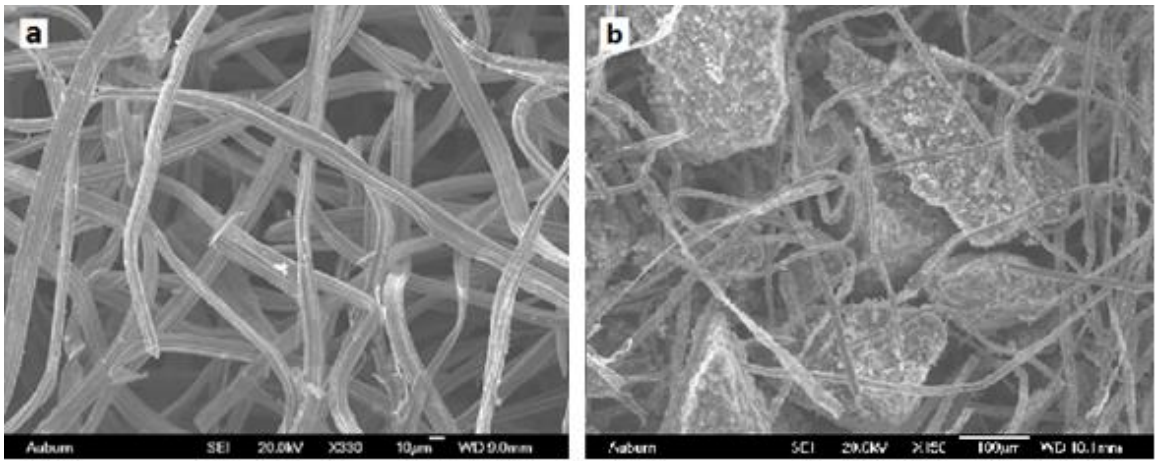

Figure IV-1. SEM image of microfibrous material: (a) 8 μm nickel fiber, (b) 8 μm nickel fiber entrapped with 150-250 μm alumina particles

IV.3. Convective Heat Transfer Model

IV.3.1. Heat Transfer Equation

Previous efforts [7] have been made to obtain the velocity profile within the MFEC using numerical method. Though a similar process is required for the temperature distribution profile, heat transfer within the microfibrous media is much more complicated, because the heat transfer coefficient, acquired theoretically and verified experimentally, is structure dependent. Microfibrous media are made from wet-lay process, causing the majority of the fibers aligned parallel to the radial direction of the sheet. The number of fibers aligned to the axial direction is scarce. The structure can be viewed as layers of fibers stacked together. Due to the nature of this structure, the fiber network is well connected in the radial directions, while different layers of fibers are only

connected by the small junction points that are created by sintering. Therefore, heat conduction in the radial direction is much more intense than in the axial direction. However, when microfibrous material media are used in high face velocity applications, the overall heat transfer is a much larger quantity, since convective contribution to heat transfer in stream-wise direction is relatively large. In this model, heat transfer in two directions are treated separately by considering two heat transfer coefficients, the radial heat transfer coefficient k_r and the axial heat transfer coefficient k_z. First, we start with general heat transfer equation for compressible gases.

$$\rho c_p \frac{DT}{Dt} = -(\nabla \cdot q) - \left(\frac{\partial ln\rho}{\partial lnT}\right)_p \frac{Dp}{Dt} - (\tau : \nabla v) \quad \text{(IV. 1)}$$

Bird *et al.* [8] presented this equation for cylindrical coordinates in the following form.

$$\rho c_p \left(\frac{\partial T}{\partial t} + v_r \frac{\partial T}{\partial r} + \frac{v_\theta}{r}\frac{\partial T}{\partial \theta} + v_z \frac{\partial T}{\partial z}\right) = -\left[\frac{1}{r}\frac{\partial}{\partial r}(r q_r) + \frac{1}{r}\frac{\partial q_\theta}{\partial \theta} + \frac{\partial q_z}{\partial z}\right] - \left(\frac{\partial ln\rho}{\partial lnT}\right)_p \frac{Dp}{Dt} - (\tau : \nabla v) \text{ (IV. 2)}$$

To address the heat transfer for two directions separately, heat transfer terms are treated with different heat transfer coefficients q_r and q_z. The last term in the equation is expanded and simplified by assuming v_x and v_y are negligible compared with v_z and can be expressed as

$$(\tau : \nabla v) = \left\{-\mu\left[2\frac{\partial v_z}{\partial z}\right] + \left(\frac{2}{3}\mu - k\right)\frac{\partial v_z}{\partial z}\right\}\left(\frac{\partial v_z}{\partial z}\right) = -\left(\frac{4}{3}\mu + k\right)\left(\frac{\partial v_z}{\partial z}\right)^2 \quad \text{(IV. 3)}$$

Pressure drop across the filter is determined by a permeability experiment on a flat sheet MFEC. As mentioned earlier, the media structure can be treated as layers of fibers stacked together. It is assumed that the flow is under continuous compression when passing through the media. The pressure decreases linearly from upstream to downstream, which leads to the following form

$$p_{abs} = -\frac{\Delta p}{l} z + p_{atm} + \Delta p \quad \text{(IV. 4)}$$

With all the simplifications, the final form of heat transfer equation is expressed as follows:

$$\rho c_p \left(\frac{\partial T}{\partial t} + v_z \frac{\partial T}{\partial z}\right) = \frac{k_r}{r}\frac{\partial T}{\partial r} + k_r \frac{\partial^2 T}{\partial r^2} + k_z \frac{\partial^2 T}{\partial z^2} + v_z \frac{\Delta p}{l} \quad \text{(IV. 5)}$$

where

$$c_p = \epsilon c_{pf} + (1 - \varepsilon)\mathrm{c_{ps}} \quad \text{(IV. 6)}$$

IV.3.2. Numerical Process

The partial differential equation (PDE) was discretized with central difference formulation and integrated by Euler explicit method. Grid dependence was tested for the numerical solution. Final results were generated based on uniform grid spacing, using 600 divisions in radial direction and 20 in the axial direction. Domain was also meshed with 700 divisions in radial and 30 in axial for comparison. Both cases were calculated to steady state based on same error estimate and the final results were identical. Von Neumann stability analysis was performed for the PDE, indicating that the scheme was conditionally stable for Courant number less than 0.5. Boundary conditions for the inlet, outlet, wall, and centerline of the regime are shown in Figure IV-2 and also described as follows.

$$\text{@ z=0 (j=1) T=473 K; @z=z (j=M+1) } \frac{\partial \mathrm{T}}{\partial \mathrm{z}} = 0\text{; @r=0 (i=1) } \frac{\partial \mathrm{T}}{\partial \mathrm{r}} = 0 \quad \text{(IV. 7)}$$

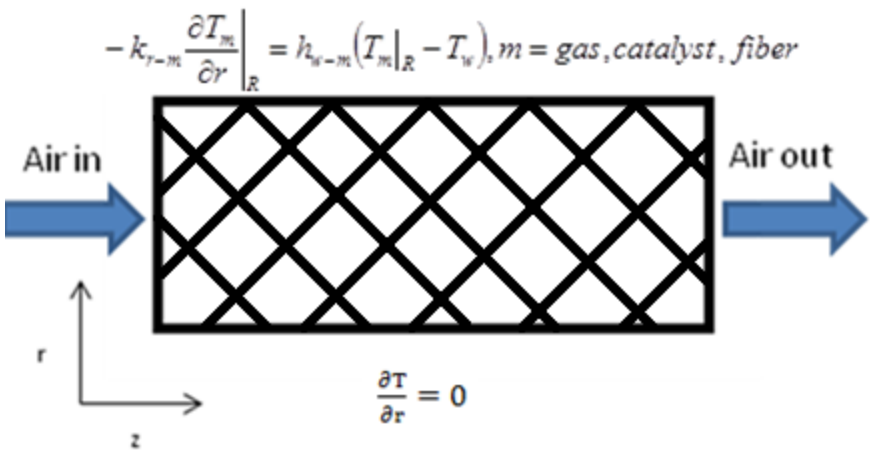

Figure IV-2. Schematic of centerline and boundary condition used in temperature profile simulation

IV.4. Material and Methods

IV.4.1. Test Set Up

Figure IV-3(a) shows the schematic of the high volumetric test system. The high velocity test set up includes a 40 horse power blower (Fan Equipment Company Inc.) circulating air inside a closed loop system. A variable drive is used to control the system speed ranging from 10-40 m/s. The system is running at near atmospheric pressure. Omega® J type thermocouples are located at several positions on the system, including the outlet of the blower, two elbows on the rig, upstream and downstream of the reactor and the blower plate. Two pressure gauges are located upstream and downstream of the reactor to monitor the pressure drop across MFEC reactor. A single pressure gauge is located at the inlet of the blower to test the absolute pressure, which is used to calculate

the absolute pressure at other locations on the rig. System speed is calculated by the pressure drop across a 10’ bare section on the test rig. This speed is verified by a Dwyer® 1/8” stainless steel pitot tube at different temperatures. All thermocouples and pressure gauges are monitored and controlled by a central PLC unit.

The system heat balance is illustrated in Figure IV-3(b). System temperature, controlled by balancing several energy sources and cooling powers, can continuously change from 100℃ to 200℃. Since the system is running at high face velocities and the surface area of the test loop wall is large, the skin friction of the moving air with the wall generates large amounts of heat (~3 kW at 30 m/s face velocity). The amount of heat generated is proportional to the face velocity in the rig. Therefore, at lower speeds, less heat is generated. Six 1800 W heaters are introduced on the blower plate and work as auxiliary heating source in this condition. When the system is overheated, some heated air is vented through a valve located at the outlet of the blower and room temperature air is introduced to cool down the system. The majority of the system is insulated with mineral wool so that when system speed changes, the temperature response is quick and does not affect the catalytic performance from time to time.

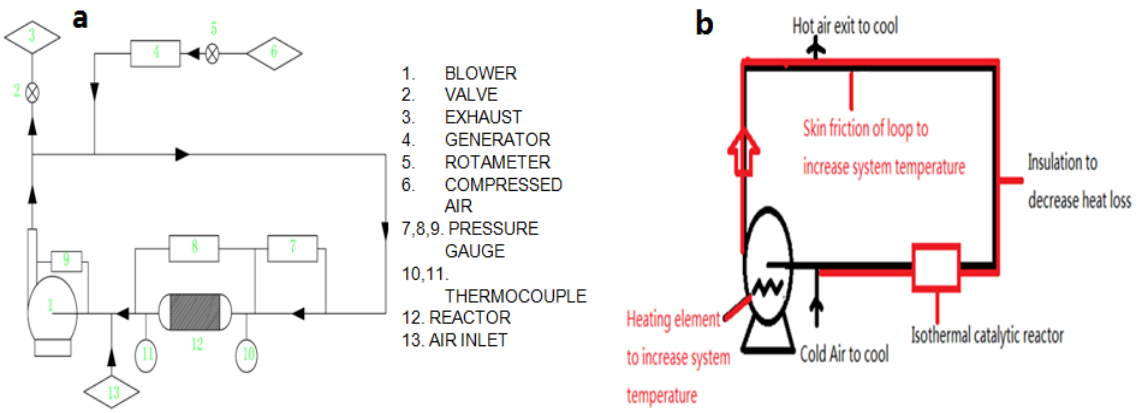

Figure IV-3. Schematic of high face velocity test setup: (a) Schematic of test set up (b) Heat balance of the system, heat source in red, cooling source in black

IV.4.2. Microfibrous Material Preparations

Traditional low-cost wet-lay process was used to prepare microfibrous material. In this process, the slurry consisted of metal fibers (8 μm nickel) and cellulose was made by rapid stirring. This slurry is then transferred to an 8"×8" head box, where alumina catalyst support is added and mixed with the slurry. Then excess water is drained to manufacture the pre-form microfibrous sheet. Pre-form sheets are dried overnight before entering the sintering furnace. BTU-1000 controlled atmosphere electric sintering furnace is used to continuously sinter multiple pieces of MFEC sheets in a reducing environment (H_2) at high temperatures (1000℃ for nickel fiber). After sintering, microfibrous media gained considerable mechanical strength so that it can be applied in a variety of applications. As mentioned above, catalyst support particles (Al_2O_3, SiO_2, and TiO2 for example) were added when preparing the slurry. These sheets with entrapped particles will be impregnated with selected catalyst nitride solution using incipient wetness process.

Impregnated sheets are then dried and calcinated at 350-500℃ to obtain required catalyst form.

IV.4.3. Temperature Distribution Measurement

In this research, temperature distribution is not only used to verify model accuracy, but also used to calculate Nusselt number to evaluate the strength of convection at different conditions. Radial and axial temperature distribution is measured respectively. An Omega® multi point thermocouple is used to measure the radial temperature distribution. This 1/16" diameter thermocouple is sandwiched within the MFEC to test the radial temperature distribution. Figure IV-4 shows the schematic of the thermocouple on the system. Six sensing points, which are 1 inch apart from each other, are located on the thermocouple. The thermocouple is moved 0.5" along the radial direction between two measurements so that temperature distribution can be measured every 0.5" for accuracy and avoid any position dependence of the temperature distribution. Wall temperature on the test rig is acquired by Omega® SA1-J-SC surface thermocouple. As to axial temperature distribution, multi point thermal couple cannot be applied in this case, because the thickness in this direction is not enough to collect multiple data. As an alternative solution, three Omega® SA1-J-SC surface thermocouples were applied in the radial direction on both upstream and downstream surface of the MFEC.

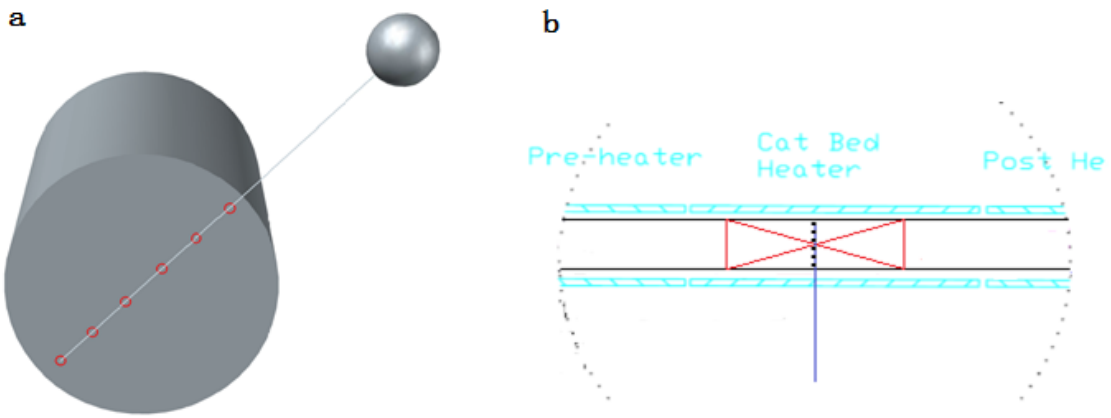

Figure IV-4. a. Position of Omega® multi point thermocouple used in radial temperature distribution test in MFEC; b. Position of thermocouple on reactor and position of bed heaters

IV.4.4. Flat Media Pressure Drop Measurement

The quadratic form pressure drop was measured using a 1" diameter steel pipe [11]. House air of 80 psi was supplied as velocity inlet for microfibrous material. The test media were blank 8 µm diameter nickel fiber with media thickness of 2.5 mm and media entrapping 150-250 µm alumina particles. Media were kept at a 122 cm distance from pipe inlet so that fluid was fully developed before entering the media. Also, a reasonable length (30 cm) was maintained downstream to avoid any unnecessary flow disorder. Air speed was controlled by two King instrument rotameters. Due to the limitation of air pressure, the maximum face velocity was limited at 8 m/s. Pressure drop were measured using IDP10-T differential pressure transmitter which connect 50 mm upstream of the media and 125 mm downstream. Two inch diameter samples were punched from pre-

manufactured microfibrous media. Each sample was test three times with increasing and decreasing speed for average result. Since a metal wire mesh was used as downstream support for the microfibrous material, the background resistance was measured with the same method and deducted from total pressure drop value. Figure IV-5 shows the equipment sketch used to test the flat media.

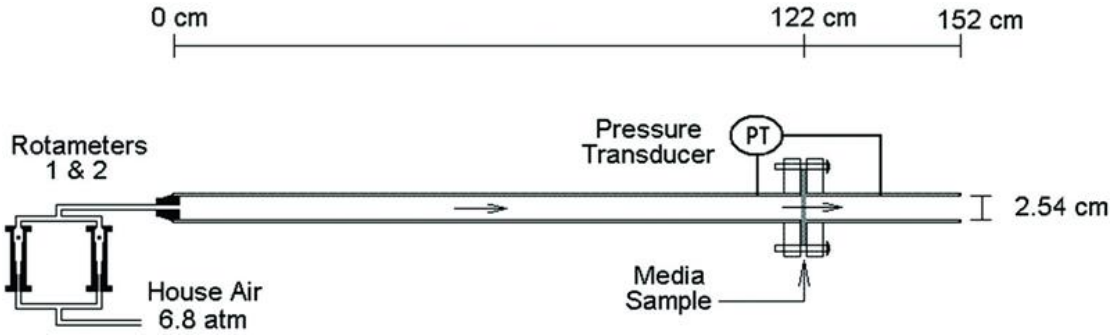

Figure IV-5. Pressure drop test rig for 1" flat MFEC sheet at face velocities up to 8 m/s

IV.5. Result and Discussion

Temperature distribution profile is first calculated using the model introduced in part two. Some model parameters, including radial and axial heat transfer coefficients, are determined using theoretically determined values. These parameters are affected by several different factors, including voidage percentage, fiber alignment and fiber thermal conductivity. Since voidage percentage changes significantly at different face velocities,

theoretically determined parameters are preferred in this model. The accuracy of these parameters is confirmed with radial and axial temperature distribution profiles. Experimentally acquired temperature distribution profile is used to verify the model accuracy so that the model can be also used to calculate heat convection at different test condition. Later, verified model can be used to evaluate running condition that is not available for experiments.

IV.5.1. Axial and Radial Heat Transfer Coefficient

Heat transfer has been previously studied for fibrous media at heat conduction conditions by both experimental and theoretical methods. For MFEC material manufactured by wet lay process, fiber alignment has dominant effect on its heat transfer properties, since majority of fibers are preferably aligned in 2D plane. Fiber aligned in the direction perpendicular to the stream-wise direction (radial direction) usually act as turbulence enhancer, while fibers aligned in the axial direction does not. Therefore, heat convection in both directions are enhanced because of the strengthening of turbulent flow. However, heat conduction is still the dominant heat transfer route due to the well-constructed network of metal fibers. Koch and Brady [3-4] studied the heat transfer for fibrous media of different alignment and introduced ensemble averaging method to determine mass and heat transfer coefficients in fibrous materials. The mass and heat transfer for a single fiber was investigated and this property was averaged over a large regime. Peclet number is used to divide different transport regimes. For the low Reynolds number regime, Sheng et al. [1] experimentally determined axial and radial for MFEC

material. Their data showed the apparent increment in radial thermal conductivity when Reynolds number increased, while axial thermal conductivity only showed marginal increment. Though transport properties are linear with average bed velocity, the properties are segmental at different velocity regime. In this study, effective thermal diffusivity is determined using ensemble averaging method. Heat transfer coefficients for traverse and longitude directions are determined by multiplying theoretically determined thermal diffusivity with volumetric heat capacity [12].

$$\mathrm{k} = D_f * C_v \tag{IV. 8}$$

In high mass flow applications, the Peclet number is relatively high. At this condition, the axial and radial heat dissipation obtained by ensemble averaging method for an isotropic bed with flow in x direction is

$$D_{xx} = D_f \left\{ \frac{1}{1-\phi-\phi m^{-1}} + \frac{171}{3200}\pi^3 \frac{a^2}{k\phi} |\wp| \right\} \tag{IV. 9}$$

$$D_{yy} = D_{zz} = D_f \left\{ \frac{1}{1-\phi-\phi m^{-1}} + \frac{9}{6400}\pi^3 \frac{a^2}{k\phi} |\wp| \right\} \tag{IV. 10}$$

IV.5.2. Inside wall heat transfer coefficient

The inside wall heat transfer coefficient is another important parameter that determines the overall heat transfer rate. Thermal resistance between the reactor bed and the reactor wall affects the temperature difference between them. Thermal resistance depends not only on the material used for the bed and wall, but also depends on uncertain factor like contacts between the wall and bed. For conventional reactor, packed bed

generally contact the reactor wall better than monolith, because monoliths are designed smaller than the reactor size to fit the structure. Since MFEC is relatively flexible than the packed bed and monolith, at least 5% percent larger than the diameter size is used to guarantee a proper contact between the MFEC bed and the reactor wall.

Dixon et al. [9-10] studied the wall heat transfer coefficient for packed bed. Since the major heat flux in the radial direction for MFEC is heat conduction in the fiber network, the solid/wall heat transfer coefficient modified for MFEC is estimated using the following equations derived from wall-liquid mass transfer equation for fixed beds.

$$h_{ws-fiber} = \frac{2.12 k_{r-fiber}}{1.5 d_f} \frac{x_{fiber}(1-bedvoidage)}{0.6} \qquad \text{(IV. 11)}$$

IV.5.3. Axial and Radial Temperature Distribution

No apparent temperature rise or drop is monitored between upstream and downstream temperatures at different positions (centerline, half radius and 0.8 radius) on the MFEC sheet through simulation. Experimental determined profile showed consistent results in the axial direction. The small temperature difference is mainly caused by the fiber alignment in the MFEC sheet. Because the majority of the fibers are aligned in the radial direction, heat conduction by the metal fibers is the dominant heat flux direction. In the axial direction, the only heat conduction through fibers is the junction points created by the sintering process of the fibers. However, the area of the junctions, compared with total cross area of fibers, is negligible. Therefore, heat conduction in the axial direction is very small. Even though the convective heat transfer coefficient transfer coefficient,

determined by the theoretical method, is not small at all, temperature change is still not noticeable because the thickness of the bed is fairly small.

Before measuring radial temperature distribution within MFEC material, the radial temperature distribution in the empty rig has to be taken, since the results will be combined signals if radial temperature distribution for the empty rig is not a constant. Results for radial temperature distribution in an empty rig taken by a single point thermocouple are shown in Figure IV-6. At 100℃, 150℃ and 200℃, the radial temperatures are same, equaling the incoming air temperature. Besides, at different face velocities, the heat generated by the friction on the rig surface is different, leading to different wall temperatures, which will bring in unfair comparisons between different running conditions. Tape heaters (Figure IV-4) added to the outside wall of the rigs is used to adjust the wall temperature to the upstream air temperature of the reactor. Any temperature increment is caused by the air compression/reaction instead of any other heat source.

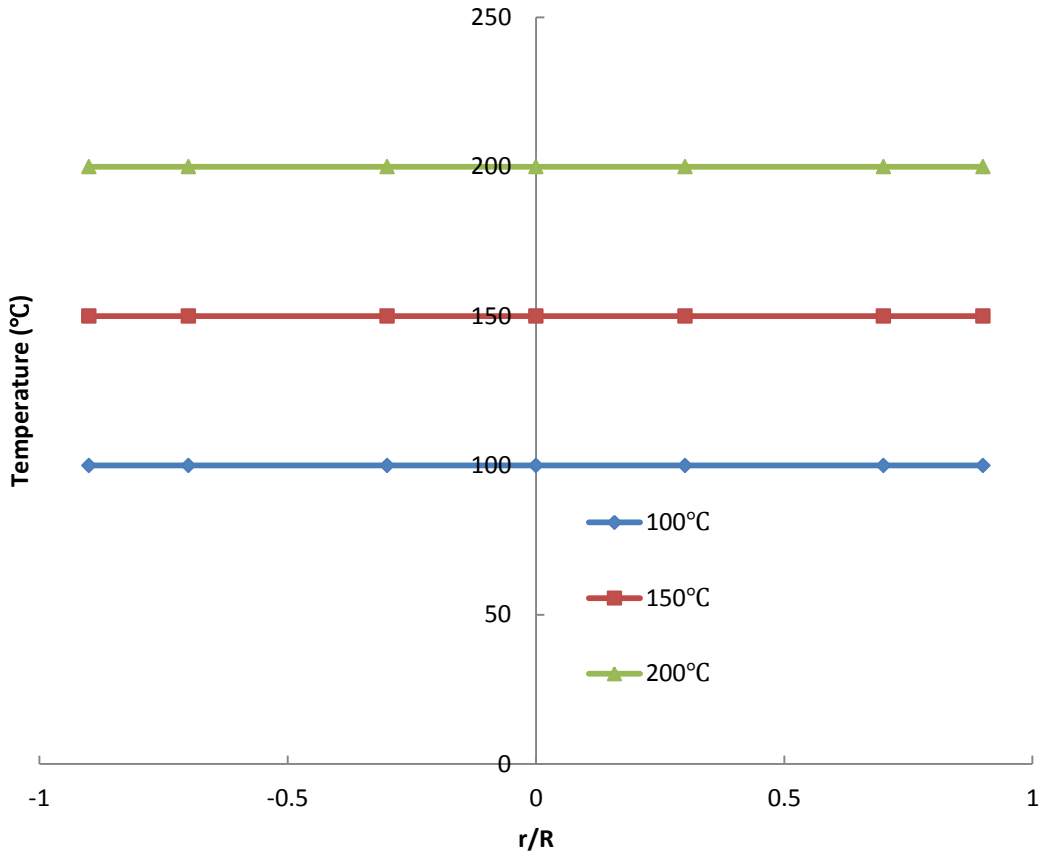

Figure IV-6. Radial temperature distribution in an empty tube for three inlet temperatures at 30 m/s face velocity and atmospheric pressure

The radial distribution within the MFEC material is shown in Figure IV-7. It is shown in the figure that the wall temperature is at the inlet air temperature. The temperature profile, which is higher than the wall temperature, is caused by the air compression work through the MFEC material, namely the PV work. As shown in Figure IV-7, centerline temperature for higher Reynolds number case is higher, since PV work generates more heat at higher face velocities. This higher centerline temperature also causes a steeper temperature profile, generating a larger temperature gradient at the wall.

Although the amount of heat generated by air compression is several times higher at higher face velocities, the highest centerline temperature is not increased significantly. This suggests that the majority of heat generated by the air compression is dissipated in this direction by the well-constructed network of fibers. It is also noted the steep temperature change only remains close to the reactor wall thanks to the high thermal conductivity fibers used. Compared with monolith or packed bed reactor, majority of the bed temperature are evenly distributed, making good contributions to catalyst bed performance and catalyst lift time.

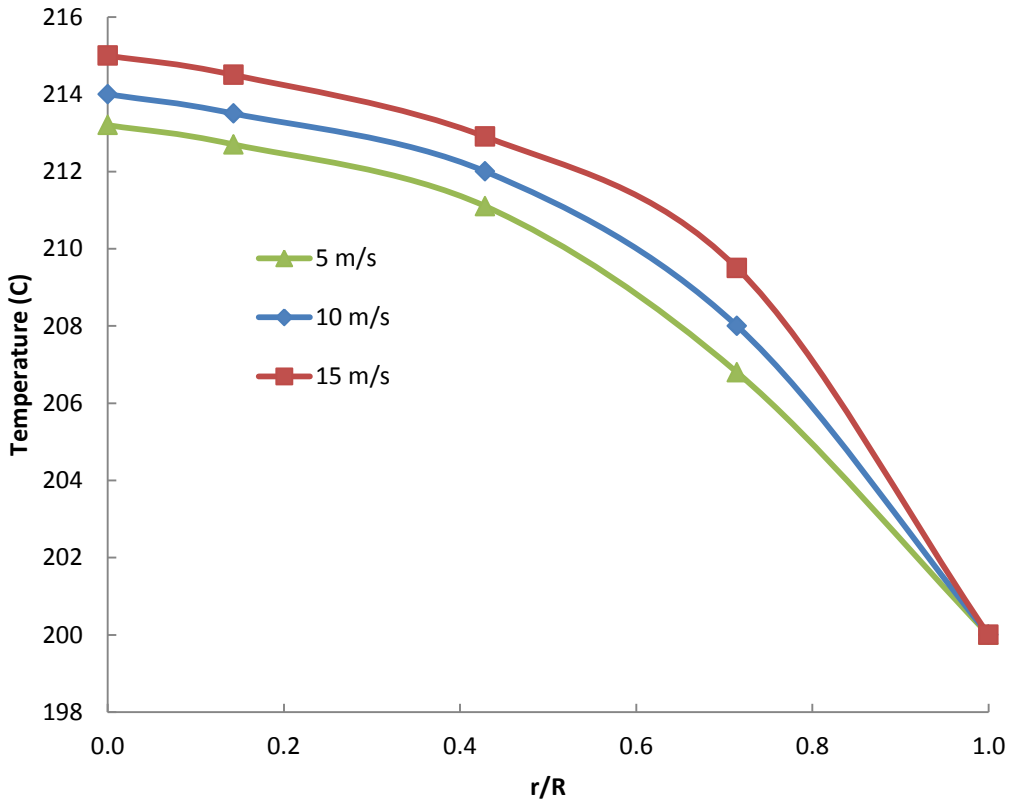

Figure IV-7. Radial temperature distribution within MFEC for three face velocities at atmospheric pressure with inlet temperature of 200℃

In addition, the radial temperature distributions for MFEC made by different materials are also compared. This convective heat transfer model investigates the case where MFEC is used in high flow conditions. Pressure/volume work through the fibrous media generates large amount of heat by air compression. The resulting temperature distribution is similar as the highly exothermic reactions carried out in the reactor. MFEC made by copper fibers has a steeper temperature profile than MFEC made by nickel fibers. Because copper fibers have higher thermal conductivity than nickels and the major fiber network is aligned in the radial direction, heat conduction by the copper fiber network is much stronger than nickel fibers, making the temperature profile more evenly distributed for the copper fiber case.

IV.5.4. Nusselt Number

Nusselt number, the ratio of convective to conductive heat transfer across the boundary, is used to compare heat convection under different running conditions. The average Nusselt number is calculated based on the temperature distribution profile using the Equation 12. Nusselt numbers for system running at different pressures are shown in Figure IV-8. Higher system temperatures contributes to enhance heat transfer because of improvement on radial and axial heat transfer coefficients by using high pressure gases. Nusselt numbers for nickel and copper fibers sheets are shown in Figure IV-9. As discussed above, the major contribution in the radial direction remain the heat conduction through the network of metal fiber. By using higher thermal conductivity material, heat transfer property is enhanced. It is also noted that in any case the Nusselt is substantially

increased with face velocities, which indicates the heat convection enhancement by the high speed fluid. Despite the higher pressure drop penalty introduced by smaller fibers, they can be used to further enhance the convective heat transfer performance, since thermal diffusivity is significantly increased by smaller fiber sizes.

$$Nu = \frac{hD}{k} = \frac{1}{2\pi L/D}\int_0^{L/D}\int_0^{2\pi}(-\frac{\partial T}{\partial r})d\theta dz \qquad \text{(IV. 12)}$$

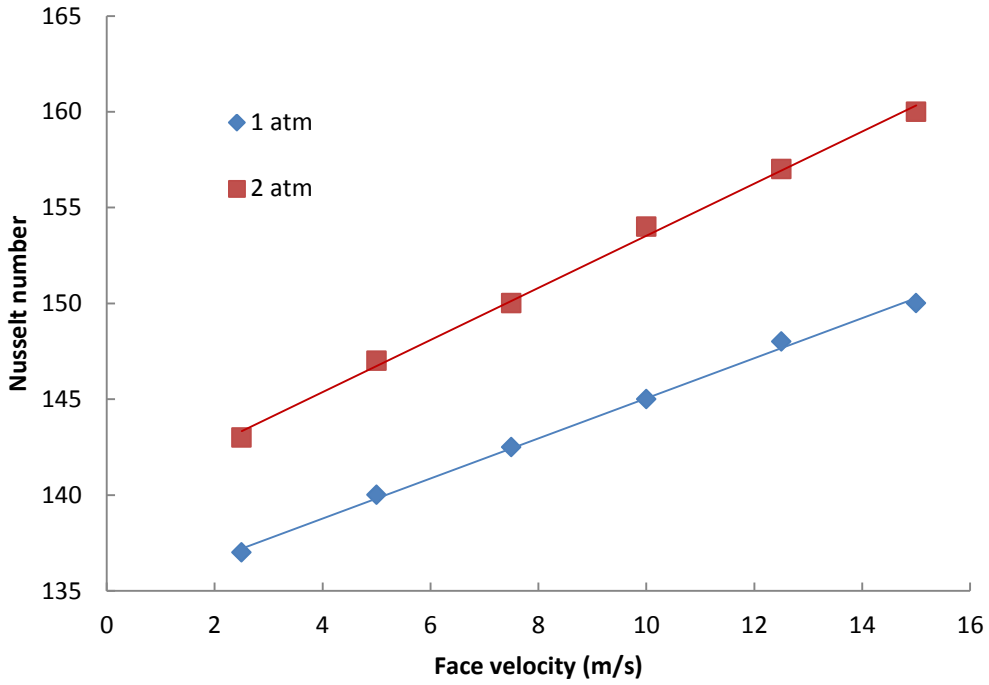

Figure IV-8. Nusselt number at face velocities up to 15 m/s and different system pressures

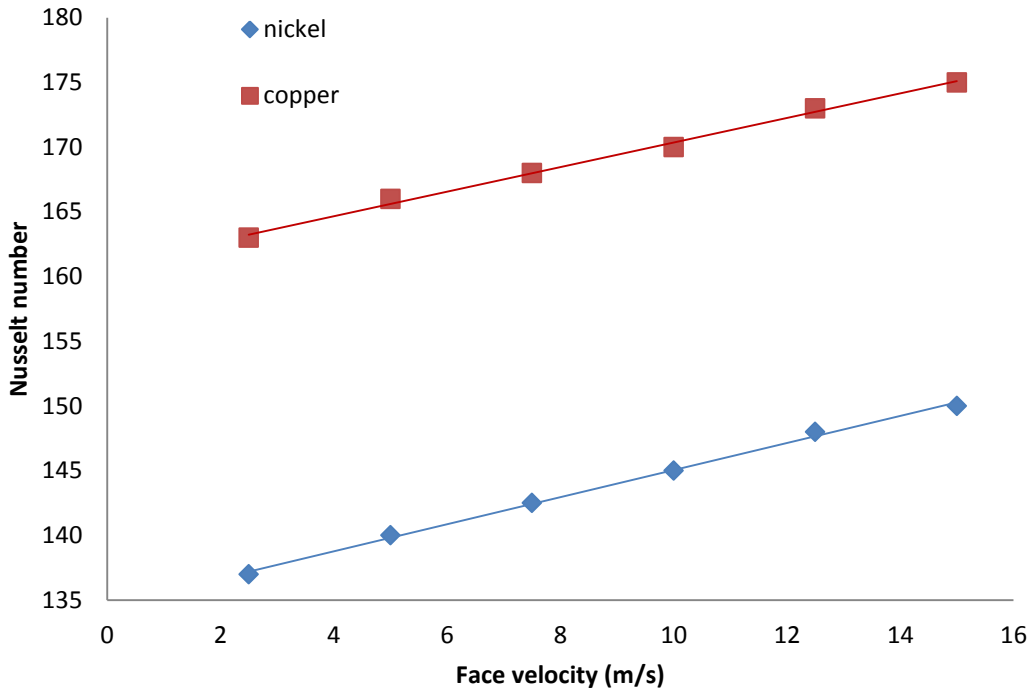

Figure IV-9. Nusselt number at face velocities up to 15 m/s for MFEC made of nickel and copper fibers

IV.6. Conclusion

A convective heat transfer model was established to numerically evaluate the performance of MFEC at mass flow conditions. This model considered several detailed conditions in reactor design, including bed voidage, fiber/particles size and fiber thermal conductivity. Axial and radial temperature profile within MFEC material has been acquired by numerically solving the heat transfer equation with axial and radial heat transfer estimated by ensemble averaging method and pressure/volume work as heat

source. Axial heat distribution profile showed no apparent temperature rise or drop, indicating low heat transfer in this direction. Radial temperature distribution profile showed steep temperature gradient near the reactor wall. Radial direction is considered as the major heat dissipation direction as the majority of fibers are aligned in this direction. Experimentally determined axial and radial temperature distribution profiles confirmed the accuracy, which is expected to be used to analyze test conditions that are not easily accessible by lab experiments. In typical high mass flow applications, pressure/volume work generates larger amounts of heat by air compression through reactor beds, which created high temperature spots in conventional packed bed or monolith reactors. These high temperature hot spots usually decrease catalyst lifespan in the beds. By measuring and calculating the temperature distribution in MFEC material, it is proved that the well-constructed network of metal fibers dissipate heat properly through radial direction and maintain highest temperature spot low compared with conventional reactors. This property endows MFEC material with huge advantage over conventional reactor in terms of catalytic activity, lifespan and consumption. It is also found that higher Reynolds number can enhance heat dissipation. Fibers made of higher thermal conductivity significantly improve heat dissipation. The overall thermal performance of MFEC at high mass flow conditions depends on the velocity, material voidage and thermal conductivity.

Nomenclature

C heat capacity

k constant

p pressure

q heat flux

r radius

T temperature

t time

v velocity

Greek

ρ density

μ viscosity

Subscript

z z direction

θ θ direction

References

[1] M. Sheng, H. Yang, D. Cahela, B. Tatarchuk, Novel catalyst structures with enhanced heat transfer characteristics, Journal of Catalysis 283 (2011) 254-262

[2] E. Tsotsas, H. Martin, Thermal conductivity of packed bed: A review, Chemical Engineering and Processing: Process Intensification, Vol. 22(1), pp. 19-37, 1987

[3] D.L. Koch, J.F. Brady, The effective diffusivity of fibrous media, AICHE Journal Vol. 32, No. 4 April 1986

[4] D.L. Koch, J.F. Brady, Dispersion in fixed beds, Journal of Fluid Mechanics, 154, 399 (1985)

[5] Daniel K. Harris, Donald R. Cahela, Bruce J. Tatarchuk, Wet layup and sintering of metal-containing microfibrous composites for chemical processing opportunities, Composites: Part A, Vol. 32, pp. 1117-1126, 2001

[6] D.R. Cahela, B.J. Tatarchuk, Permeability of sintered microfibrous composites for heterogeneous catalysis and other chemical processing opportunities, Catalysis Today, Vol. 69, pp. 33-39, 2001

[7] Q. Gu, B. Tatarchuk, A CFD Pressure Drop Model for Microfibrous Entrapped Catalyst Filters using Micro Scale Imaging, AICHE proceeding, 2013

[8] Bird, R., W. Stewart, E. Lightfoot, Transport Phenomena, 2nd ed. New York, John Wiley & Son, Inc., 2001

[9] A. G. Dixon, J. Arias, J. Willey, Wall-to-liquid mass transfer in fixed beds at low flow rates, Chemical Engineering Science, Vol. 58(9), pp. 1847-1857, 2003

[10] A. G. Dixon, D. Cresswell, Theoretical prediction of effective heat transfer parameters in packed beds, AIChE Journal, Vol. 25(4), pp. 663-676, 1979

[11] Ryan A. Sothen, Bruce J. Tatarchuk, A semi-empirical pressure drop model: part I-pleated filters, HVAC&R Research, Vol. 14, Number 6

[12] E.L. Foley, R.B. Sawyer, Thermal diffusivity of nickel from 25 to 500℃, Journal of Applied Physics, 35, 3053 (1964)

Chapter V. Ozone Decomposition at Ultra Short Contact Time using Microfibrous Entrapped Catalyst in Pressurized Systems

V.1. Abstract

Microfibrous entrapped catalysts (MFEC) have demonstrated significant improvement in ozone decomposition reactions at high mass flow rate atmospheric pressure condition. In many practical uses, high mass flow application involves high system pressure. Since the change of physical properties for air impact the gas-solid mass transfer rate and pressure drop across the reactor, MFEC reactors are tested at low and high system pressure conditions for ozone decomposition reaction to investigate the pressure effect on effective reaction rate, gas-solid mass transfer rate and heterogeneous contact efficiency. The results indicate that the gas-solid mass transfer rate is marginally enhanced because of the higher effective diffusivity at higher pressures. The enhanced mass transfer rate also enhances effective reaction rate for mass transfer limited reactions. Meanwhile, the heterogeneous contact efficiency, a ratio of log of removal to pressure drop across the reactor, is significantly improved. This is only partially due to the increased reaction rate. The major contribution is the reduced pressure. To maintain same molecular flow rate, the high pressure system is running much slower than low pressure system, leading to a significantly reduced pressure drop ($\sim v^2$). In addition, convective heat transfer properties is studied, which also demonstrates the advantages of high system pressure for catalytic performance.

Keywords: Metal Fiber, System Pressure, Heterogeneous Contact Efficiency

V.2. Introduction

V.2.1. Background

For high mass flow catalysis applications like aircraft ozone remover, automobile catalytic converters and fuel cell cathode air filters, traditional fixed bed reactors have to be modified to adjust to the high pressure drop penalty, while maintaining high catalytic performance and good heat management, since pressure/volume work at high mass flows generates large amount of heat (1548W at 30 m/s). While the transport phenomenon in these applications have changed significantly compared with normal operating conditions, the traditional reactors are not well adapted because of certain disadvantages. The low porosity of the packed bed reactor leads to an unacceptably high pressure drop across the reactor. Meanwhile, both packed bed reactors and monolith reactors made of materials of low thermal conductivity, including alumina, silica, titanium oxide and etc., demonstrate poor heat transfer properties. In highly exothermic application, these beds are limited in size to reduce maximum centerline temperature so that proper catalyst lifetime and performance can be maintained. A new matter of structure with high voidage and good heat transfer properties is demanded because of all these issues. Microfibrous entrapped catalysts offers high voidage, high contact efficiency and good thermal properties by using sinter-lock structure of metal fibers entrapping small size catalyst particles. For instance, Sheng *et al.* [1] has studied the heat conduction property of metal fiber materials experimentally in Fischer–Tropsch synthesis. Their results suggest that the radial thermal conductivity is enhanced

for heat conduction at low face velocity, since the majority of fibers in MFEC are aligned in the radial direction because of the wet lay process used for manufacturing.

In this paper, ozone decomposition reaction is selected to demonstrate the advantage of MFEC to be used in high system pressure and high mass flow condition. Previous study on ozone decomposition reaction at atmospheric pressure and high mass flow condition using MFEC has demonstrated significant improvement in catalytic performance, pressure drop and heterogeneous contact efficiency. However, in most high mass flow condition applications, higher system pressure is often encountered, which changes air properties, mass transfer rate and convective heat transfer properties. The model developed by Koch and Brady [2][3] indicates that the radial and axial heat transfer coefficients are enhanced by the increased system pressure, which will in turn the change the catalytic performance. However, the surface reaction rate is also a function of gas-solid mass transfer rate. Therefore, the catalytic performance of MFEC at high system pressure cannot be calculated using existing models. Pressure drop, on the other hand, is expected to increase dramatically, since the density of air is the main concern. But air speed can be much lower in high pressure system to maintain the same molecular flow as that of low pressure system. On the other hand, the increased air density affects the compressibility of MFEC, form drag and air viscosity. Pressure drop needs to be experimentally tested to understand the pressure effect and be used to evaluate the heterogeneous contact efficiency.

V.2.2. Microfibrous Entrapped Catalysts

Microfibrous material was first developed at Auburn University. Figure V-1 shows SEM images of microfibrous material (8μm nickel fiber) with (Figure 1a) and without (Figure 1b) entrapped particles and a fiber roll (Figure 1c) manufactured by commercial paper making machine. The choice of fiber and entrapped particles type can be made depending on the requirement of catalytic/adsorption process under consideration. This material is manufactured using traditional wet-lay process with 2-20μm diameter metal fibers (nickel, stainless steel, and copper). This material can entrap catalyst support particles as small as 20μm, which significantly enhances inter phase mass and intra bed mass transfer rate [4-6]. This kind of material is also high in voidage compared with packed bed and monolith reactors that are made from similar size particles, which results in a several magnitudes smaller pressure drop, especially in high velocity application. The heat transfer property of MFEC is another major advantage of this material. The heat transfer properties in the radial direction of the material works so well that no significant temperature rise is monitored even in highly exothermic reactions.

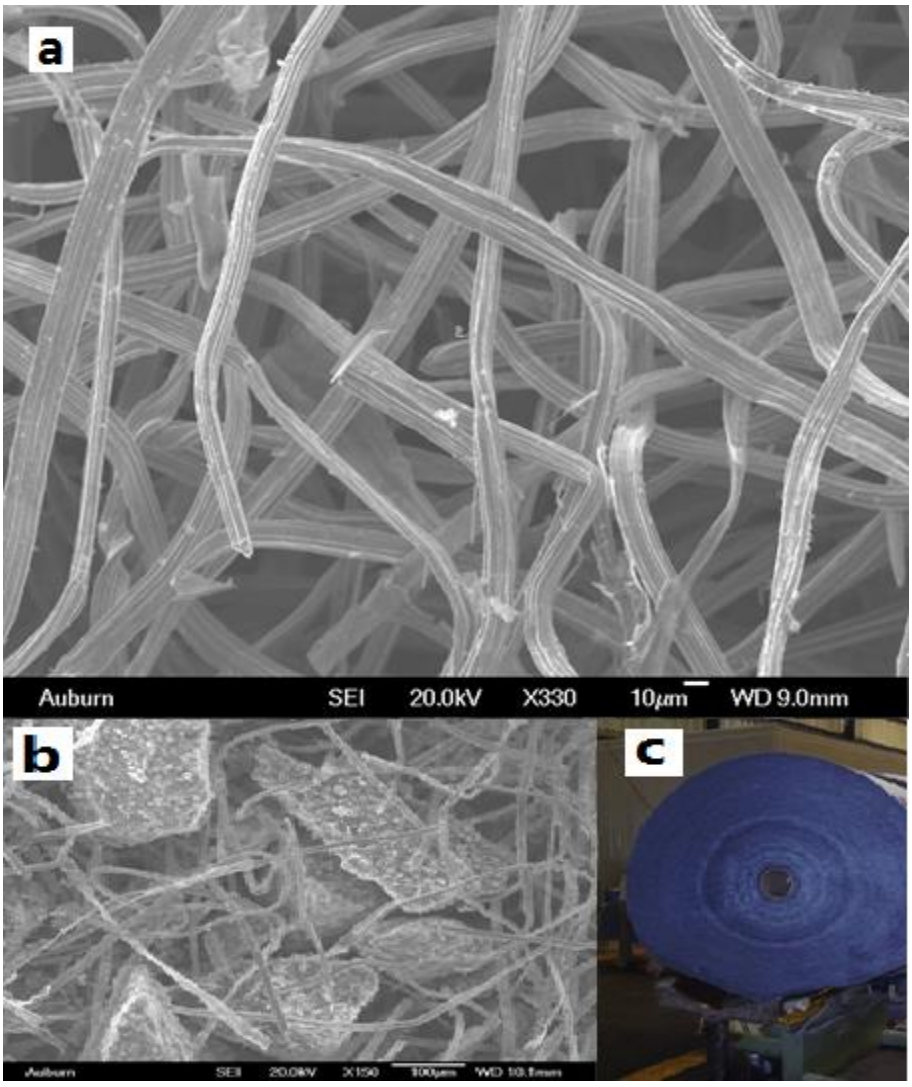

Figure V-1. SEM image of MFEC material: (a) 8 μm nickel fiber, (b) 8 μm nickel fiber entrapped with 150-250 μm alumina particles, (c) microfibrous roll made by paper making machine

The objective of this paper is to theoretically and experimentally understand the advantage of MFEC in high pressure and high mass flow condition as compared to atmospheric application. Pressure drop across the reactor, inter phase mass transfer rate and heat transfer property will be studied theoretically and verified experimentally. The

pressure effect will be evaluated by gas-solid mass transfer rate, pressure drop and heterogeneous contact efficiency. In addition, the convective heat transfer properties in high pressure system will be studied.

V.3. Material and Methods

V.3.1. Atmospheric Test Set Up

The high mass flow test set up is shown in Figure V-2(a). This closed-loop set up is made up of a 40 horse power blower (Fan Equipment Company Inc.) to circulate air at high face velocities (10-40 m/s). Temperatures are monitored at different locations (blower outlet, elbows, reactor upstream, reactor downstream and blower inlet) on the loop using Omega® J type thermocouples. Pressure drop across blower, reactor and a bare section on the rig are recorded using IDP10-T differential pressure transmitters. System speed is acquired by calculating the pressure drop across a bare section on the rig and verified by a Dwyer® 1/8" stainless steel pitot tube at different temperatures. Figure V-2(b) shows the heat balance on the system. The system is constructed as closed loop because of the difficulty of simulating turbine bleed air temperature using a common blower. The skin friction on the pipe wall brings up the system temperature quickly at high face velocities. When the system is running at relatively lower face velocities, six 1800W ring heaters assist with temperature. Besides, the loop is insulated with 2" thick mineral wool to help with the temperature response when the system face velocity

changes. By balancing all the heating sources, the system can be controlled between 100℃ and 200℃, which is in the operating range of turbine bleed air.

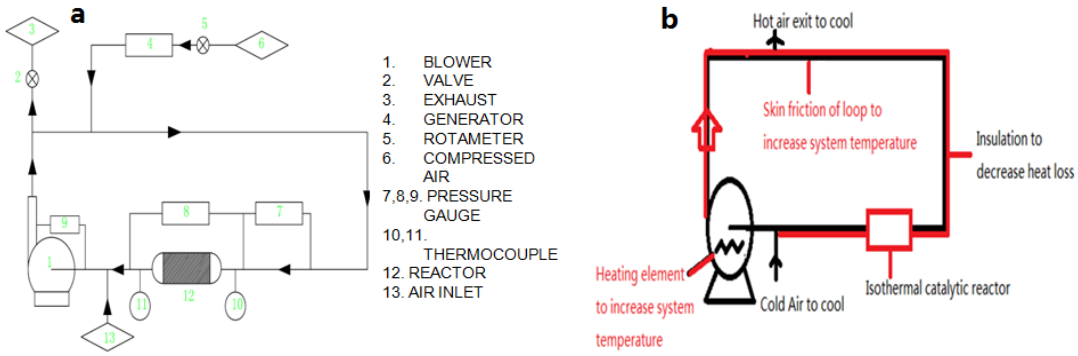

Figure V-2. Sketch of high face velocity test setup: (a) Schematic of test set up (b) Heat balance of the system

V.3.2. High Pressure Tubular Reactor

Figure V-3 shows the 1" diameter tubular reactor that is used to test catalytic performance of MFEC when high system pressure is demanded. This system includes a tubular reactor that is contained in a temperature controlled oven with ozone concentration (Eco Sensor UV100) and temperature (Omega® J type thermocouples) monitored upstream and downstream of the reactor. This tubular reactor can reach same temperature range and face velocity range as that of each pleat in the atmospheric system, while maintaining 2-3 times higher pressure. In high mass flow application, the pressure drop across the MFEC media is in quadratic form, which is affected by several factors including porosity, fiber dimension and media compressibility. The most accurate way of acquiring the pressure drop is by experimentally determined media permeability test. This

test is done by connecting the reactor with IDP10-T differential pressure transmitters located at inlet and outlet of the reactor.

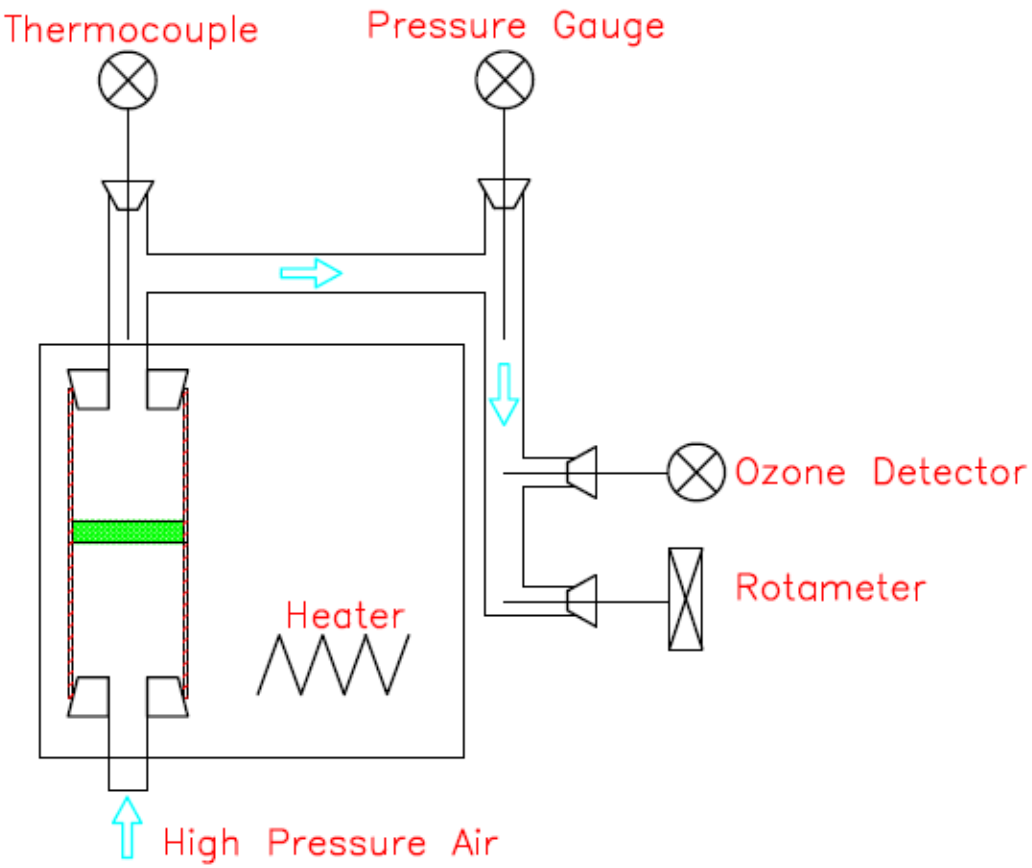

Figure V-3. Tubular reactor for testing MFEC at high system pressure

V.3.3. Microfibrous Material Preparations

Microfibrous material is prepared by traditional wetlay process. Fibers and cellulose are first mixed into a suspension with water viscosity adjusted for slower precipitation. Cellulose added in this process act as a temporary binder for fibers before sintering so that sheets can maintain a proper mechanical strength. The suspension was

then transferred into a head box, where catalyst support particles (Al_2O_3, SiO_2, TiO_2 and etc.) are added and dispersed by rapid mixing. Excess water is drained quickly to avoid uneven distribution caused by different precipitation speed. These preformed sheets are visually examined before an overnight drying process. Dried preform sheets are peroxide at 400℃ to remove the cellulose binder before the sintering process, since cellulose is found to reduce the mechanical strength of sintered sheets. The sintering process is carried out in a BTU-1000® controlled atmosphere electric furnace. MFEC sheets are exposed to high temperature (1000℃ for nickel fiber) for 40 minutes in a reducing environment. Sintered MFEC sheets are impregnated with different catalysts for different purposes using incipient wetness methods. In this research, metal nitrides are used as catalysts precursors. The impregnated sheets are dried overnight and calcinated at 350-500℃ before used as catalyst beds.

V.4. Results and Discussion

V.4.1. Effective Reaction Rate at Higher System Pressures

Since MFEC reactor is a new type of reactor, it is important to determine the flow type within the reactor so that appropriate kinetic model can be applied in analysis. By Reynolds number analysis, the flow within the MFEC is weakly turbulent at high mass flow (10-40 m/s), which indicates plug flow within MFEC. This result has been verified by a numerical analysis [7]. Plug flow is found to exist at this velocity range with very thin boundary layer. The mass balance for a plug flow reactor is given by

$$-v\frac{dc_A}{d_x} = k_m a_c X_c (C_A - C_{AS}) \quad \text{(V. 1)}$$

It is also determined that the ozone decomposition using MFEC at high face velocity range is a mass transfer limited reaction [8], meaning the previous mass transfer rate is the same as reaction rate on the catalyst, then

$$\mathrm{k_m a_c} X_c (\mathrm{C_A - C_{AS}}) = \eta \mathrm{k_r} \rho_c X_c \mathrm{C_{AS}} \quad \text{(V. 2)}$$

If k_{eff} is the effective reaction rate, the we can also write

$$-v\frac{\mathrm{dc_A}}{\mathrm{d_x}} = \mathrm{k_{eff}} X_c \mathrm{C_A} \quad \text{(V. 3)}$$

By eliminating the concentration term in the above equations, the effective reaction rate can be expressed as follows

$$\frac{1}{\mathrm{k_{eff}}} = \frac{1}{\mathrm{k_m a_c}} + \frac{1}{\eta \mathrm{k_r} \rho_c} \quad \text{(V. 4)}$$

The reaction term k_r is the only quantity that needs to be determined experimentally. Tubular reactor was used to determine the catalytic performance at two system pressures. MFEC is manufactured with 8 μm diameter nickel fiber with 70% voidage. The bed is 4 mm in thickness loaded with 1% Pd on Al_2O_3 supports. The k_r in the plot is calculated by iteratively solving Equation and effectiveness factor obtained from ozone decomposition data. The Arrhenius plot for ozone decomposition at 1 atm and 2 atm pressure is shown in Figure V-4. The reaction rate constants are higher at higher system pressures, which indicates an enhancement in surface reaction rate when system pressure is increased.

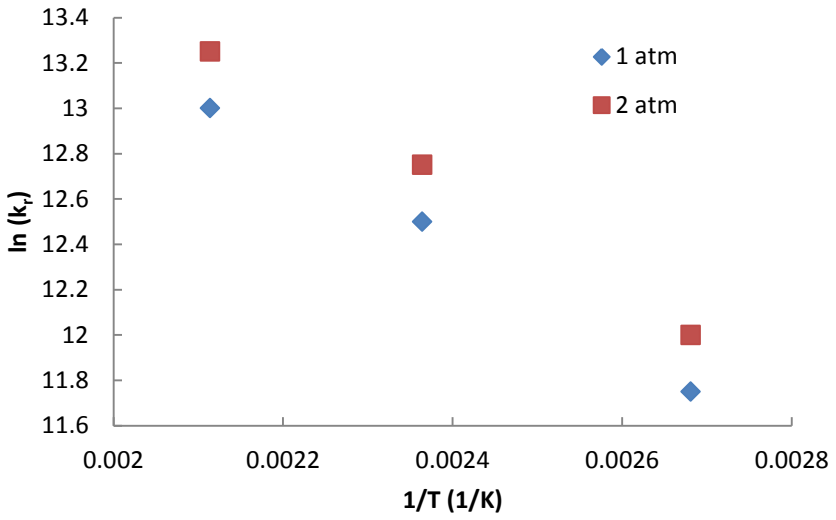

Figure V-4. Arrhenius plot for ozone decomposition using nickel MFEC with 1% Pd catalyst on Al_2O_3 support

The effective reaction rate is a measure of catalyst utilization for the reactor, which considers both surface reaction and gas-solid mass transfer rate. The mass transfer rate is estimated by the Shewood number correlation used by Dwivedi and Upadhyay [9-10. Accoding to Equation 4, the effective reaction rate should reflect similar trend to the mass transfer coefficient curve, if the reaction involved is mass transfer limited. Figure V-5 shows the effective reaction rate for three reactor structures at different face velocities. It is noted that the reaction rate at higher system is enhanced for all structure studied. This enhancement is a combination of both surface reaction rate and the mass transfer rate by the increased effective diffusivity at higher system pressures. It is also noted in Figure V-5 that the effective reaction rate for packed bed and MFEC are significantly higher than monolith. This is because the effective reaction is mainly affected by the gas-solid transfer rate, whose value is much larger for packed bed and

MFEC due to the particle size in these beds. The effective reaction rate for packed bed is also found to be larger than MFEC, because it is more densely packed than the MFEC bed, which makes it less likely for the reactant to reach the catalyst surface.

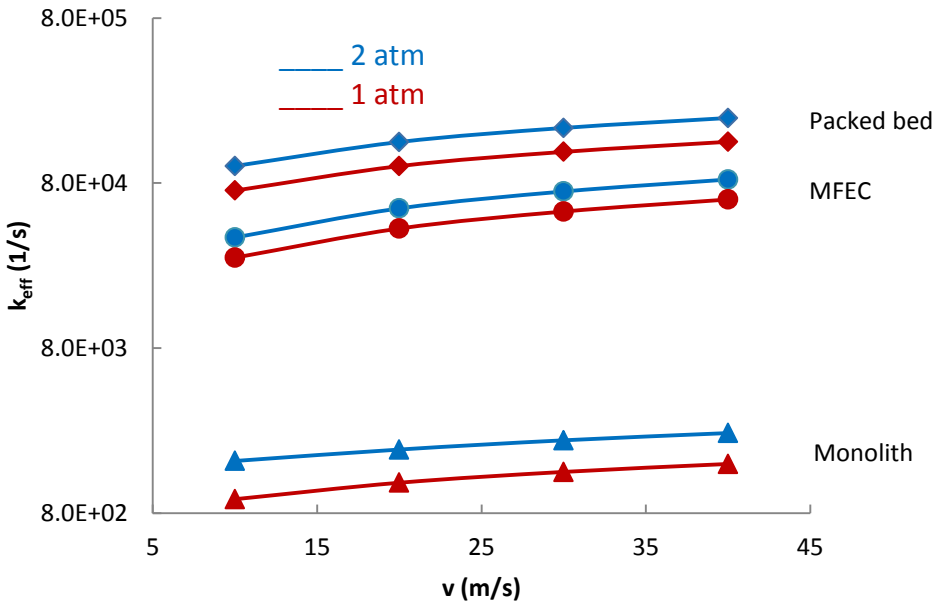

Figure V-5. Effective reaction rate for packed bed, monolith and MFEC reactor at two system pressures

V.4.2. Mass Transfer Rate at Higher System Pressures

The mass transfer coefficients for packed bed, monolith and MFEC are determined by three correlation between Sherwood number and Reynolds number. The Thoenes-Kramers [11] correlation in Equation 5 is used for packed bed. This semi-empirical correlation is valid for packed bed with $40 < Re/(1-\varepsilon) < 400$ and $0.25 < \varepsilon < 0.5$. Tronconi and Forzartti [12] correlation, which is valid for fluid phase mass transfer

coefficient in monolith, is shown in Equation 6. Dwivedi and Upadhyay [9] proposed correlation for gas solid in fixed bed in Equation 7, which is valid for voidage ranging from 0.25 to 0.97 and Reynolds number up to 10000.

$$\mathrm{Sh} = \frac{(1-\varepsilon)^{1/2}}{\varepsilon} Re^{1/2} Sc^{1/3} \quad \text{(V. 5)}$$

$$\mathrm{Sh} = 2.967 + 8.827 \times \left(\frac{1000}{Gz}\right)^{-0.545} \exp\left(\frac{-48.2}{Gz}\right) \quad \text{(V. 6)}$$

$$\mathrm{Sh} = \frac{0.455}{\varepsilon} Re^{0.59} Sc^{0.33} \quad \text{(V. 7)}$$

Figure V-6 shows the volumetric mass transfer coefficient ($k_m a_c$) at different face velocities. It is noted that the mass transfer coefficient for each reactor structure is enhanced at higher system pressure. This increment is mainly due to the higher effective diffusivity at this pressure. The mass transfer coefficient for packed bed and MFEC are in the same range, because the particle sizes used in these beds are similar. However, the voidage of these beds are significantly different. Particles in MFEC material are much more dispersed than the packed bed, making the reactant less likely to interact with catalyst surface. This negative effect on gas-solid transfer coefficient, compared with reduced pressure drop by high voidage, can be ignored when considering overall efficiency.

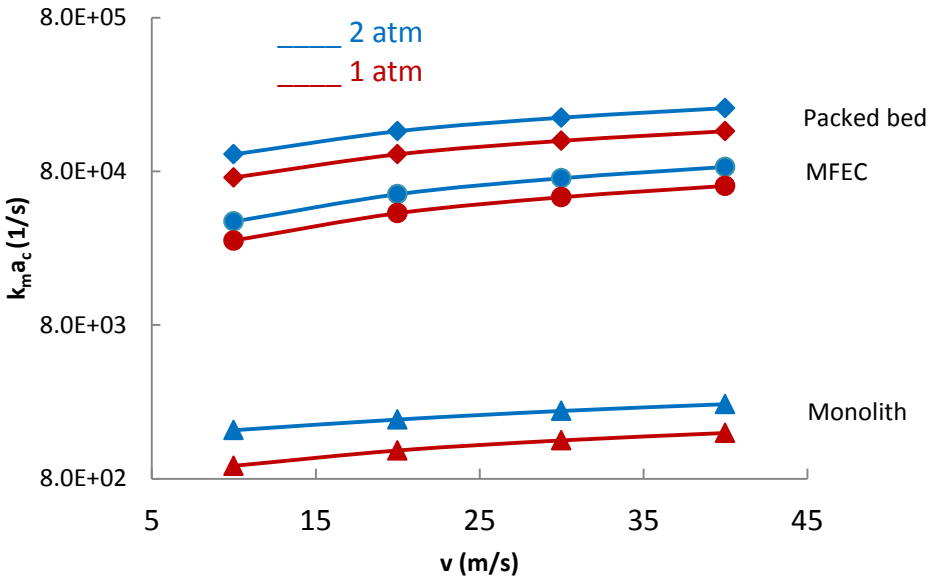

Figure V-6. Volumetric mass transfer coefficient for packed bed, monolith and MFEC reactor at two system pressures

Figure V-6 also explains why traditional reactors like packed bed and monolith are not well adapted to be used in high mass flow condition. Since previous study found the ozone decomposition reaction to be mass transfer limited, the volumetric mass transfer coefficient equals to the maximum reaction rate constant that can be obtained by any reactor structure at a fixed system pressure. It is noted that this rate for monolith is significantly lower than packed bed and MFEC because of the particle size involved. This major disadvantage of low gas-solid transfer rate is the reason why monolith reactor has to be larger in size so that more catalyst can be loaded and more contact time is needed for acceptable conversion rate. As to the packed bed reactor, though the mass transfer coefficient is significantly higher, it possesses very high pressure drop, which

brings down the overall efficiency of the structure. At high mass flow condition, packed bed runs at low cost efficiency.

V.4.3. Heterogeneous Contact Efficiency at Higher System Pressures

The performance comparison of different reactor structures at different system pressures are made using a parameter called heterogeneous contact efficiency, which is defined by the ratio of mass efficiency to flow efficiency. The mass efficiencyχ_m is defined by [13-15]

$$\chi_{\mathrm{M}} = \frac{\mathrm{k_m}}{1+\mathrm{k_c}a_c/\mathrm{k_r}a_c}\frac{\mathrm{L}}{v} = \ln\frac{\mathrm{C_{A1}}}{\mathrm{C_{A2}}} \tag{V. 8}$$

The flow efficiencyχ_F, also known as double Euler number, is defined by

$$\chi_{\mathrm{F}} = \frac{\Delta \mathrm{P}}{\rho v^2/2} \tag{V. 9}$$

Then the heterogeneous contact efficiency is defined as

$$\chi_{\mathrm{F}} = \frac{\chi_{\mathrm{M}}}{\chi_{\mathrm{F}}} = \frac{\ln\frac{\mathrm{C_{Ai}}}{\mathrm{C_{A0}}}}{-\frac{\Delta \mathrm{P}}{\rho v^2}} = \frac{\mathrm{k_m a_c}\epsilon\frac{\mathrm{L}}{v}}{-\frac{\Delta \mathrm{P}}{\rho v^2}} \tag{V. 10}$$

The mass efficiency term in heterogeneous contact efficiency is acquired by experimental method using tubular reactor at different system pressures for each reactor structure. Previous efforts [7] have been made to use both experimental and computational fluid dynamics method to determine the pressure drop across MFEC. Because the physical structure of MFEC is affected by the changing system pressure, experimental pressure drop is preferred in this study to avoid unfair assumptions in simulation. Figure V-7 shows the pressure drop results. Higher pressure drop is monitored for higher system pressure because of the density increase. Moreover, the

higher face velocity brings in more compression of MFEC at higher face velocity, which significantly increases the pressure drop. Figure V-8 shows the heterogeneous contact efficiency for packed bed, monolith and MFEC reactor. The packed bed reactor, which share similar effective reaction rate and gas solid mass transfer rate to MFEC, demonstrates dramatically lower heterogeneous contact efficiency because of the large pressure drop penalty. Monolith reactor, which shows low gas solid mass transfer rate, performs even better than the packed bed in heterogeneous contact efficiency because of the lower pressure drop.

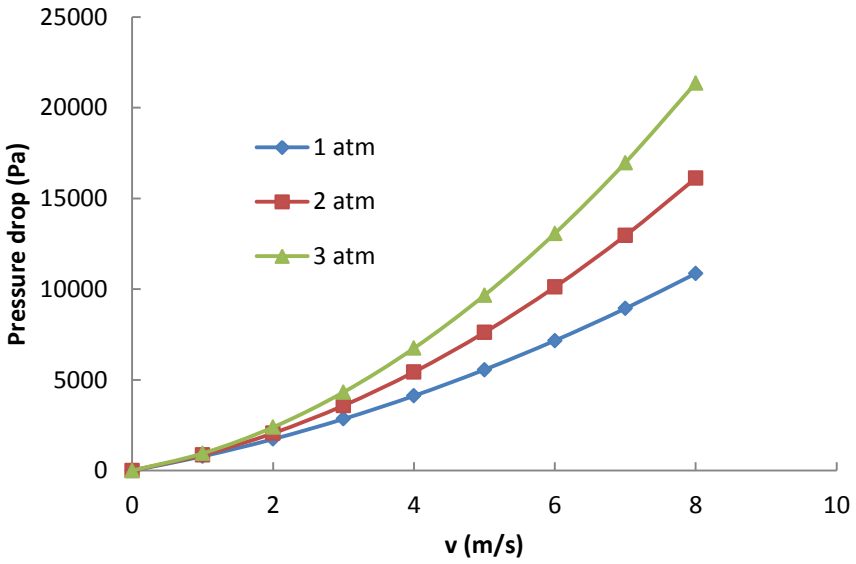

Figure V-7. Pressure drop across flat MFEC at three system pressures with 8μm diameter nickel fibers

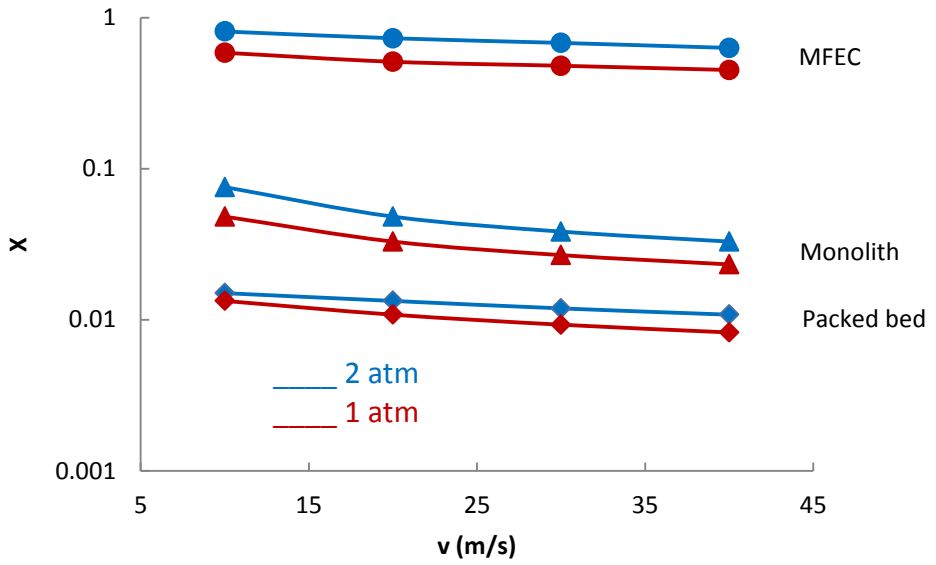

Figure V-8. Heterogeneous contact efficiency for packed bed, monolith and MFEC reactor at two system pressures

V.4.4. Further improvement of Heterogeneous Contact Efficiency

As discussed in the previous section, the MFEC reactor has significantly higher heterogeneous contact efficiency than other reactor structures. This property is preferred in high mass flow application, since it improves the overall performance and reduces the operating cost. While increasing the system pressure improves the heterogeneous contact efficiency, further modification of the structure can be done to enhance its performance. The pressure drop across MFEC at higher system pressure and higher face velocity are found to be significant in Figure V-7 and can be optimized to improve the overall efficiency. However, common methods to reduce pressure drop involves either increasing the voidage of the bed or decreasing bed thickness, both of which will have adverse impact on the catalyst loading in MFEC. A structure with both higher voidage and proper

thickness is demanded for improvement of heterogeneous contact efficiency. Figure V-9 shows the two layers of MFEC stacked together with holes created on each layer. The pressure drop across each layer of the MFEC is significantly reduced because of the increase opening area. The pressure drop over the new structure remains in the same range as a single layer of MFEC structure, because the pressure drop reduction on each layer is compromised by the area which are twice as thick as a single layer. However, the total area for loading catalysts has been increased due to the overlapping area (28.6%), which improve the mass efficiency. It is found that the heterogeneous contact efficiency is enhanced at higher system pressure, especially at lower face velocity region (5% improvement).

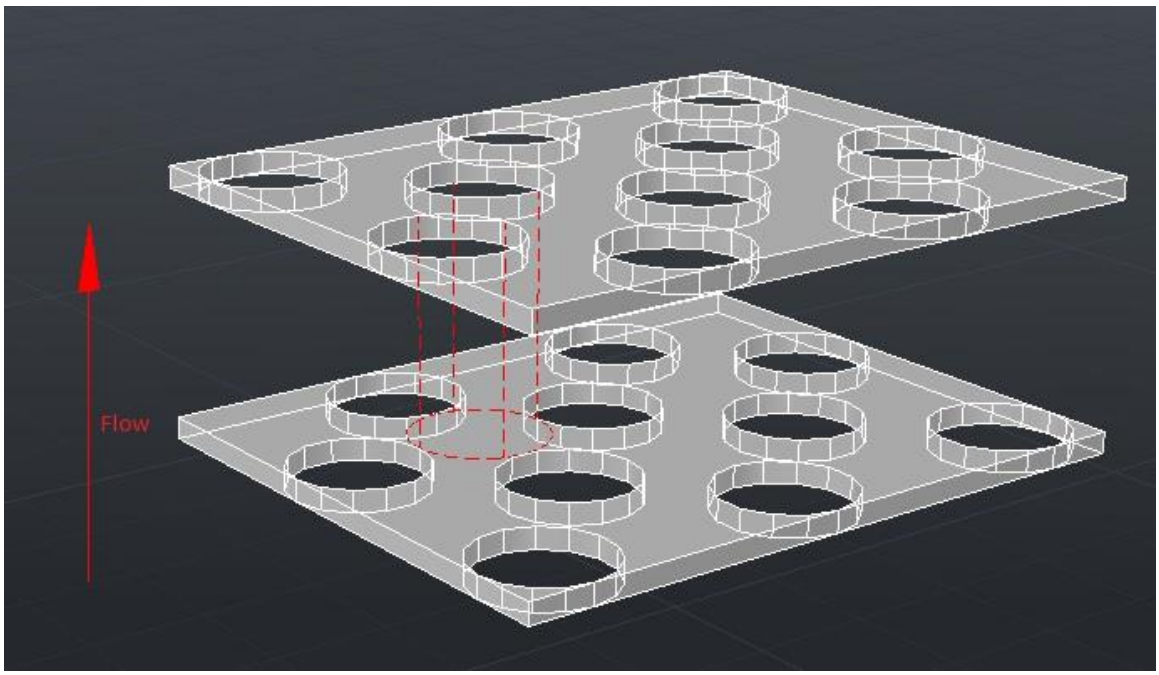

Figure V-9. Position of holes on MFEC to enhance heterogeneous contact efficiency of MFEC

V.4.5. Nusselt Number at Higher System Pressures

Convective heat transfer properties of MFEC has been previously studied [8] by experimentally determined temperature distribution profile within the MFEC material. Compared with bed structures that are made of low thermal conductivity materials, MFEC has demonstrated good heat transfer properties at high face velocity, especially at the radial direction where fibers are preferably aligned due to the wet-lay method used in manufacturing. In this model, heat transfer coefficient for radial and axial directions are separately determined using ensemble averaging method. The original heat transfer equation presented by Bird et al. [16] can be simplified as follows.

$$\rho c_p \left(\frac{\partial T}{\partial t} + v_z \frac{\partial T}{\partial z}\right) = \frac{k_r}{r}\frac{\partial T}{\partial r} + k_r \frac{\partial^2 T}{\partial r^2} + k_z \frac{\partial^2 T}{\partial z^2} + v_z \frac{\Delta p}{l} \qquad \text{(V. 11)}$$

The temperature distribution profile is acquired by numerically solving Equation 11. When system pressure changes, the radial and axial heat transfer coefficient are significantly enhanced by analyzing the ensemble averaging coefficients in Equation 12 and 13 [2-3].

$$D_x = D_f \left\{\frac{1}{1-\phi-\phi m^{-1}} + \frac{171}{3200}\pi^3 \frac{aa^2}{kk\phi}|\wp|\right\} \qquad \text{(V. 12)}$$

$$D_y = D_z = D_f \left\{\frac{1}{1-\phi-\phi m^{-1}} + \frac{9}{6400}\pi^3 \frac{aa^2}{kk\phi}|\wp|\right\} \qquad \text{(V. 13)}$$

The boundary conditions used for solving the equation is listed in Equation 14.

$$@\ z=0\ (j=1)\ T=473\ K;\ @z=z\ (j=M+1)\ \frac{\partial T}{\partial z} = 0;\ @r=0\ (i=1)\ \frac{\partial T}{\partial r} = 0 \qquad \text{(V. 14)}$$

Equation 15 shows the Nusselt number calculation which is used to compare the heat convection under different system pressures. Nusselt numbers are acquired by the temperature distribution profile from previous modeling using Equation 11. Results from

modeling shows that the axial temperature difference between upstream and downstream of the MFEC is insignificantly, since the majority of fibers are not aligned in this direction and the thickness of MFEC bed is relatively small. Radial temperature distribution is mostly uniform along the radial direction with larger temperature gradient at the wall for higher system pressure case. Figure V-10 compares with Nusselt number at two system pressures for MFEC. With the enhanced radial and axial heat transfer rate, overall heat convection at higher system pressures is significantly enhanced. This additional benefit for fiber beds provides more opportunities for it to be used highly exothermic reactions, since the temperature distribution in the bed is much more uniform than packed bed and monolith.

$$Nu = \frac{hL}{K} = \frac{1}{2\pi L/D}\int_0^{L/D}\int_0^{2\pi}(-\frac{\partial T}{\partial r})d\theta dz \qquad \text{(V. 15)}$$

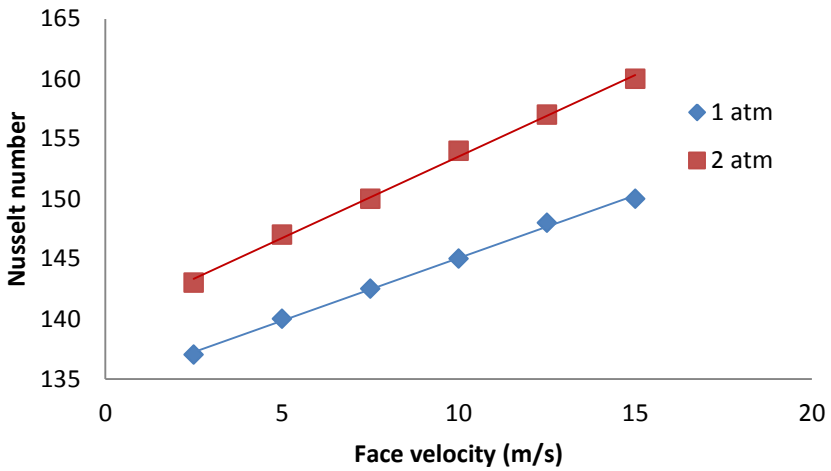

Figure V-10. Nusselt number for nickel fiber MFEC at two system pressures

V.5. Conclusion

System pressure effect on the performance of MFEC at high mass flow applications are evaluated by several factors, including effective reaction rate, gas solid mass transfer rate, heterogeneous contact efficiency and convective heat transfer property. The mass transfer rate for ozone to the catalyst surface was enhanced because of the increase diffusivity. The effective reaction rate should also be enhanced accordingly, since the reaction of ozone decomposition on MFEC was previously found to be mass transfer limited. This hypothesis was tested experimentally and yielded the same result. An overall efficiency factor was introduced to evaluate the conversion at different pressure drop penalty. Higher efficiency factor indicates better conversion at smaller pressure drop penalty. Pressure drop at high system pressures was determined by computational fluid dynamics method. At small molecular flow rate, a higher efficiency factor was calculated at higher system pressure. Also, a convective heat transfer model was utilized to compare the heat transfer characteristics at different system pressures. Axial and radial temperature profiles at different pressures were acquired by numerically solving the heat transfer equation with adjusted air properties. Nusselt numbers were calculated for different system pressures based on the temperatures, which indicated that the heat convection properties were enhanced by the higher system pressures.

Nomenclature

a external surface area per unit volume of catalyst (1/m)

aa fiber radius (m)

C	reactant concentration (mol/m^3)
D	effective thermal diffusivity
h	convective heat transfer coefficient
Gz	Graetz number
K	thermal conductivity
k	mass transfer coefficient (m/s)
kk	scalar permeability of isotropic bed
L	bed thickness (m)
m	ratio of heat capacity in the fluid to the heat capacity in fiber
Nu	Nusselt number
ΔP	pressure drop (Pa)
$\wp$	Peclet number
r	radius (m)
Re	Reynolds number
Sc	Schmidt number
Sh	Sherwood number
T	temperature (K)
t	time (s)
X	volume fraction of catalyst support
x	position along the reactor length (m)
v	face velocity (m/s)
z	axial direction (m)

Greek

χ	heterogeneous contact efficiency
ε	voidage
ϕ	volume fraction of fiber
η	internal effectiveness factor
ρ	density

Subscript

A	reactant A
AS	surface reactant
c	catalyst
eff	effective
f	tracer
M	mass
m	gas phase
r	surface
x	x direction
y	y direction
z	z direction

References

[1] M. Sheng, H. Yang, D. Cahela, B. Tatarchuk, J. of Catal. 283 (2011) 254-262.

[2] D.L. Koch, J.F. Brady, AICHE J. 32 (1986) 575-591.

[3] D.L. Koch, J.F. Brady, J. of Fluid Mech. 154 (1985) 399-427.

[4] D.K. Harris, D.R. Cahela, B.J. Tatarchuk, Composites Part A 32 (2001) 1117-1126.

[5] D.R. Cahela, B.J. Tatarchuk, Catal. Today 69 (2001) 33-39.

[6] A.N. Karwa, B.J. Tatarchuk, Sep. and Purif. Technol. 86 (2012) 55-63.

[7] Q. Gu, B. Tatarchuk, Proc. AIChE (2013) 583m.

[8] Q. Gu, B. Tatarchuk, Proc. AIChE (2013) 405d.

[9] P.N. Dwivedi, S.N. Upadhyay, Ind. & Eng. Chem. Process Des. and Dev. 16 (1977) 157-165.

[10] R.R. Kalluri, D.R. Cahela, B.J. Tatarchuk, Appl. Catal., B 90 (2009) 507-515.

[11] H.S. Fogler, Elements of Reaction Engineering, third ed., Prentice Hall PTR, New Jersey, 1999.

[12] E. Tronconi, A. Beretta, Catal. Today 52 (1991) 249–258.

[13] A. Kołodziej, J. Łojewska, Chem. Eng. Process. 46 (2007) 637–648.

[14] L. Giani, G. Groppi, E. Tronconi, Ind. Eng. Chem. Res. 44 (2005) 4993–5002.

[15] F.C. Patcas, G.I. Garrido, B. Kraushaar-Czarnetzki, Chem. Eng. Sci. 62 (2007) 3984–3990.

[16] R. Bird, W. Stewart, E. Lightfoot, Transport Phenomena, 2nd ed. New York, John Wiley & Son, Inc., 2001

Chapter VI Conclusion & Suggested Future Work

VI.1. Conclusion

This research is a comprehensive study of the ozone removal using microfibrous entrapped catalysts at high velocity applications. A wide selection of catalysts for ozone decomposition have been tested using MFEC. Performances have been compared with conventional monoliths, which demonstrated the advantages of MFEC in high velocity applications. The high intra particle mass transfer property of the material significantly enhanced the performance of the reactor even if the contact time for the reactions is very short. Several aspects that affects the performance of MFEC, including humidity, system pressure and catalyst loading has also been studied to optimize the performance of MFEC at different operating conditions.

Meanwhile, the catalytic performance of MFEC at increased system pressure (2-3 atm) is studied, because the high face velocity applications in real world usually involve increased system pressure. The pressure change impacts the mass transfer properties of the reaction, which is crucial to the ozone decomposition reaction at high face velocity condition. The overall performance of the MFEC beds at increased system pressure is compared with packed beds and monoliths to demonstrate the advantages of using MFEC at high face velocity and increased system pressure condition. Both catalytic and pressure drop performance are evaluated experimentally.

In addition, heat convection property has for MFEC at high face velocity conditions has been investigated, because the pressure volume work by air compression generates heat. Temperature distribution profile has been acquired by both experimental

and theoretical methods. MFEC beds are found to perform well in terms of heat management at high face velocity conditions. The temperature difference between the centerline and the wall is insignificant, which helps with catalyst stability, catalyst lifetime and catalytic properties.

In conclusion, the MFEC application at high velocity range is not limited to ozone decomposition reaction. The purpose of this study is to demonstrate the catalytic performance of the material in a wide selection of applications. Potential applications include turbine engine bleed air filtration, fuel cell cathode air filtration, automobile engine air filtration and aircraft cabin air filtration. Through modified design work, the MFEC material can demonstrate high performance and flexibility as a catalytic bed.

VI.2. Future Work

1. Computational fluid dynamics model of heat transfer considering chemical reaction can be conducted to study the reaction effect on the temperature distribution within the material
2. Gas mixture has been studied under low velocity in literatures. Studies can be conducted under high velocity range to investigate its effect on the mass transfer.
3. MFEC performance at increased system pressure (2-3 atm) should be evaluated using full scale test system, which requires the replacement of current blower. The test is intended to test the stability of catalysts, the reliability of filter structure and the impact of filter housing on the overall pressure drop.

4. Filter structure can be heated (e.g. electric current through the media) so that cold air with contaminant can be tested for catalytic performance. In this case, a proper catalytic activity can be maintained because of the higher catalyst temperature. This method is more suitable for high volumetric flow applications without significant heat source.
5. MFEC material with fluffy structure can be made to test pre-manufactured commercial catalysts. This methods provides an even wide selection of catalysts that can be used to remove certain contaminants that is difficult to remove at high face velocity applications.

Appendix 1

Code for velocity profile calculation in MFEC

```
clear all
clc
N=600;
n=20;
V0=zeros(N+1,n+1);
V1=zeros(N+1,n+1);
for i=1:N+1
   for j=1:n+1
      V0(i,j)=10;
   end
end
z=0.0025;
dz=z/n;
r=0.15/2;
dr=r/N;
dt=1/10000000;
vz=10;
dp=117.11*vz^2+160.2*vz;
p=0.8;
u=10^(-5);
error=1;
```

```
kk=0;
while error>=0.0001
   for i=2:N
      for j=2:n
         V1(i,j)=V0(i,j)*(1-2*dt*u/p/dr^2-2*dt*u/p/dz^2)+V0(i+1,j)*(dt*u/2/p/dr/(i-
1)/dr+dt*u/p/dr^2)+V0(i-1,j)*(dt*u/p/dr^2-dt*u/2/p/dr/(i-
1)/dr)+V0(i,j+1)*dt*u/p/dz^2+V0(i,j-1)*dt*u/p/dz^2-
dt/2/dz*V0(i,j)*V0(i,j+1)+dt/2/dz*V0(i,j)*V0(i,j-1)+(dt/p*dp/z-dt/p*dp)/1000;
      end
   end
   V1(1,:)=4/3*V1(2,:)-1/3*V1(3,:);
   V1(:,n+1)=4/3*V1(:,n)-1/3*V1(:,n-1);
   V1(:,1)=10;
   V1(N+1,:)=0;
   error=0;
   for i=1:N+1
      for j=1:n+1
         error=error+(V1(i,j)-V0(i,j))^2;
      end
   end
   error=(error/(N+1)/(n+1))^0.5
   kk=kk+1
   V0(:,:)=V1(:,:);
```

```
end
imagesc(V0);
colorbar
```

Appendix 2

Code for temperature profile calculation in MFEC

```
clear all
clc
N=600;
n=20;
T0=zeros(N+1,n+1);
for i=1:N+1
   for j=1:n+1
      T0(i,j)=493;
   end
end
T1=zeros(N+1,n+1);
TT=293;
kr=300;
kz=30;
hw=100;
vz=10;
%vNi=0.03;
```

```
%vAl=0.29;
%void=1-vNi-vAl;
pcp=500;
r=0.15/2;
rid=(0.15-0.002)/2;
bi=hw*rid/kr;
z=0.0025;
dr=r/N;
dz=z/n;
dt=1/1000000000000/2;
dp=117.11*vz^2+160.2*vz;
kk=0;
error=1;
while error>=0.00001
   for i=2:N
      for j=2:n
         pair=((-
(117.11*vz^2+160.2*vz)*j*dz/0.0025)+100000+117.11*vz^2+160.2*vz)/8.314/T0(i,j)*2
9/1000;
         pcp=(void+vAl*0.816)*pair*1009;
         T1(i,j)=T0(i,j)*(1-2*dt*kr/pcp/dr^2-2*dt*kz/pcp/dz^2)+T0(i+1,j)*(kr*dt/pcp/(i-
1)/dr/dr+kr*dt/dr^2/pcp)+T0(i-1,j)*(dt*kr/pcp/dr^2-dt*kr/2/pcp/(i-
1)/dr/dr)+T0(i,j+1)*(dt*kz/pcp/dz^2-dt*vz/2/dz)+T0(i,j-1)*(dt*kz/pcp/dz^2+dt*vz/2/dz)-
```

```
vz*dp/z*dt/pcp;
        end
    end
T1(1,:)=4/3*T1(2,:)-1/3*T1(3,:);
T1(:,n+1)=4/3*T1(:,n)-1/3*T1(:,n-1);
T1(N+1,:)=(2*bi*TT/N+(4*T1(N,:)-T1(N-
1,:))*(1+bi*kr/400*log(r/rid)))/(2*bi/N+3*(1+bi*kr/400*log(r/rid)));
T1(:,1)=493;
error=0;
for i=1:N+1
    for j=1:n+1
        error=error+(T1(i,j)-T0(i,j))^2;
    end
end
error=(error/(N+1)/(n+1))^0.5
kk=kk+1
T0(:,:)=T1(:,:);
end
imagesc(T0)
colorbar
```